

Late Holocene climate at Hallet and Greyling Lakes,
central Chugach Range, south-central Alaska

By Nicholas McKay

A Thesis
Submitted in Partial Fulfillment
Of the Requirements for the Degree of
Master of Science
In Geology

Northern Arizona University

June, 2007

Approved:

Darrell S. Kaufman, Ph.D., Chair

R. Scott Anderson, Ph.D.

James Sample, Ph.D.

Al Werner, Ph.D.

Abstract

Late Holocene climate at Hallet and Greyling Lakes,
central Chugach Range, south-central Alaska

Nicholas McKay

Lake sediments and glacier extents were used to reconstruct late Holocene climate changes from Hallet (61.5°N, 146.2°W; 1128 m asl) and Greyling (61.4°N, 145.7°W; 1015 m asl) Lakes in the Chugach Mountains, south-central Alaska. The lakes are located 30 km apart near the crest of the range and both have glaciated catchments. Age models for the two sediment cores, one from Hallet Lake (core HT01, taken in 40 m of water) and one from Greyling Lake (core GY05, 12 m water depth), were developed using 16 radiocarbon (^{14}C) ages, two tephra ages, and a $^{239+240}\text{Pu}$ profile. Biogenic silica (BSi) in core HT01 was analyzed at high resolution (~10 yr intervals) for the past 2 kyr, and lower resolution (~50 yr) for the rest of the record, back to 7.7 ka. Organic matter content (OM) was analyzed by loss on ignition in core HT01 (~25 yr interval) and core GY05 (~75-250 yr interval).

High-resolution measurements of OM and BSi flux from the last 130 yr (top 10 cm of surface sediment) were correlated with a suite of instrumental climate records from Valdez and Gulkana, and with published climate indices for the north Pacific region. OM is related to the Aleutian Low Pressure Index (ALPI) ($r = 0.66$) and Gulkana and Valdez winter (DJFM) temperature ($r = 0.63$ and 0.75 , respectively). Over the past ~4.3 kyr, fluctuations in OM in cores from Greyling and Hallet Lakes are remarkably similar. This

suggests that the sediment at each lake records regional climate variability, and that the age models for this part of each core are robust.

BSi flux correlates most strongly with Valdez summer (JJA) temperature ($r = 0.87$), and a transfer function was developed using this relation to quantitatively reconstruct summer temperatures for the past 2 kyr. The reconstructed temperatures indicate periods of warm summer temperatures from 100-500 AD, 1300-1500 AD, and after ~1900 AD. Periods of cool summer temperatures occurred from 500-1200 AD, and from 1600-1900 AD. Fluctuations in OM over the past 2000 yr, interpreted to reflect AL strength and winter temperature, show similarities and differences with BSi-inferred summer temperature. OM was relatively high from 0-500 AD, 900-1300 AD, and after ~1900 AD. Low values occurred from 500-800 AD, and 1400-1900 AD.

The accumulation-area ratio (AAR) method was used to estimate former equilibrium-line altitudes (ELAs) for the maximum LIA and modern extents of 25 glaciers in the study area. The calculated ELA lowering during the LIA, relative to 1978, was 92 m. In contrast, the BSi-inferred temperature lowering of 1.5°C during the LIA can be applied to a local environmental lapse rate ($-7^{\circ}\text{C km}^{-1}$) to suggest that ELA should have lowered by 210 m. This suggests a reduction in accumulation-season precipitation relative to 1978 and is consistent with the OM record, which implies reduced AL strength during the LIA. The paleotemperature record from Hallet Lake will be integrated into the ongoing NSF-ARCSS 2 kyr synthesis project.

Table of Contents

	Page
Abstract.....	2
List of Tables.....	5
List of Figures.....	6
Chapters	
1. Introduction.....	7
a. Study area	7
b. Background	8
2. Methods.....	12
a. Glacial History	12
b. Lake sediments	15
3. Glacial history.....	20
a. Hallet Valley	20
b. Greyling Valley	21
c. Equilibrium-line altitudes	22
4. Lake sediments.....	23
a. Geochronology	23
b. Sedimentological and biological analyses – Hallet Lake	27
c. Sedimentological and biological analyses – Greyling Lake	30
d. Climate correlations	32
5. Climate variability at Hallet and Greyling Lakes.....	35
a. Climate variability over the past 2 kyr	35
b. Climate variability from 15 – 2 ka	42
6. Summary and conclusions.....	46
7. References.....	49

List of Tables

	Page
1. Lake cores recovered from Hallet and Greyling Lakes.....	54
2. Radiocarbon ages and complimentary data.....	55
3. Lichen sizes on moraines in Hallet and Greyling Valleys.....	56
4. Central Chugach Mountains cirque glacier equilibrium-line altitudes.....	57
5. Tephra geochemistry.....	58
6. ²³⁹⁺²⁴⁰ Pu, ¹³⁷ Cs, and ²¹⁰ Pb activities for Hallet and Greyling Lakes.....	60
7. Correlations between biogenic silica flux and organic-matter content in Hallet Lake and meteorological records and North Pacific climate indices.....	61
8. Biogenic silica flux and organic-matter data from Hallet Lake, along with selected instrumental datasets.....	62

List of Figures

	Page
1. Map of Alaska and study area.....	63
2. Color-infrared aerial photographs of Hallet and Greyling Lakes.....	64
3. Bathymetry of Hallet and Greyling Lakes.....	65
4. Map of modern and former glacier extents near Hallet and Greyling Lakes.....	66
5. Relation between Aleutian Low strength and winter temperature and precipitation in the Gulf of Alaska.....	67
6. 1978 and Little Ice Age equilibrium-line altitudes for cirque glaciers near Hallet and Greyling Lakes.....	68
7. Accumulation area ratio data from Wolverine and Gulkana Glaciers.....	69
8. Equilibrium-line altitudes from west to east in the study area.....	70
9. Tephra geochemistry.....	71
10. Tephra shard morphology.....	72
11. $^{239+240}\text{Pu}$, ^{137}Cs , and ^{210}Pb activities in Hallet Lake.....	73
12. Lithostratigraphy, sedimentology and biological parameters in Greyling Lake..	74
13. $^{239+240}\text{Pu}$, ^{137}Cs , and ^{210}Pb activities in Greyling Lake.....	75
14. Age-depth models for Hallet and Greyling Lakes.....	76
15. Lithostratigraphy, sedimentology and biological parameters in Hallet Lake.....	77
16. Organic-matter content in Hallet and Greyling Lakes over the past 5 kyr.....	78
17. Relation between daily air temperature at Greyling Lake and Gulkana and Valdez.....	79
18. Organic-matter content in Hallet Lake and the ALPI over the past 100 yr.....	80
19. Relation between biogenic silica flux in Hallet Lake and Valdez temperature...	81
20. Air and water temperature at Greyling Lake.....	82
21. Biogenic-silica-inferred temperature reconstruction for Hallet Lake.....	83
22. Comparison of Hallet Lake climate records to regional and hemispheric climate proxies.....	84
23. Organic-matter content, grain size, and sedimentation rate for Greyling Lake over the past 15 ka.....	85
24. Biogenic silica, organic-matter content, grain size, and sedimentation rate for Greyling Lake over the past 8 ka.....	86

Introduction

To better predict future changes in climate and to determine the degree and effects of human impacts on climate, 20th century warming must be placed in a longer-term context of climate variability. Arctic climate appears to be sensitive to global changes in climate and has demonstrated a high susceptibility to modern anthropogenic climate change (Overpeck et al., 1997). Because most reliable meteorological records from the arctic do not extend beyond the early 20th century, longer-term climate variability must be inferred from proxy records. This study utilizes variations in the sedimentologic and biologic characteristics of sediment deposited in glacier-fed Hallet and Greyling Lakes, in the Chugach Mountains of southern Alaska, to develop a high-resolution record of late Holocene climate for the region.

This study is part of a larger project to synthesize high-resolution (annual to decadal scale variability) lacustrine records of late Holocene climate from 30 lakes across the North American Arctic (<http://www.arcus.org/synthesis2k/>). The climate records developed from Hallet and Greyling Lake sediments will play a part in furthering our understanding of how modern climate change fits into the context of late Holocene climate on a global scale, and a better understanding of how modern modes of climatic variability, and regional climatic phenomena (i.e., Aleutian low) have affected North America through time.

Study area

Hallet Lake (61.5°N, 146.2°W) is located in southern Alaska on the northern flank of the Chugach Mountains at 1128 m asl (figure 1). The lake occupies the bottom of a glacial

valley, dammed by a series of large debris avalanches near the mouth of the tributary valley (figure 2). The lake covers 0.61 km^2 , and has relatively simple bathymetry, with large deltaic fans located at the mouths of the two major inflows, and an otherwise flat lake bottom, 41 m deep at its deepest point (figure 3a). The lake drains 9.4 km^2 , including seven cirque glaciers, that range from 0.05 to 0.70 km^2 (figures 2 and 4a).

Greyling Lake (61.4°N , 145.7°W) is located 30 km east of Hallet Lake, also near the crest of the range at 1015 m asl. The lake is elongate, approximately 2 km long, with three sub-basins (figure 3b). It covers 0.67 km^2 , is 36 m deep at its deepest point (figure 3b), and its drainage area covers 10 km^2 , including four cirque glaciers that range from 0.25 to 1 km^2 (figures 2 and 4b). Greyling Lake is fed by the outlet of Upper Greyling Lake, which is located up-drainage, about 300 m south of Greyling Lake. Upper Greyling is 1100 m asl, covers 0.28 km^2 , and is roughly circular (figures 1 and 2).

Background

Modern climate in southern Alaska

Hallet and Greyling Lakes are in what has been described as a transitional climate regime, separating the maritime region to the south from the continental regime to the north (Papineau, 2001). Winter climate in the region is dominated by the Aleutian Low-Pressure System (AL), a regional-scale low pressure center that is best organized during the winter and spring. The strength and position of the AL is well-correlated to both winter temperature and winter precipitation throughout Beringia; an enhanced AL corresponds to warmer and wetter winters in south-central Alaska (figure 5) (Mock et al., 1998; Rodionov et al., 2005). The strength of the AL varies from year to year, although

decadal-scale modes of typically enhanced or weakened AL have been observed over the past century (Beamish et al., 1997; Minobe and Mantua, 1999). These modes are related to larger scale oscillations in pacific and arctic climate, such as the Pacific Decadal Oscillation (PDO), the El Niño Southern Oscillation (ENSO), and the Arctic Oscillation (AO) (Papineau, 2001). For example, negative phases of the PDO are associated with an enhanced AL, as well as greater interannual variability in AL (Minobe and Mantua, 1999). El Niño years are also associated with warmer winters and deepened AL (Papineau, 2001).

The strength of the Aleutian Low has been characterized by several indices, most commonly the Aleutian Low-Pressure Index (ALPI), the North Pacific Index (NPI), and the Pacific Decadal Oscillation Index (PDOI). The ALPI for any given year is defined as the average area in the northern Pacific Ocean with sea-level pressures below 100.5 kPa from December-March. This study relies on the ALPI as a measure of AL strength over the past 100 yr (Beamish et al., 1997).

Lake sediments as climate proxies

Lake sediments have been widely used as climate proxies in Alaska (e.g., Hu et al., 2001; Kaufman et al., 2003; Loso et al., 2006), and have provided valuable information on past climate. The steady deposition of sediment often results in a continuous record, that may be well dated by ^{14}C dating, tephrochronology, and under the right circumstances, counting annual layers (varves). The use of multiple proxies is commonly appropriate, allowing for multiple aspects of the climate system to be reconstructed from a single sediment sequence. Proglacial lakes are often sensitive to glacial activity. Glaciers are

sensitive indicators of changes in climate, specifically summer temperature and winter precipitation (Nesje et al., 2001; Ohlendorf et al., 1997). Variations in physical sedimentation parameters have been used to define periods of glacial advance and retreat, as well as to imply changes in climate as reflected by changes in glacial activity (Ohlendorf et al., 1997; Smith et al., 2004). Biological proxies from mountain lakes are also particularly sensitive to changes in climate (Nesje et al., 2004).

Organic-matter content (OM) has been shown to be an excellent proxy of environmental change in high-latitude lakes (Willemse and Törnqvist, 1999; Nesje and Dahl, 2001; Kaplan et al., 2002; Nesje et al., 2004). The interpretation of down-core variations in OM is commonly complex, although in proglacial lakes, the OM is typically a balance between the amount of organic material produced in and around the lake, and the amount of minerogenic sediment being deposited in the lake due to variations in glacial activity (Nesje et al., 2004).

Biogenic silica (BSi) is a measure of the sedimentary abundance diatoms, a photosynthetic algae that secrete an internal shell, and is commonly related to lake primary productivity (Wetzel, 2001). Several studies have related BSi to climate at high-latitude lakes; Hu et al. (2003) recognized that BSi in Arolik Lake in southwestern Alaska fluctuates in synchronicity with solar cycles. Nesje et al. (2004) attribute variations in BSi in Danntjørn, in southern Norway, to changes in summer temperature through the Holocene. This is the first study that I know of which uses BSi to quantitatively reconstruct summer temperature.

Paleoclimate records from southern Alaska

Little work has been done using lacustrine sediments as a proxy for climate with decadal scale resolution in Alaska; most studies using lacustrine deposits to reconstruct climate in southern Alaska (Hu et al., 1998; Kaufman et al., 2003; Anderson et al., 2005) have not developed climate records with fine enough resolution to place modern instrumental records in context with late Holocene climate. A recent study (Loso et al., 2006) developed a high-resolution record from varved sediments deposited in an ice-dammed lake in the eastern Chugach Mountains. There are similarly few studies which have used lacustrine proxies to develop quantitative reconstructions of south-Alaskan climate. Hu et al. (2001) used a geochemical proxy from Farewell Lake in the Alaska Range to quantitatively reconstruct growing-season temperature.

Most other investigations of late Holocene climate in Alaska with finer-than-centennial scale resolution have relied on tree rings. Tree rings are valuable records of climate, but do not extend reliably beyond 1000 years in Alaska (Barclay et al., 1999). Geomorphic records of glacial advances from southern Alaska have been used to imply periods of wet and cool climate in the late Holocene, and are generally well dated by ^{14}C , tree-ring chronologies, and lichenometry, and provide a good framework of major climatic events (Calkin et al., 2001; Wiles et al., 2002; Wiles et al., 2007). However, these records are discrete and low-resolution, and are not directly comparable to records of modern climate. Ice cores have been recovered from two sites in the Yukon Territory, but neither has produced a definitive high-resolution record of late Holocene climate for the region. The Mt. Logan ice core is not ideally situated to record regional climate; the high elevation site (5340 m asl) is sensitive to high tropospheric air masses that bear little

resemblance to the lower air masses relevant to most of Alaska's climate (Holdsworth et al., 1991). Ice cores from the Eclipse Icefield have been correlated with several instrumental temperature records from the region (Wake et al., 2003), but because of the high accumulation rates, no climate record has been developed from the ice cores that extends beyond 1000 yr.

Methods

Glacial history

Glacial landform mapping and lichenometry

The series of prominent late Holocene moraines formed in the forefields of extant glaciers at the head of both Greyling and Hallet valleys were mapped during July 2006. Twenty-six lichen stations (13 in each valley) were established on well-defined moraines (figure 4) to estimate the timing of the multiple moraine-forming intervals. At each lichen station, the long and short axes of circular or subcircular *Rhizocarpon geographicum* thalli were measured on 15-20 boulders to characterize the largest lichens at the station. The age of each landform was calculated by applying the length of the long axis of the largest lichen (unless it was 20% larger than the second largest) to an empirically derived growth curve. Because no lichen growth curves have been developed for the Chugach Range, I relied on the composite curve for the Wrangell–St. Elias Mountains presented by Solomina and Calkin (2003). The growth curve assumes a 30 yr colonization time.

$$38.813 \cdot 10^{(0.022408 \cdot D)} \text{ (great period);}$$
$$- 1018.4 + 30.095 \cdot D \text{ (linear phase)}$$

Where D = lichen diameter in mm

This is the nearest, climatically similar area with a well-established lichen record. The ages of the landforms are estimated to be accurate to within $\pm 20\%$ of the calculated numerical ages (Calkin and Ellis, 1980; Bickerton and Matthews, 1992); however, confidence is increased when using lichen sizes to correlate between landforms in the same locality.

Equilibrium-line altitudes

The accumulation area ratio (AAR) method (Meier and Post, 1962) was used to reconstruct equilibrium-line altitudes (ELAs) for 25 modern glaciers (16 near Greyling Lake, 9 near Hallet Lake) in the study area, and for the maximum LIA ice extent for each glacier. Only glaciers with well-defined maximum LIA moraines were selected for ELA reconstruction. Modern glacier extent was interpreted from 1:63,360-scale aerial photos taken in 1978. LIA extent was determined by photo-interpretative mapping of glaciogeomorphic evidence, and field checked at five sites, those located in the watersheds of Greyling and Hallet Lakes (figure 6). Three-dimensional models of the glacier surfaces were created in ArcGIS v9.1 using the mapped glacier extents, and elevations derived from a 30 m digital elevation model (DEM) of the region. The elevations used by the DEM were from USGS topographic maps published in 1979, based on aerial photographs taken in 1978. Consequently, the three-dimensional glacier surface models underestimate the height of the LIA glacier surfaces; this is acceptable for maximum ELA lowering estimates (Δ ELA) (the difference between calculated modern and LIA ELAs) since it results in underestimating the LIA ELA, increasing Δ ELA.

To determine an appropriate AAR for both the modern and LIA glaciers, a range of values common for alpine glaciers (0.55-0.65) (Dyurgerov et al., 2002) were evaluated to determine which value resulted in the least variability (lowest standard deviation) among the calculated ELAs in the field area, as suggested by Osmaston (2005). For both modern and LIA glaciers, there was essentially no difference in variability across the range of AARs. Therefore, AARs were instead chosen to reconstruct a reasonable estimate of maximum Δ ELA. To do this, the highest reasonable AAR was chosen for LIA ELA reconstructions, while the lowest reasonable AAR was used to reconstruct 1978 ELAs. An AAR of 0.65 was chosen for the LIA glaciers, because this value is generally the maximum for stable alpine glaciers (Dyurgerov et al., 2002), and the large LIA moraines attest to the relative stability of these former glaciers. Glaciers in the study area retreated during the second half of the 20th century (indicated by 1951 USGS topographic maps (an earlier version than those used to interpret DEM elevations, based on 1950 aerial photographs), 1978 aerial photographs, and 2006 field-mapped glacier extents). This suggests that the 1978 glaciers were most likely not in equilibrium with their climate and the AAR is expected to be somewhat lower than for the equilibrium state. Therefore, a reasonable estimate for minimum AAR for the 1978 glaciers is determined by comparison to mass balance data for the two glaciers in southern Alaska with long-term records, Gulkana and Wolverine Glaciers (figure 1). The mass balance data indicate an average AAR of 0.58 (Gulkana Glacier = 0.56, Wolverine Glacier = 0.59) from 1966-1978 (Dyurgerov et al., 2002). While these records are from glaciers located ~200 km from the study area, they show regional synchronicity and consistency in AAR (figure 7), and probably serve as a good estimate of AAR for the glaciers in this

study because they bracket the study area both geographically and climatically (figure 1). Therefore, a conservative, but realistic, AAR estimate of 0.55 was chosen for the 1978 glaciers in order to account for potential differences from the records from Gulkana and Wolverine Glaciers, and to calculate a reasonable estimate of maximum Δ ELA.

Lake sediments

Core recovery

The bathymetry of both Hallet and Greyling Lakes was mapped prior to coring using a GPS-integrated Lowrance sonar unit. Coring sites were chosen to sample areas with both high and low sedimentation rates. Six cores (three from each lake) were recovered during the 2006 field using a percussion coring system, operated from a floating platform. The cores were 7.5 cm in diameter and up to 4.5 m long (Table 1). At Hallet Lake, three cores (HT01, HT02, and HT03) were taken from the deepest part of the lake (~40 m), each increasingly distal from the main inflow at the south end of the lake (figure 3a). At Greyling Lake, one core was taken from each of the three sub-basins (GY03 = northern, GY04 = southern, and GY05 = central), in water depths ranging from ~12 m in the central basin, to ~35 m in the southern basin (figure 3b). In addition to the percussion cores, multiple surface cores were taken to recover the sediment-water interface, which is typically not preserved by percussion cores. In the laboratory, the cores were split, photographed, and described. The cores were then subsampled to analyze a variety of sedimentological and biological parameters. Cores HT01 and GY05 were chosen as the foci of the research because they were the least deformed by the coring procedure, to

compare records between lakes, and to develop a high-resolution record for the past 2 kyr (HT01), in addition to a record which might span the entire Holocene (GY05).

Modern sedimentation

An instrument mooring was deployed in June 2004 in the southern sub-basin of Greyling Lake (figure 3b). Sediment traps and temperature loggers were stationed at 3.6 and 30.9 m water depth. The collected sediments were described and subsampled in August 2005, and July 2006.

Geochronology

A total of 16 radiocarbon (^{14}C) ages were obtained from core HT01 (9) and GY05 (7). All of the analyses were on vegetation macrofossils, although the size fraction and composition varied (Table 2). Accelerator mass spectrometer (AMS) analyses were performed at the Keck Carbon Cycle AMS Facility at the University of California, Irvine. The ^{14}C ages were calibrated using CALIB v 5.02 (Stuiver and Reimer, 1993). Single best estimates for each calendar age are presented as the median probability of the 2σ calibrated age range (Telford et al., 2004).

The activities of $^{239+240}\text{Pu}$ were measured on 20 contiguous 0.5-cm-thick samples from 0-10 cm in surface core HT01-B, and on 14, 0.5-cm-thick samples from 0-14 cm in surface core GY02-A using the inductively coupled plasma mass spectrometer (ICPMS) at Northern Arizona University. $^{239+240}\text{Pu}$ isotopes do not occur naturally in the atmosphere, but were produced as a byproduct of nuclear weapon testing (Ketterer et al., 2004). $^{239+240}\text{Pu}$ may be used as a geochronometer, because the peak activity in lake

sediments is known to have occurred from 1963-1964 AD (coincident with the hiatus of above-ground testing) (Ketterer et al., 2004). ^{210}Pb and ^{137}Cs analyses on 28, 0.5-cm-thick samples from surface cores HT01-B and GY02-A were performed by gamma spectrometry at the University of Southern California. All of the $^{239+240}\text{Pu}$, ^{210}Pb and ^{137}Cs analyses were performed on samples taken from the split core face.

Major-element geochemistry and shard morphology were used to characterize tephra deposits in cores HT01, GY03, and GY05 for use in tephrochronology. Tephras were located by their coarser grain size (fine sand) and high magnetic susceptibility. One tephra was identified in core HT01 at 180 cm; two tephras were located in core GY03 at 39 and 43 cm, and two in core GY05 at 18 and 67 cm. The major-element geochemistry and shard morphology were characterized for each of the five tephras to correlate the tephras in core GY05 with the tephras in cores HT01 and GY03, whose ages were inferred from nearby ^{14}C ages. Each tephra was sampled from the core axis, and wet-sieved through a 45 μm mesh to separate the coarser tephra grains. Once separated, the samples were heated to $\sim 80^\circ\text{C}$ in the presence of 30% H_2O_2 for 0.5 hr to remove any organic material. The tephras were then rinsed, dried, and mounted on two slides, one with epoxy, and the other with two-sided tape. The epoxy-mounted slides were sanded to expose smooth surfaces of the glass shards, and then carbon-coated for analysis on a Cameca MBX electron microprobe at Northern Arizona University. A single point on each of 58 glass shards from the five tephra deposits was analyzed, along with andradite and augite standards used to calibrate the microprobe prior to use. The total oxide percents of 10 elements were normalized to 100%. The morphology of the glass shards mounted on double-sided tape was documented using the scanning electron microscope

(SEM) at Northern Arizona University. The tephras were imaged using backscatter electron (BSE) imaging techniques; the SEM was operated at low vacuum (30 Pa) with an accelerating voltage of 20 kV.

Sedimentological and biological analyses

Magnetic susceptibility (MS) was measured at a 0.5 cm intervals on the split core faces using a Bartington MS2 surface meter. The cores were allowed to warm to room temperature before analysis. To determine whether the diffuse sediment laminations in both Hallet and Greyling Lakes corresponded to changes in density, thin slabs (0.4 cm thick) were taken from the core axis and imaged using X-radiography. Grain-size distributions were measured using a Coulter LS 230 laser diffraction particle-size analyzer. A total of 83 samples were taken from cores HT01 and GY05, and pretreated before analysis: The 0.2-0.4 g samples were heated overnight at 50°C with 10 ml of 30% H₂O₂ to remove organics, heated for 4 h at 80°C with 10 ml of NaOH to dissolve biogenic silica. The pretreated samples were deflocculated by adding 10-15 ml of hexametaphosphate and shaking for 0.5 h before analysis. The mass-percent of the >1 mm size fraction was determined for forty-two, 5-cm-thick sections of core HT01 using a 1 mm sieve and standard techniques.

Percent organic matter (OM) and bulk density were measured on 1 cm³ samples taken at 2.5 cm intervals from cores HT01 and GY05. The top 10 cm of surface core HT01B was sampled at 0.5 cm intervals to develop a higher-resolution record for comparison to instrumental climate records. Samples were dried overnight at 70°C, allowed to cool to room temperature, and weighed to determine bulk density. The

samples were then heated to 550°C for 5 h, cooled to room temperature in a desiccating chamber, and weighed to determine loss on ignition, which was used to approximate mass-percent OM.

Biogenic silica (BSi) was measured using wet-alkaline extraction techniques (Mortlock and Froelich, 1989). Samples were taken from the top 2 m of core HT01 at 1 cm intervals and at 5 cm intervals over the bottom 2.5 m of the core. Each sample was 0.5 cm thick, and taken from the core axis. The top 9 cm of surface cores HT01B and GY02A were sampled at 0.25 cm intervals to develop a high-resolution record for comparison to instrumental climate records. Samples were dried and ground to powder; large samples (~200 g) were used for analysis because of the low BSi content in the sediment, and to reduce the effects of sample heterogeneity. The samples were pretreated to remove organic material (shaken overnight with 5 ml of 30% H₂O₂) and carbonate (shaken for 1 h with 5 ml of 1 M HCl). BSi was extracted with 40 ml of 10% Na₂CO₃ (4 h at 85°C), and concentrations determined using absorbance measured by a spectrophotometer, following the procedure of Mortlock and Froelich (1989). A large reference sample taken from core HT01 was homogenized and run twice with each batch; the results were used to account for batch effects. BSi concentrations (%) were converted to flux (mg cm⁻² yr⁻¹) by multiplying %BSi by total flux (the product of bulk density and sedimentation rate).

Results

Glacial history

Hallet Valley

A map of the moraine sequence for the glacier forefield, including lichen stations and ages, is presented in figure 4a. A total of 183 lichens with nearly circular thalli were measured. Maximum lichen thalli sizes for individual landforms ranged from 15 to 68 mm, corresponding to ages ranging from 980 ± 200 to 1920 ± 20 AD (Table 3). With the exception of one station located high on the largest lateral moraine of glacier HTG1 (figure 4a), the lichenometric ages indicate that all of the prominent, bouldery moraines in the southern end of the valley stabilized after ~ 1500 AD, suggesting that the moraines formed during the LIA. Moraines deposited by glaciers on the west side of the valley suggest a limited LIA advance (figure 4a), and lichen ages (1870-1920 AD) indicate that the moraines stabilized more recently. Also, in contrast to the moraine sequence in the southern part of the valley, older moraines are preserved beyond the LIA extent in these cirques (figure 4a). These moraines were degraded, with lower crests and smaller, weathered, and more rounded boulders. Despite the presence of large lichens on the landforms (120-150 mm), an accurate lichen age could not be obtained because of the non-circular growth patterns of the lichens, and because of the decreased certainty with which numerical ages may be obtained from larger lichens (Solomina and Calkin, 2003). However, among the control points used by Solomina and Calkin (2003) to develop the growth curve is a 130-mm-diameter lichen that was dated by ^{14}C to 2870 cal BP (Denton and Karlén, 1973; Solomina and Calkin 2003). This age is therefore adopted for these landforms. Moraines with similar lichen sizes and weathering features occur in all four

cirques in the western part of the watershed (figure 4a). In cirques 6 and 7, they occur beyond the maximum LIA moraines, and in cirques 8 and 9, they form the moraines closest to the cirque headwalls. These cirques lack modern glaciers and glacial deposits indicative of a LIA advance (figure 4a).

Greyling Valley

A map of the moraine sequence for the valley, including lichen stations and ages, is presented in Figure 4b. A total of 165 lichens with nearly circular thalli were measured; maximum lichen thalli sizes for individual landforms ranged from 8 to 46 mm, corresponding to ages ranging from 1590 ± 80 to 1950 ± 10 AD (Table 3). The lichen ages suggest that all of the bouldery moraines near Upper Greyling Lake are associated with LIA glacier advances. The LIA moraine sequence records a complex history of advance and retreat from the multiple cirques: the west tongue of glacier GYG1 experienced limited advance compared with the other glaciers in the valley, but was the only glacier to preserve a record of several moraines deposited progressively down-valley during the LIA. Lichenometric ages suggest the glacier underwent several episodes of advances and standstills from 1630–1850 AD, when it reached its full extent, coalescing with the glacier emanating from the east near Upper Greyling Lake. The moraine record suggests that the east tongue of glacier GYG1, and the other glaciers in the valley (which are much larger than the west tongue of GYG1) reached their LIA maximum extents earlier, between 1590 and 1730 AD. Recessional moraines record the pauses during the retreat of these larger glaciers, and suggest that most of the recession from the LIA maximum extents occurred during the past 100 yr. The lichenometric age from a small

recessional moraine near the modern terminus of glacier GYG3 indicates the landform stabilized ~1945 AD. This moraine lies within the glacier extent shown on the 1951 USGS topographic maps, and suggests either an error in the USGS map, or an overestimate of the lichen age. While the glacier extents on topographic maps are often inaccurate at this scale, the discrepancy allows for an evaluation of the maximum error in the lichen ages. The 1978 air photographs show that the glacier had receded upvalley of the moraine by 1978; therefore if the lichen age is incorrect, it overestimated the age by < 30 yr. While this is beyond the $\pm 20\%$ error range assumed for lichenometric ages (± 12 yr), uncertainty in the local colonization time has disproportionately large effects on the youngest ages, so errors of this magnitude may be expected. Alternatively, this may indicate an error in the colonization time used in the growth curve. Because the curve was developed for a region with a more continental climate, a shorter colonization time may be expected for the study area, and would explain the discrepancy between the lichen ages and aerial photo evidence.

Equilibrium-line altitudes

ELAs for the study areas ranged from 1410-1650 m for the modern glaciers, and 1280-1610 m for the LIA glaciers (figure 6; Table 4). The calculated ELAs for both the modern and LIA reconstructions tend to rise to the west (3 m km^{-1} , p-value = 0.009) (figure 8). The average ELA lowering (ΔELA) was 86 ± 61 m ($n = 7$) near Hallet Lake, and 82 ± 38 m ($n = 14$) near Greyling Lake. Because the ΔELA values are essentially equal, all 21 glaciers are used to estimate the ΔELA for the area (83 ± 44 m, $n = 21$).

Lake sediments

Geochronology

Tephrochronology

Among the five tephra layers, there are two distinct populations; “Greyling tephra” (tephra layers GY03 39 cm and GY05 18 cm) was relatively silica-poor (60 ± 3 wt. % oxide), but enriched in FeO and MgO (7 ± 2 and 3 ± 1 wt. % oxide, respectively) (figure 9; Table 5). Two other tephra layers (GY05 67 cm and HT01 180 cm) compose the second distinct population, referred to as the “Hallet tephra”. These tephra layers were more rhyolitic, with more SiO₂ (79 ± 4 wt. % oxide) and less FeO and MgO (1.5 ± 0.5 and <1 wt. % oxide, respectively). The tephra layer GY05 67 cm was distinct from the others analyzed, containing two separate geochemical populations. Most of the analyzed glass shards fell in the range of the “Hallet tephra”, but 4 of the 15 shards were silica-poor (48 ± 7 wt. % oxide) and enriched in FeO and MgO (11 ± 3 and 15 ± 1 wt. % oxide, respectively). The composition of tephra layer GY03 43 cm was intermediate between the two populations, and was the most heterogeneous of the five tephra layers analyzed, SiO₂ ranged from 60-73 wt. % oxide, and FeO and MgO ranged from 2-6 and 0-2.5 wt. % oxide, respectively (figure 9, Table 5).

Shard morphology was also useful in correlating tephra layers. Layers GY03 39 cm and GY05 18 cm were both primarily composed of pumicey glass shards of near-uniform size and shape; most grains were roughly equidimensional, typically ~ 100 μm in diameter (figure 10). Tephra layers GY05 67 cm and HT01 180 cm also contained pumicey shards, but were distinguishable from GY03 39 cm and GY05 18 cm because they contained many larger (150-250 μm), elongated shards, with a ribbed-wall texture

(figure 10). The shard morphology of layer GY03 43 cm was significantly different than the four other tephra layers. The shards were smaller (50-100 μm) with very few pumicey grains (figure 10). Most of the shards had smooth faces, with bubble-wall textures.

The major-element geochemistry and the shard morphologies indicate that the tephra in core GY05 at 18 and 67 cm can be correlated with the tephra at 39 cm in core GY03, and the tephra at 180 cm in core HT01, respectively. The age of the GY03 39 cm tephra has been inferred to be ~1200 AD using a linear sedimentation rate between a ^{14}C age at 52 cm and the surface. The HT01 180 cm tephra is dated at ~30 AD by a ^{14}C age directly above the tephra (Table 2).

Hallet and Greyling Lakes age-depth models

An age-depth model for the core HT01 was developed using all nine ^{14}C ages, as well as one $^{239+240}\text{Pu}$ age (3.25 cm = 1963), and the surface age (0 cm = 2006) obtained from the companion surface core (HT01-B) (Tables 2 and 6). A thin marker layer in both core HT01 and surface core HT01-B indicates that 2.25 cm of sediment was lost from the top of the core HT01; depths in the age model were adjusted accordingly. In some cases, the onset of global fallout from thermonuclear weapons testing, such as $^{239+240}\text{Pu}$, can be used to identify a 1953/1954 horizon in lacustrine sediments (Ketterer et al., 2004). The onset of $^{239+240}\text{Pu}$ is not used in the Hallet Lake chronology, because the depth of onset (5.0 cm) would indicate a period of very high sedimentation rates from 1954-1963, while the core stratigraphy and the smooth $^{239+240}\text{Pu}$ profile (figure 11) suggest relatively steady sedimentation through the interval. It is possible that the $^{239+240}\text{Pu}$ diffused after

deposition, causing the depth of onset to be artificially low (M. Ketterer, personal communication).

The ^{210}Pb and ^{137}Cs inferred ages were not used in the age model. The activities of each were low (<0.27 and <0.13 Bq g^{-1} , respectively), which is typical of sediment in glacier-fed lakes, especially those in the Arctic where the ^{210}Pb flux is lower; this has been recognized as the single largest problem associated with ^{210}Pb dating in polar regions (Wolfe et al., 2004). In addition, the analyses were performed using gamma spectrometry, which is less efficient than alpha counting, and may not be appropriate for ^{210}Pb analyses in low activity sediments (J. Smol, personal communication). This is probably the cause of the atypical ^{210}Pb profile; activities decrease rapidly from 0-2 cm, but then increase from 2.5-4.5 cm (figure 11). The ^{137}Cs profile shows a well-defined peak at 1.75 cm, which would suggest an average sedimentation rate of 0.41 mm yr^{-1} over the past 43 yr, nearly half the $^{239+240}\text{Pu}$ -inferred sedimentation rate of 0.76 mm yr^{-1} over the same time interval. I believe that the $^{239+240}\text{Pu}$ -inferred sedimentation rate is more likely to be accurate, because $^{239+240}\text{Pu}$ is less mobile in lake sediments than ^{137}Cs (Crusius and Anderson, 1995), the peak $^{239+240}\text{Pu}$ activities are much higher than the peak ^{137}Cs activities (2350 and 0.12 Bq g^{-1} , respectively), and the $^{239+240}\text{Pu}$ -inferred sedimentation rate (0.76 mm yr^{-1}) is more consistent with the well-defined, average sedimentation rate over the past 2 kyr determined by ^{14}C (0.93 mm yr^{-1}), while the ^{137}Cs -inferred sedimentation rate is much lower (0.41 mm yr^{-1}).

Seven ^{14}C ages, and two tephra ages were obtained for core GY05, as well as the surface age (0 cm = 2006) obtained from the companion surface core (Table 2). Several fine layers deposited in both core GY05 and surface core GY05-A indicate that 1 cm of

sediment was lost from the top of core GY05. The age from 100 cm was rejected because it fell off the well-defined nearly linear trend set by the four ages nearest to it in the core. The age from 260 cm was rejected because it suggested that the bottom of the core may have been deposited nearly 25 ka; this is considered unlikely, as regional glacial records of Pleistocene deglaciation suggest that the Chugach Range was occupied by extensive ice through the late-Wisconsinan (Hamilton and Thorson, 1983; Kaufman and Manley, 2004). The age from 260 cm also suggests that the sedimentation rate below 230 cm was remarkably low (0.05 mm yr^{-1}), especially considering that the core stratigraphy (figure 12) suggests that the sedimentation rate below 230 cm should be at least as high as above 130 cm (0.3 mm yr^{-1}). Because the age at 260 cm was rejected, and the age at 292 cm is poorly constrained, the age model is considered uncertain below 230 cm. None of the major conclusions of this study rely on the accuracy of these lowermost ages.

$^{239+240}\text{Pu}$, ^{210}Pb and ^{137}Cs in surface core GY02-A in the northern sub-basin exhibit complex behavior (figure 13; Table 6), and indicate that the sediment was either disturbed, or that the challenges associated with using these isotopes in Arctic settings described above were even more pronounced in Greyling Lake than in Hallet Lake. A best-estimate of the irregular profiles indicates a sedimentation rate of $\sim 1 \text{ mm yr}^{-1}$, however, the presence of the “Greyling” tephra at 25 cm in the surface core indicates that over that interval, the sedimentation rate was similar to the rate observed in core GY05 in the central basin ($\sim 0.3 \text{ cm yr}^{-1}$). In the southern basin, the sediment traps captured the equivalent of $\sim 0.15 \text{ mm}$ from June 2004 to August 2005, and $\sim 0.1 \text{ mm}$ from August 2005 to July 2006, suggesting that sedimentation rates may be uniformly low throughout the lake.

A smoothed cubic spline function was used to model the age-depth relation in cores HT01 and GY05 (Heegaard et al., 2005) (calculations were performed by the statistical software R (<http://cran.r-project.org/>; last accessed 7 March, 2007)) (figure 14). The routine also calculates confidence intervals at any point in the core. Following Heegaard et al. (2005) the 95% error bands were calculated using three parameters from each control point: 1) the 1σ calibrated age ranges, 2) the analytical uncertainty, and 3) the depth range from which the sample was obtained (Table 2). The spline fit function requires a coefficient (K value), which controls the flexibility of the modeled curve. K values range from 1 to $n-1$ (n = the number of age control points); higher K-values increase the ability of the curve to accommodate the dated levels. A K value of 10 was chosen for core HT01, and 7 for core GY05, each because it resulted in the most realistic curve that fit the control points (figure 14).

Sedimentological and biological analyses – Hallet Lake

Lithostratigraphy

Core HT01 is dominated by silty mud, and is weakly laminated throughout the core (0.1- to 2-cm-thick laminations) (figure 15). The laminations are defined by changes in color, and occasionally slight changes in texture. The bottom of the core (450-340 cm) consists of dark-gray (10YR 2/1) silty mud, with abundant angular rock fragments. Laminated, dark-gray (10YR 2/1) mud with few rock fragments is present from 340-160 cm. Above 160 cm, the laminations thin, and the sediment color varies from light gray (10YR 3/1) to light tan (10YR 4/6). One light-pink (10R 9/1) tephra layer (0.5 cm thick) is located at

180 cm. A 2.5-cm-thick deposit of nearly pure organic material (plant fragments) is located at 10.5 cm.

Magnetic susceptibility

The magnetic susceptibility (MS) profile is characterized by a relatively constant background level ($\sim 30 \times 10^{-6}$ SI) punctuated by a single large peak ($\sim 250 \times 10^{-6}$ SI) corresponding to the single tephra layer at 180 cm (figure 15). Below 327 cm, the background level decreases ($\sim 20 \times 10^{-6}$ SI). This is consistent with the increase in concentration of stone fragments, which have low MS, and dilute the signal of the fine-grained matrix (figure 15).

Grain size

Considering the downcore variability in rock fragments in core HT01, the lack of significant trends in grain-size distribution in the sediment matrix is unexpected (figure 15). The single-point peaks, especially below 200 cm, reflect the incorporation of a relatively small amount of sand-sized particles ($>50 \mu\text{m}$); the grain size of the silt and clay matrix of the sediment appears to remain relatively constant down-core. As expected, the >1 mm fraction does exhibit higher percentages of pebbles and cobbles below 340 cm, which is consistent with the low MS values (figure 15).

Bulk density

Bulk density ranges from 0.7 to 1.9 g cm^{-3} in core HT01. A 5-point (~ 100 yr) running mean was used to emphasize longer-term variability in bulk density (figure 15). The bulk

density fluctuates between ~ 1.2 and $\sim 1.8 \text{ g cm}^{-3}$ over the top 350 cm of the core, below which it primarily varies between ~ 0.8 and $\sim 1.2 \text{ g cm}^{-3}$.

Organic-matter content

OM in core HT01 ranges from 2.5 to 7.3% (figure 15) (one measurement was excluded as a clear outlier (10.7%)). To emphasize centurial-scale changes, OM is presented as a 5-point (~ 100 yr) running mean. OM in the core is generally low, emphasizing the importance of minerogenic sediment input from the nearby glaciers, and the low productivity of the lake and watershed. OM varies between 2.5 and 4.5% over the top 340 cm of the core, exhibiting an overall decrease towards the top of the core. Below 340 cm OM dramatically increases, and is consistently higher below 340 cm than anywhere else in the core. OM is inversely related to bulk density ($r = -0.82$), and this correlation improves between the running means ($r = -0.93$).

Biogenic silica

BSi flux in core HT01 varies from 0.1 to $4.9 \text{ mg cm}^{-2} \text{ yr}^{-1}$ (figure 15). The data were filtered to remove four extreme outliers not related to decadal-scale climate variability. Above 380 cm, BSi flux fluctuated between ~ 0.5 and $2.0 \text{ mg cm}^{-2} \text{ yr}^{-1}$, with intervals of high flux between 200-140, 85-50, and 10-0 cm. Below 380 cm, BSi flux is much higher, ranging from 1.0 to $5.0 \text{ mg cm}^{-2} \text{ yr}^{-1}$.

Sedimentological and biological analyses – Greyling Lake

Lithostratigraphy

Core GY05 consists of three main stratigraphic units (figure 12): Unit I, the basal unit (350-230 cm) is composed of gray (5GY 3/1) silty mud, which is generally not laminated, although a zone with well-defined lamina (0.5- to 1-cm-thick) is located from 350-330 cm. Two large rocks (7 and 10 cm long, 7 cm wide) were recovered in this unit, from about 250 and 330 cm. Unit II (130-230 cm) is grayish-green (5GY 6/3) gyttja, with a sharp contact at the base, and a gradational contact at the top. Unit III (0-130 cm) is thinly bedded, gray to dark-gray clayey mud. Two fine-grained tephra are visible in this unit, a light-pink (10R 9/1), 0.25-cm-thick layer at 67.5 cm, and a dark-gray (5GY 1/1) 0.25-cm-thick layer at 18.5 cm.

Magnetic susceptibility

The average background level in the MS profile is $\sim 20 \times 10^{-6}$ SI (figure 12). It is lowest (~ 5 to $\times 10^{-6}$ SI) from ~ 230 -200 cm, and increases towards the surface (to ~ 30 to $\times 10^{-6}$ SI). The background is ~ 20 to $\times 10^{-6}$ SI from the bottom of the core to 230 cm, where it rapidly decreases; this shift is consistent with the abrupt change from lithostratigraphic unit I to unit II (figure 12). There are several peaks in MS, especially above 140 cm. The highest peak (222×10^{-6} SI) at 67.5 cm corresponds to a prominent tephra layer. The only other visible tephra also corresponds with a peak in MS (67 to $\times 10^{-6}$ SI) at 18.5 cm.

Grain size

Median grain size in core GY05 varies from ~1.5–3.2 μm (figure 12). Down-core changes in grain size can be subdivided into three zones, consistent with the lithostratigraphic units: at the bottom of the core, 340–230 cm (Unit I), grain size is fairly constant, and the coarsest in the core (median = ~2.75 μm). From 230–130 cm (Unit II), median grain size gradually decreases (~2.75 to ~1.5 μm). From 120–0 cm (Unit III), median grain size remains fairly constant, but slowly increases (from ~1.5 to ~1.8 μm). This unit contains the finest grain size in the core.

Bulk density

Bulk density ranges from 0.3 to 1.8 g cm^{-3} in core GY05. Following the discussion for Hallet Lake, bulk density is also presented as a 5-point (~300–1000 yr) running mean (figure 12). The bulk density is high at the base of the core (~1.6 g cm^{-3}), decreased rapidly to its lowest value (~0.3 g cm^{-3}) around 215 cm, then gradually increases to the top of the core. Zones of higher bulk density coincide with dark-gray glacial silt and clay (Units I and III) (figure 12).

Organic-matter content

OM in core GY05 ranges from 2.1 to 9.7% (figure 12). Following the discussion for Hallet Lake, OM is also presented as a 5-point (~300–1000 yr) running mean. OM is low at the base of the core (~2.5%), and then increases rapidly to its maximum (~9.5%) at ~215 cm. OM gradually decreases toward the top of the core. OM is well correlated with

bulk density ($r = -0.85$); the correlation improves between the running means ($r = -0.91$). Over the past ~4.3 kyr OM in cores HT01 and GY05 are remarkably similar (figure 16).

Climate correlations

Meteorological data

Daily mean temperature, precipitation, snowfall and snow depth data from Valdez (1917-2005), Gulkana Airport (1943-2005), and Tonsina Lodge (1963-2005) were obtained from the National Climatic Data Center (NCDC, 2007). Monthly, seasonal, and annual averages were calculated using daily values, which allowed the reliability of the averages to be evaluated by comparing the number of days that contributed to the mean to the total possible. Only averages based on measurements for >90% of the days in the period were used in the correlations.

An air-temperature logger was installed near the northern shore of Greyling Lake (figure 3b) in August 2005, and recorded air temperature once an hour from August 5, 2005 through July 6, 2006. The logger was mounted on a wall-tent frame, which broke during the winter; the logger was apparently buried in snow from March 16 to May 26, 2006. Consequently, the temperatures measured during this time could not be used, but the logger did record the timing of the spring melt. Daily average temperature measured at Greyling Lake correlates well with the instrumental record from Valdez ($r = 0.96$) and Gulkana ($r = 0.95$) (figure 17). This suggests that the instrumental records provide a fair approximation of temperature at the lakes over the past 100 yr.

Climate correlations between sediment proxies and climate parameters

Simple, single-variable regressions were used to evaluate the correlations between measured BSi flux and OM at Hallet Lake, and the monthly, seasonal and annual average weather parameters from the three instrumental records, the Tonsina River discharge data, and three climate indices from the northern Pacific Ocean: the Aleutian Low Pacific Index (ALPI) (Beamish et al., 1997), the North Pacific Index (NPI) (NCAR, 2007), and the Pacific Decadal Oscillation Index (PDOI) (Mantua et al., 1997). Ages were assigned to the high-resolution BSi flux and OM measurements used for correlation by assuming that the average sedimentation rate suggested by the depth of the well-defined peak in $^{239+240}\text{Pu}$ activities (known to be centered on 1963-1964 (Ketterer et al., 2004)) was constant through the last 100 yr (~8 cm). Because of limitations in sampling, individual measurements of both BSi and OM represent more than a single year (BSi = ~4 yr, OM = ~7 yr). To compensate for this effect, regressions were performed with 5- and 7-year (BSi and OM, respectively) running averages of the instrumental weather parameters. This allowed direct comparison between the datasets, since both integrate multiple years, and reduced the effects of errors in the assigned ages.

High-resolution measurements of OM and BSi flux from the top 10 cm of surface core HT01-B (sister core of HT01) were correlated with the suite of instrumental climate records from Valdez and Gulkana and with published climate indices for the north Pacific region (Table 7). OM correlates with the Aleutian Low Pressure Index (ALPI) ($r = 0.66$) and Gulkana and Valdez winter (DJFM) temperature ($r = 0.63$ and $r = 0.75$, respectively). The strength of this correlation is limited by the low-resolution sampling used for OM,

and by the length of the instrumental records. Nevertheless, many of the major shifts in OM over the past 100 yr occurred when the AL changed phase (figure 18).

The strongest correlation between any of the measured proxies and climate parameters is the direct correlation between BSi flux and Valdez summer (JJA) temperature ($r = 0.84$) (figure 19) (Table 7 and 8). On the basis of this strong correlation, a transfer function was developed to quantitatively reconstruct summer temperature for the past 2 kyr from the BSi flux from core HT01. BSi concentrations are known to be related to lake temperature, light and nutrient availability, and summer temperature may have direct and indirect effects on all three factors (Anderson, 2000). In competitive environments, water temperature tends to be less important to diatom growth than the other factors (Anderson, 2000). Productivity in Hallet Lake is low; competition for the available nutrients is probably limited, and the sub-arctic summers probably provide abundant light for the small diatom crops. Consequently, water temperature may be more of a limiting factor at Hallet Lake than other locations, and summer water temperature may have a direct control on the abundance of BSi deposited each year. Summer water temperature at Hallet Lake is probably closely tied to summer air temperature; water temperature sensors at Greyling Lake indicate that water temperature is sensitive to changes in air temperature, responding with a four-day lag (figure 20).

Quantitative summer temperature reconstruction

BSi flux increases exponentially with temperature over the calibration period (figure 19).

A classical logarithmic regression was used to develop a transfer function.

$$T_{\text{JJA}} (^{\circ}\text{C}) = \frac{\left(\text{Log}_{1.000624} \left(\frac{\text{mg}_{\text{BSi}} \text{ cm}^{-2} \text{ yr}^{-1}}{0.465} \right) \right)^{\frac{1}{3}} - 0.99}{0.914}$$

To minimize the effects of point-to-point variability, and to emphasize longer-term changes in temperature, a 50-year Gaussian-weighted low-pass filter was applied to the high-resolution record of BSi flux before using the transfer function to reconstruct summer temperatures for the past 2 kyr. The BSi flux-inferred summer temperatures for the past 2 kyr range from 9-14°C; the average of the unfiltered data for the past 2 kyr is 10.6°C (10.7°C for the filtered data), nearly 2°C cooler than the modern average temperature (12.4°C) (figure 21); here defined as 1976-2005, the period of continuous measurement during the current AL regime. Comparisons of the observed and predicted values, along with the residuals show that the transfer function tends to slightly underestimate the highest and lowest temperatures (figure 19). The transfer function was cross-validated using both jackknife and bootstrap techniques; $r^2_{(\text{jack})} = 0.68$, $r^2_{(\text{boot})} = 0.69$. The root mean square error of prediction (RMSEP) was also calculated using the two techniques ($\text{RMSEP}_{(\text{jack})} = 0.69^{\circ}\text{C}$, $\text{RMSEP}_{(\text{boot})} = 0.67 - 1.31^{\circ}\text{C}$) (Birks, 1995). The $\text{RMSEP}_{(\text{boot})}$ calculated for each point in the record of BSi flux was used to provide a dynamic estimate the error for the temperature reconstruction, which varies with temperature (figure 21) (Birks, 1995).

Climate variability at Hallet and Greyling Lakes

Climate variability over the past 2 kyr

The multi-proxy approach used in this study provides insight into multiple aspects of late Holocene climate. The correlations between OM and the ALPI and Valdez and Gulkana

winter temperature (Tables 7 and 8) suggest that the strength of the AL controls the input of detrital organic material and nutrients into the lake, affecting OM. While the mechanisms that drive this relation are not well understood, several processes may have an important effect on OM concentration in the lake sediment. Enhanced winter precipitation probably results in more avalanches, which may bring detrital OM from the hillslopes to the lake. In the Gulf of Alaska years with strong AL tend to be associated with warmer winter temperatures (Mock et al., 1998; Rodionov et al., 2005), allowing for earlier melt out and a longer growing season the following summer. Abundant wind-blown organic matter was present on the snow pack and lake ice around Hallet Lake during the 2006 field season; a strengthened AL might increase the amount of wind-blown organic material deposited in the lake, enhancing the relation between OM and the AL. The similarities between fluctuations in OM in independently dated cores from Greyling and Hallet Lakes over the past ~4.3 kyr suggest that the sediment at each lake record regional climate variability (figure 16). This also suggests that the age models for this part of each record are robust.

The record of AL strength and winter temperature inferred from OM compliments the BSi-inferred reconstruction of summer temperature from Hallet Lake. Together, they provide information on winter precipitation and summer temperature, the two parameters most strongly linked to glacier health (Ohlendorf et al., 1997; Nesje et al., 2001). This allows for direct comparison to geomorphic evidence of glacial advances and ELA lowering during the LIA, which provide independent information about late Holocene climate in the study area.

First millennium AD cooling

Reconstructed summer temperatures are warmer than the average for the past 2 kyr (10.6°C) from ~100 to ~500 AD, before decreasing rapidly to ~2°C below average by 600 AD (figure 21). The cooling from 480 to ~600 AD coincides with glacial advance in southern Alaska. Glacier forefields in the Chugach Range, as well as the Kenai and St. Elias Mountains, show evidence of First Millennium AD (FMA) advances (Wiles et al., 2007). Radiocarbon ages from glacially overrun trees suggest that the main interval of advance was between 590 and 650 AD; an age of 430 AD is the earliest evidence of glacial expansion for the coastal mountain ranges (Wiles et al., 2007). The timing of the cooling inferred from Hallet Lake is consistent with other regional and hemispheric temperature reconstructions as well, although the amount of temperature change is significantly less in the hemispheric reconstructions (~0.1°C compared to ~2°C) (figure 22) (Hu et al., 2001; Mann and Jones, 2003; Moberg et al., 2005). The difference in amplitude in temperature variability between Alaskan sites (Hu et al., 2001; this study) and Northern Hemisphere reconstructions (Mann and Jones, 2003; Moberg et al., 2005) is probably due to the effects of averaging a number of records over large area which did not experience simultaneous changes in climate. Polar amplification of climate variability may have had an additional effect, enhancing the variability in temperature at the Alaskan sites.

Percent OM exhibits similar trends over the last 2 kyr, with high values from 0 – 200 AD, increasing to a local maximum from ~200 to ~500 AD before decreasing significantly from ~500 to ~700 AD (figure 22). OM begins to decrease after the BSi-inferred summer temperatures, remaining relatively high from 550-600 AD, by which

time summer temperature had reached its minimum ($\sim 2^{\circ}\text{C}$ below average). The higher OM content suggests an enhanced AL. This combined with the low summer temperature may have contributed to the glacier expansion observed throughout the Gulf of Alaska at this time (Wiles et al., 2007).

Medieval Warm Period

After ~ 600 AD, summer temperature gradually increased ($\sim 1.5 - 0.5^{\circ}\text{C}$ below average) through ~ 1100 AD, before rapidly increasing to $\sim 1^{\circ}\text{C}$ above the 2-kyr average by 1300 AD, and remained above average until ~ 1500 AD (figure 21). While the BSi-inferred temperature reconstruction from Hallet Lake suggests warming throughout the period, summer temperature did not reach its maximum until 1300-1500 AD. The Medieval Warm Period (MWP) is classically considered to have occurred significantly earlier, from ~ 950 to ~ 1200 AD (Brazdil et al., 2005); however, many studies have emphasized the spatial and temporal heterogeneity of the warm period (e.g., Hughes and Diaz, 1994; Jones and Mann, 2004). A recent study by Osborn and Briffa (2006) demonstrated that the Northern Hemisphere experienced a period of general warmth from 950 to 1200 AD, but that it was not a continuous 250 yr interval of warm climate. Rather, it comprised several multi-decadal periods of consistent warmth separated by periods of spatial heterogeneity (i.e., some records indicate warm temperature, others cold). The study also found that a significant warm anomaly from 1350 – 1450 AD occurred broadly across the Northern Hemisphere. This is consistent with the warming observed between 1300 and 1500 AD in Hallet Lake.

In southern Alaska, only a few studies have presented well-constrained evidence for the timing and magnitude of the MWP (Hu et al., 2001; Loso et al., 2006; Wiles et al., 2007). Tree-ring chronologies from recently uncovered subfossil wood in glacial forefields in the Chugach and Kenai Mountains (figure 1) suggest continuous forest growth from ~900 to ~1300 AD in areas that were covered with ice during the FMA and the LIA (Wiles et al., 2007). The quantitative temperature reconstruction from Farewell Lake, in the foothills of the northwestern Alaska Range (figure 1), developed by Hu et al. (2001) indicates a period of increased temperature (~0.5°C cooler than modern) from ~800 to 1500 AD. The 1600-yr varve sequence from Iceberg Lake in the eastern Chugach Mountains (figure 1) contains a period of increased varve thickness from 1000 to 1300 AD (Loso et al., 2006). The Wolverine tree ring-width series from near Wolverine Glacier on the eastern Kenai Peninsula (figure 1) suggests periods of warmth centered on 1300 and 1450 AD, but the record only goes back to ~1250 AD (Barclay et al., 1999). The period of warmth inferred from the Hallet Lake BSi record from 1300-1500 AD is generally consistent with other records in the region, but the cooler summer temperature between 900 – 1200 AD is not consistent with other records of warm-season temperature from the area.

OM remains low until ~900 AD, and then quickly increases before leveling off at ~1050 AD (figure 22). The values remain high until ~1350 AD before decreasing again. The differences in the BSi-inferred temperatures compared to OM suggest that the AL strength increased ~200 yr before summer temperature began to warm significantly, and weakened ~100 yr before summer temperatures began to cool. The OM record shows strong similarities to the varve thicknesses from Iceberg Lake over this time interval

(figure 22) (Loso et al., 2006). Loso et al. (2006) attribute the variability in the varve thicknesses to sediment transport capacity and shoreline elevation, relating both of these mechanisms to spring and summer temperatures. Winter precipitation likely has a significant effect on lake level as well as sediment transport capacity during the spring melt. If so, then the similarity between the OM records presented in this paper and the varve-thickness record from Iceberg Lake suggests regional synchronicity in the strength of the AL.

The paleoclimate records from Hallet Lake suggest that the region did not experience a classic Medieval Warm Period. Instead, summer temperature increased through this period, but did not peak until after the period typically cited. The OM record does indicate a climate anomaly from ~900-1350 AD (figure 22), consistent with the timing of the MWP. This suggests that the region experienced increased AL strength during the MWP, while summer temperature did not reach its maximum until 1300-1500 AD (figure 21).

Little Ice Age

Summer temperature began to decrease at ~1450 AD, cooling by more than 2°C by ~1875 AD (figure 21). The maximum cooling at Hallet Lake occurred from ~1750 to ~1900 AD. The LIA in southern Alaska has been divided into three phases (early, middle, and late) based glacial evidence and tree-ring chronologies (Wiles et al., 1999; Barclay et al., 2002). The BSi record from Hallet Lake indicates cooler temperatures during the middle and late phases, with the coldest temperatures of the LIA occurring during the late phase, consistent with most extensive glacier advance of the period (Wiles

et al., 2007). Several tree-ring chronologies from southern Alaska identify major cool periods during the 18th and 19th centuries, commonly the coldest in the record (Cropper and Fritts, 1981; Barclay et al., 1999; Davi et al., 2003).

OM began to decline rapidly at ~1350 AD, reaching its lowest value for the past 2000 yr by ~1550 AD. OM remained low through 1750 AD before increasing to modern values (~3.5%) (figure 22). The low OM values suggest a weakened AL throughout the LIA. A weakened AL during the LIA is supported by evidence from glaciers near Greyling and Hallet Lakes, which suggest that the LIA glaciers received less winter precipitation than modern glaciers in the area. Temperature records from Greyling Lake and Valdez during 2005-2006 were used to derive an environmental lapse rate of $-7^{\circ}\text{C km}^{-1}$ for the area. In this study, glacier geometry was used to estimate (using the AAR method) ELAs based on the 1978 glacier extents. Consequently, the calculated ELAs are controlled by the integrated effects of climate over the few decades prior to the 1978 aerial photographs. The period from 1950-1978 AD was on average 1.5°C warmer than during the maximum LIA cooling. This, combined with the environmental lapse rate, suggests that ELA should have lowered by ~210 m. The maximum ELA lowering calculated using the maximum LIA extents and the AAR method is 83 m. This ΔELA is a realistic maximum estimate, and is relatively insensitive to changes in AAR; to achieve the environmental lapse rate-inferred lowering of ~210 m, the modern AAR would have to be ≤ 0.05 . This is substantial evidence indicating that the ELA lowering and the LIA glacier advances in the region were limited because of reduced winter precipitation, consistent with a weakened AL inferred from the low OM during the LIA. Evidence for

reduced winter precipitation during the LIA has been identified in other records from southern Alaska (Levy et al., 2004; Daigle et al., 2006; Kathen et al., 2006).

20th century warming on the basis of the BSi-inferred temperature record

Summer temperature at Hallet Lake has increased $\sim 3.5^{\circ}\text{C}$ in the 130 yr since the coldest part of the LIA (figure 21). The most dramatic difference between 20th century warming, and the warming leading into the MWP, and the warm period from 1300-1500 AD is the rate of temperature change. It took 850 yr, from 550 to 1400 AD, for temperature to warm from 9 to $\sim 12^{\circ}\text{C}$. In contrast, during the past 130 yr, temperature has increased from ~ 10 to $\sim 13^{\circ}\text{C}$. The reconstructed temperatures for the past 20 yr are the highest for the past 2000 yr at Hallet Lake. Some of the glaciers in the Hallet valley have retreated more than 1 km since 1951 (figure 4), despite the increase in winter precipitation associated with increased AL strength. This rapid 20th century warming is observed consistently throughout southern Alaska, in tree-ring chronologies, lake records, and glacial records (Hu et al., 2001; Davi et al., 2003; Loso et al., 2006; Wiles et al., 2007).

Climate variability from 15 – 2 ka

The Hallet Lake OM and BSi records extend as far back as 7.7 ka; however, before 4.8 ka (below 340 cm), OM, BSi and the mass % >1 mm are much higher than elsewhere in the core (figure 15). The timing of this shift coincides with when the OM records from Hallet and Greyling Lakes begin to vary with remarkable synchronicity (figure 16). Before 4.8 ka, the OM records are similar, but much less so than after 4.8 ka. OM and BSi may have responded to climate in the same way before 4.8 ka as they did during the past 2 kyr; the

high OM and BSi values correspond to enhanced AL strength and higher summer temperatures. The BSi flux values before 4.8 ka are about two times higher than modern values, and as much as five times higher than the average value for the past 2 kyr (figure 15); however, the correlation between BSi flux and summer temperature indicates that BSi flux increases exponentially with increasing temperature (figure 19). Applying the transfer function to the highest BSi flux values suggests a 2-3°C increase in summer temperature relative to the average temperature from 1976-2005, consistent with estimates of Holocene thermal maximum warming in Alaska (Kaufman et al., 2004). High OM before 4.8 ka may be associated with a strengthened AL and consequently, enhanced winter precipitation, which, combined with the increased summer temperature may have promoted mass wasting on the steep, weakly endurated hillslopes on either side of the lake, explaining the abundance of rock fragments in the core before 4.8 ka. This inferred period of increased mass wasting suggests that the lake formed shortly prior to the deposition of the sediment recovered from the bottom of core HT01, because the lake is dammed by several large debris avalanche deposits near the mouth of the valley (figure 2). If so, this provides an alternative explanation for the high OM and BSi values, since the flooded valley floor would provide abundant nutrients and OM relative to the modern lake system. However, this hypothesis does not explain the rapid decrease in OM, BSi and mass % >1 mm at 4.8 ka, and it seems unlikely that the flooded valley floor could support the high OM and BSi concentrations for nearly 3 kyr. Therefore, the Hallet Lake OM and BSi records from 7.7 to 4.8 ka are considered to be indicative of climate variability.

The difference in correlation between the OM from Hallet and Greyling Lakes before 4.8 ka is most likely related to the change from lithologic unit II to unit III in the Greyling Lake core at ~135 cm (4.8-4.7 ka) associated with decreased OM and increased sedimentation rates (figures 12 and 23). This shift probably signifies the expansion or return of glaciers to the catchment. Therefore, before 4.8 ka, major changes in vegetation in the valley, and the input of glacially-derived sediment may have had a more important effect on OM than AL strength.

Early Holocene warmth

Following the last glacial maximum, the sedimentation rate was high, OM was low and grain size was at its coarsest (figure 23). This is consistent with the influx of abundant glacially derived sediment, and the lack of vegetation in the watershed expected after the retreat of Wisconsinan glaciers. The coarser grain size suggests that Upper Greyling Lake (figure 4) remained occupied by glacial ice, and was probably not acting as a sedimentation trap, distilling out the coarser grains, as it does today. Between 14.5 and 14.0 ka, the sedimentation rate decreased, and OM began to rapidly increase, peaking by 11.5 ka. This is probably due to the colonization of the area after Pleistocene glacial retreat and the continued reduction of glacial input over the time interval. OM remained elevated through the low-sedimentation-rate, gyttja-textured section of the core (figures 12 and 23). There is no evidence for glacial advance during the Younger Dryas reversal in the OM record; in fact, the low sedimentation rates and high OM suggest that the glaciers at the head of the valley were dramatically diminished or entirely ablated from 13-5 ka (figure 23).

BSi flux in Hallet Lake was at its highest ($2.5\text{-}5.0 \text{ mg cm}^{-2} \text{ yr}^{-1}$) from the start of record, 7.7 ka, to 5.6 ka, consistent with diminished glaciers during the time interval (figure 24). Using the transfer function developed for this study, the increased BSi suggests summer temperature was $2\text{-}3^\circ\text{C}$ warmer than the average summer temperature from 1976-2005. Hallet Lake OM is also high during this time interval, suggesting that the AL may have been enhanced relative to modern from 7.7 to 5.6 ka (figure 24). High OM values, combined with low sedimentation rates, suggest a reduction in glacial sediment, likely related to a reduction of glacier extent in the valley from 7.7 to 3.8 ka (figure 22).

Neoglaciation

In Greyling Lake, the sedimentation rate increased and OM began to decrease ~ 4.3 ka (figure 23). The Hallet Lake OM record shows a similarly sharp decrease in OM beginning ~ 4.5 ka (figure 24), although a more dramatic decrease in OM occurred 5.2 ka (figure 24). BSi was generally low after 4.6 ka, suggesting cooler summer temperatures. This is interpreted as the onset of neoglaciation. Beginning 4.8 ka, the OM records from each lake began to fluctuate synchronously, each steadily decreasing from 4.8-0 ka, with four, ~ 1000 yr cycles (figure 16). However, the rate of decrease was significantly higher at Greyling Lake. The difference in the rate of decrease may be related to the difference in dilution by glacial sediment at each site. The Greyling Lake core is from the central basin, which does not receive glacial sediment directly; sediment must pass through both Upper Greyling Lake and the southern sub-basin, or through a proglacial lake to the east and the northern sub-basin before it reaches the central sub-basin (figure 6b). Therefore, a

reduction in sediment input has a greater effect, both on increasing OM and decreasing sedimentation rate at Greyling Lake than at Hallet Lake.

Summary and conclusions

This study integrates the sediment records of two lakes with evidence of glacier activity to infer multiple aspects of Holocene climate in south-central Alaska, including a quantitative reconstruction of summer temperature for the past 2 kyr. This study is the first to quantitatively infer summer temperature from BSi, and the reconstruction is the longest quantitative temperature record with sub-decadal resolution produced for southern Alaska. From 4.8-0 ka, independently dated OM records varied synchronously, suggesting that the sediments at each lake record regional climate variability and that the age models for this part of each record are robust. High-resolution measurements of OM are related to the Aleutian Low Pressure Index (ALPI) ($r = 0.66$) and Gulkana and Valdez winter (DJFM) temperature ($r = 0.63$ and $r = 0.75$, respectively), indicating that OM may be a good measure of AL strength for the late Holocene. Since the strength of the AL controls winter precipitation in the region (Mock et al., 1998), the BSi and OM fluctuations provide information on winter precipitation and summer temperature, the two parameters most strongly linked to glacier health (Ohlendorf et al., 1997; Nesje et al., 2001) This allows for direct comparison to the record of glacial advances and ELA lowering during the LIA, which provide independent information about late Holocene climate in the study area. The paleotemperature record from Hallet Lake will be integrated into the ongoing NSF-ARCSS 2 kyr synthesis project (<http://www.arcus.org/synthesis2k/>).

OM and BSi were high, and sedimentation rates were low from 13-5 ka, indicating warmer summer temperature, reduced glacier extents, and a potentially strengthened AL during the time period. Beginning 4-5 ka, BSi and OM content at both lakes began a steady decrease to modern values, interpreted as the onset of neoglaciation in the region. During the past 2 kyr, reconstructed temperatures indicate periods of warmth from 100-500 AD, 1300-1500 AD, and after ~1900 AD. Periods of cool summer temperatures occurred from 500-1200 AD, and from 1600-1900 AD. The cooling from 500 to 600 AD, and subsequent cold period is consistent with records of a First Millennium AD glacial advance from the Chugach, Kenai, and St. Elias Mountains, and with other regional and hemispheric temperature reconstructions (Hu et al., 2001; Mann and Jones, 2003; Moberg et al., 2005; Wiles et al., 2007). The reconstruction suggests warming from ~700-1300 AD, but temperature did not reach its maximum until 1300-1500 AD. This peak warmth occurs later than the classically defined Medieval Warm Period, although the interval of warmth from 1300-1500 AD is observed in other regional and hemispheric temperature reconstructions (Mann and Jones, 2003; Moberg et al., 2005; Wiles et al., 2007). The Little Ice Age (LIA) is recognized in the BSi-inferred temperature record as the cool period from 1600-1900 AD. The most extensive neoglacial moraines in multiple cirques that feed both Hallet and Greyling Lakes were dated lichenometrically, and indicate that the glaciers stabilized during this time frame.

Following the maximum LIA cooling near the end of 19th century, summer temperature warmed rapidly, increasing by 3°C more than four times faster than the warming from 700-1300 AD. Average summer temperature during the period from 1976-2005 (12.4°C), which characterizes modern climate and the current AL regime, is nearly

2°C warmer than the average (10.6°C) over the past 2 kyr; the past 20 yr are the warmest of the last 2 kyr.

Fluctuations in OM over the past 2 kyr, interpreted to reflect AL strength and winter temperature, show similarities and differences with BSi-inferred summer temperature. OM was relatively high from 0-500 AD, 900-1300 AD, and after ~1900 AD. Low values occurred from 500-800 AD, and 1400-1900 AD.

The accumulation-area ratio (AAR) method was used to estimate former equilibrium-line altitudes (ELAs) for the maximum LIA and modern extents of 25 glaciers in the study area. The calculated ELA lowering during the LIA, relative to 1978, was 83 m. In contrast, the BSi-inferred temperature lowering of 1.5°C during the LIA is applied to a local environmental lapse rate ($-7^{\circ}\text{C km}^{-1}$) to suggest that ELA should have lowered by 210 m. This suggests a reduction in accumulation-season precipitation relative to 1978 and is consistent with the OM record, which implies reduced AL strength during the LIA.

References

- Anderson, L., Abbott, M.B., Finney, B.P., Edwards, M.E.** 2005: Palaeohydrology of the southwest Yukon territory, Canada, based on multiproxy analyses of lake sediment cores from a depth transect. *The Holocene* 15, 1172-83.
- Anderson, N.J.** 2000: Diatoms, temperature and climatic change. *European Journal of Phycology* 35, 307-14.
- Barclay, D.J., Wiles, G.C., Calkin, P.E.** 1999: A 1119-year tree-ring-width chronology from western Prince William Sound, southern Alaska. *The Holocene* 9, 79-84.
- Barclay, D.J., Wiles, G.C., Calkin, P.E.** 2002: An 850 year record of climate and fluctuations of the iceberg-calving Nellie Juan Glacier, south central Alaska, U. S. A.. *Annals of Glaciology* 36, 51-6.
- Beamish, R.J., Neville, C.E.M., Cass, A.J.** 1997: Production of Fraser River sockeye salmon (*oncorhynchus nerka*) in relation to decadal-scale changes in the climate and the ocean. *Canadian Journal of Fisheries and Aquatic Sciences* 54, 543-54.
- Bickerton, R.W., Matthews, J.A.** 1993: On the accuracy of lichenometric dates: an assessment based on the 'Little Ice Age' moraine sequence of Nigardsbreen, southern Norway. *The Holocene* 2, 227-37.
- Birks, H.J.B.** 1995: Quantitative palaeoenvironmental reconstructions. In Maddy, D., Brew, J., Editors, *Statistical Modelling of Quaternary Science Data. Technical Guide, Volume 5*, 161-254.
- Brázdil, R., Pfister, C., Wanner, H., Storch, H.V., Luterbacher, J.R.** 2005: Historical climatology in Europe—The state of the art. *Climatic Change* 70, 363-430.
- Calkin, P.E., Ellis, J.M.** 1980: A lichenometric dating curve and its application to Holocene glacier studies in the central Brooks Range, Alaska. *Arctic and Alpine Research* 12, 245-64.
- Calkin, P.E., Wiles, G.C., Barclay, D.J.** 2001: Holocene coastal glaciation of Alaska. *Quaternary Science Reviews* 20, 449-61.
- Cropper, J.P., Fritts, H.C.** 1981: Tree-ring width chronologies from the North American arctic. *Arctic and Alpine Research* 13, 245-60.
- Crusius, J., Anderson, R.F.** 1995: Evaluating the mobility of ^{137}Cs , $^{239+240}\text{Pu}$ and ^{210}Pb from their distributions in laminated lake sediments. *Journal of Paleolimnology* 13, 119-41.

- Daigle, T.A.** 2006: Late Holocene climate change at Goat Lake, Kenai Mountains, south-central Alaska. Master's thesis, Northern Arizona University, Flagstaff, AZ.
- Davi, N., Jacoby, G., Wiles, G.** 2003: Boreal temperature variability inferred from maximum latewood density and tree-ring width data, Wrangell Mountain region, Alaska. *Quaternary Research* 60, 252-62.
- Denton, G., Karlén, W.** 1977: Holocene glacial and tree-line variations in the White River Valley and Skolai Pass, Alaska and Yukon Territory. *Quaternary Research* 7, 63-111.
- Dyurgerov, M.** 2002: Glacier Mass Balance and Regime: Data of Measurements and Analysis. *INSTAAR occasional paper no. 55*, Institute of Arctic and Alpine Research, University of Colorado.
- Hamilton, T.D., Thorson, R.M.** 1983: The Cordilleran Ice Sheet in Alaska. In Porter, S.C., editor, *Late Quaternary Environments of the United States. Vol. 1, the Late Pleistocene*, University of Minnesota Press, University of Minnesota, Minneapolis, 38-52.
- Heegaard, E., Birks, H.J.B., Telford, R.J.** 2005: Relationships between calibrated ages and depth in stratigraphical sequences: An estimation procedure by mixed-effect regression. *The Holocene* 15, 612-8.
- Holdsworth, G., Fogarasi, S., Krouse, H.R.** 1991: Variation of the stable isotopes of water with altitude in the Saint Elias Mountains of Canada. *Journal of Geophysical Research* 96, 7483-94.
- Hu, F.S., Ito, E., Brubaker, L.B., Anderson, P.M.** 1998: Ostracode geochemical record of Holocene climatic change and implications for vegetational response in the northwestern Alaska Range. *Quaternary Research* 49, 86-95.
- Hu, F.S., Ito, E., Brown, T.A., Curry, B.B., Engstrom, D.R.** 2001: Pronounced climatic variations in Alaska during the last two millennia. *Proceedings of the National Academy of Sciences* 8, 1-5.
- Hu, F.S., Kaufman, D., Yoneji, S., Nelson, D., Shemesh, A., Huang, Y., Tian, J., Bond, G., Clegg, B., Brown, T.** 2003: Cyclic variation and solar forcing of Holocene climate in the Alaskan subarctic. *Science* 301, 1890-3.
- Hughes, M.K., Diaz, H.F.** 1994: Was there a 'Medieval Warm Period', and if so, where and when? *Climatic Change* 26, 109-42.
- Jones, P.D., Mann, M.E.** 2004: Climate over past millennia. *Review of Geophysics* 42, 1-42.
- Kaplan, M.R., Wolfe, A.P., Miller, G.H.** 2002: Holocene environmental variability in southern Greenland inferred from lake sediments. *Quaternary Research* 58, 149-59.

- Kathen, K.** 2006: Late Holocene climate fluctuations at Cascade Lake, northeastern Ahklun Mountains, southwestern Alaska. Master's thesis, Northern Arizona University, Flagstaff, AZ.
- Kaufman, D.S., Hu, F.S., Briner, J.P., Werner, A., Finney, B.P., Gregory-Eaves, I.** 2003: A ~33,000 year record of environmental change from Arolik Lake, Ahklun Mountains, Alaska, USA. *Journal of Paleolimnology* 30, 343-61.
- Kaufman D.S., Ager T.A., Anderson N.J., Anderson P.M., Andrews J.T., Bartlein P.T., Brubaker L.B., Coats L.L., Cwynar L.C., Duvall M.L., Dyke A.S., Edwards M.E., Eisner W.R., Gajewski K., Geirsdottir A., Hu F.S., Jennings A.E., Kaplan M.R., Kerwin M.W., Lozhkin A.V., MacDonald G.M., Miller G.H., Mock C.J., Oswald W.W., Otto-Bliesner B.L., Porinchu D.F., Ruhland K., Smol J.P., Steig E.J., Wolfe B.B.** 2004: Holocene thermal maximum in the western Arctic (0–180°W). *Quaternary Science Reviews* 23: 529-60.
- Kaufman, D.S., Manley, W.F.** 2004: Pleistocene Maximum and Late Wisconsinan glacier extents across Alaska, U.S.A. In Ehlers, J. and Gibbard, P.L. (editors), *Quaternary Glaciations – Extent and Chronology, Part II: North America*. Elsevier: 9-27.
- Ketterer, M.E., Hafer, K.M., Jones, V.J., Appleby, P.G.** 2004: Rapid dating of recent sediments in Loch Ness: Inductively coupled plasma mass spectrometric measurements of global fallout plutonium. *The Science of the Total Environment* 322, 221-9.
- Levy, L.B., Kaufman, D.S., Werner, A.** 2004: Holocene glacier fluctuations, Waskey Lake, northeastern Ahklun Mountains, southwestern Alaska. *The Holocene* 14, 185-93.
- Loso, M.G., Anderson, R.S., Anderson, S.P., Reimer, P.J.** 2006: A 1500-year record of temperature and glacial response inferred from varved Iceberg Lake, southcentral Alaska. *Quaternary Research* 66, 12-24.
- Mann, M.E., Jones, P.D.** 2003: Global surface temperatures over the past two millennia. *Geophysical Research Letters* 30, 1820-3.
- Mantua, N.J., Hare, S.R., Zhang, Y., Wallace, J.M., Francis, R.C.** 1997: A pacific interdecadal climate oscillation with impacts on salmon production. *Bulletin of the American Meteorological Society* 78, 1069-79.
- Meier, M.F., Post, A.S.** 1962: Recent variations in mass net budgets of glaciers in western North America. *IASH Publication* 58, 63–77.
- Minobe, S., Mantua, N.** 1999: Interdecadal modulation of interannual atmospheric and oceanic variability over the North Pacific. *Progress in Oceanography* 43, 163-92.

- Moberg, A., Sonechkin, D.M., Holmgren, K., Datsenko, N.M., Karlen, W., Lauritzen, S.E.** 2005: Highly variable Northern Hemisphere temperatures reconstructed from low- and high-resolution proxy data. *Nature* 433, 613-7.
- Mock, C.J., Bartlein, P.J., Anderson, P.M.** 1998: Atmospheric circulation patterns and spatial climatic variations in Beringia. *International Journal of Climatology* 18, 1085-104.
- Mortlock, R.A., Froelich, P.N.** 1989: A simple method for the rapid determination of biogenic opal in pelagic marine sediments. *Deep-Sea Research* 36, 1415-26.
- NCAR**, 2007: NP data provided by the Climate Analysis Section, NCAR, Boulder, USA, Trenberth and Hurrell (1994). Digital data at: <http://www.cgd.ucar.edu/cas/jhurrell/npindex.html>.
- NCDC**, 2007: National climatic data center data set for daily surface data, Gulklana, AK and Valdez, AK. Digital data at: <http://www.ncdc.noaa.gov/oa/ncdc.html>.
- Nesje, A., Dahl, S.O.** 2001: The Greenland 8200 cal. yr BP event detected in loss-on-ignition profiles in Norwegian lacustrine sediment sequences. *Journal of Quaternary Science* 16, 155-66.
- Nesje, A., Matthews, J.A., Dahl, S.O., Berrisford, M.S., Andersson, C.** 2001: Holocene glacier fluctuations of Flatebreen and winter-precipitation changes in the Jostedalbreen region, western Norway, based on glaciolacustrine sediment records. *The Holocene* 11, 267-80.
- Nesje, A., Olaf Dahl, S., Lie, Ø** 2004: Holocene millennial-scale summer temperature variability inferred from sediment parameters in a non-glacial mountain lake: Danntjørn, Jotunheimen, central southern Norway. *Quaternary Science Reviews* 23, 2183-205.
- Ohlendorf, C., Niessen, F., Weisser, H.** 1997: Glacial varve thickness and 127 years of instrumental climate data: A comparison. *Climatic Change* 36, 391-411.
- Osborn, T.J., Briffa, K.R.** 2006: The spatial extent of 20th-century warmth in the context of the past 1200 years. *Science* 311, 841-4.
- Osmaston, H.** 2005: Estimates of glacier equilibrium line altitudes by the area \times altitude, the area \times altitude balance ratio and the area \times altitude balance index methods and their validation. *Quaternary International* 138, 22-31.
- Overpeck, J., Hughen, K., Hardy, D., Bradley, R., Case, R., Douglas, M., Finney, B., Gajewski, K., Jacoby, G., Jennings, A.** 1997: Arctic environmental change of the last four centuries. *Science* 278, 1251-6.

- Papineau, J.M.** 2001: Wintertime temperature anomalies in Alaska correlated with ENSO and PDO. *International Journal of Climatology* 21, 1577-92.
- Rodionov, S.N., Overland, J.E., Bond, N.A.** 2005. The Aleutian low and winter climatic conditions in the Bering Sea. Part I: Classification. *Journal of Climate* 18, 160-77.
- Smith, S.V., Bradley, R.S., Abbott, M.B.** 2004: A 300 year record of environmental change from Lake Tuborg, Ellesmere Island, Nunavut, Canada. *Journal of Paleolimnology* 32, 137-48.
- Solomina, O., Calkin, P.E.** Lichenometry as applied to moraines in Alaska, USA, and Kamchatka, Russia. *Arctic, Antarctic, and Alpine Research* 35, 129-43.
- Stuiver, M., Reimer, P.J.** 1993: Extended ^{14}C data base and revised CALIB 3.0 ^{14}C age calibration program. *Radiocarbon* 35, 215-30.
- Telford, R.J., Heegaard, E., Birks, H.J.B.** 2004: The intercept is a poor estimate of a calibrated radiocarbon age. *The Holocene* 14, 296-8.
- Wake, C., Yalcin, K., Gundestrup, N.** 2003: The climate signal recorded in the oxygen isotope, accumulation, and major ion time-series from the eclipse ice core, Yukon Territory. *Annals of Glaciology* 35, 416-22.
- Wetzel, R.** 2001. *Limnology: Lake and river ecosystems*. Academic Press, San Diego, CA.
- Wiles, G.C., Barclay, D.J., Calkin, P.E.** 1999: Tree-ring-dated Little Ice Age histories of maritime glaciers from western Prince William Sound. *The Holocene* 9, 163–73.
- Wiles, G.C., Jacoby, G.C., Davi, N.K., McAllister, R.P.** 2002: Late Holocene glacier fluctuations in the Wrangell Mountains, Alaska. *Geologic Society of America Bulletin* 114, 896-908.
- Wiles, G.C., Barclay, D.J., Calkin, P.E., Lowell, T.V.** 2007: Century to millennial-scale temperature variations for the last two thousand years indicated from glacial geologic records of southern Alaska. *Global and Planetary Change* in press.
- Willemse, N.C., Törnqvist, T.E.** 1999: Holocene century-scale temperature variability from West Greenland lake records. *Geology* 27, 580-4.
- Wolfe, A.P., Miller, G.H., Olsen, C.A., Forman, S.L., Doran, P.T., Holmgren, S.U.** 2004: Geochronology of high latitude lake sediments. In Last, W.M. and Smol, J.P., editors, *Developments in paleoenvironmental research, Volume 8*, Springer, 19-52.

Table 1. Location, water depth and core length for lake cores recovered from Hallet and Greyling Lakes

Core	Lat (°N)	Long (°W)	Water depth (m)	Length (m)	Notes
<u>Hallet Lake</u>					
HT01	61.4934	146.2385	40.5	4.5	
HT01-A	61.4934	146.2385	40.5	0.3	Sub-sampled in field
HT01-B	61.4934	146.2385	40.5	0.4	
HT02	61.4955	146.2383	37.2	2.5	
HT02-A	61.4955	146.2383	37.2	0.2	
HT02-B	61.4955	146.2383	37.2	0.3	
HT03	61.4960	146.2397	38.5	4.2	
HT03-A	61.4960	146.2397	38.5	0.3	
HT03-B	61.4960	146.2397	38.5	0.2	
<u>Greyling Lake</u>					
GY02-A	61.3842	145.7364	30.2	0.3	
GY03	61.3835	145.7362	28.2	2.2	
GY03-A	61.3835	145.7362	28.2	0.4	
GY03-B	61.3835	145.7362	28.2	0.3	Sub-sampled in field
GY04	61.3824	145.7358	34.5	4.0	
GY04-A	61.3824	145.7358	34.5	0.4	
GY04-B	61.3824	145.7358	34.5	0.3	Sub-sampled in field
GY05	61.3875	145.7356	12.5	3.5	
GY05-A	61.3875	145.7356	12.5	0.3	Sub-sampled in field
GY05-B	61.3875	145.7356	12.5	0.4	

Note: Surface cores indicated by letter designation

Table 2. Radiocarbon ages and complimentary data

Lab ID [†]	Top depth (cm)	Bottom depth (cm)	Material type*	Fraction modern	±	D ¹⁴ C	±	¹⁴ C age (BP)	±	Cal age (BP) [§] (median probability)	2σ range ±
<u>Core HT01</u>											
29497	10	11	TPF	0.9765	0.0018	-23.5	1.8	190	15	175	140
29498	10	11	APF,TPF	0.9852	0.0015	-14.8	1.5	120	15	110	130
29499	81.5	82	TPF	0.904	0.0022	-96	2.2	810	20	715	40
33138	135	137	<120µm	0.8332	0.0021	-166.8	2.1	1465	25	1350	40
29500	177	178	TPF	0.7821	0.0013	-217.9	1.3	1975	15	1920	50
31584	177	178	<120µm	0.7805	0.0017	-219.5	1.7	1990	20	1940	50
29501	236	236.5	WS	0.7344	0.0012	-265.6	1.2	2480	15	2585	120
33139	299	301	<120µm	0.6555	0.0017	-344.5	1.7	3395	25	3645	60
33140	329	331	<120µm	0.6480	0.0034	-352.0	3.4	3485	45	3760	110
31585	363	365	<120µm	0.5813	0.0019	-418.7	1.9	4360	30	4920	90
33141	435	440	WS	0.4250	0.0008	-575.0	0.8	6875	15	7695	40
<u>Core HT03</u>											
29502	344	344.5	WS	0.5348	0.0009	-465.2	0.9	5025	15	5835	110
<u>Core GY03</u>											
31586	52	52.5	WS	0.8708	0.0014	-129.2	1.4	1110	15	1010	40
<u>Core GY05</u>											
31587	130	130	WS	0.6232	0.0010	-376.8	1.0	3800	15	4465	60
31588	149	149	WS	0.5758	0.0010	-424.2	1.0	4435	15	4190	70
33142	100	102	<120µm	0.6098	0.0021	-390.2	2.1	3975	30	5010	150
33143	190	192	<120µm	0.3641	0.0009	-635.9	0.9	8115	20	9030	40
33144	230	232	<120µm	0.2434	0.0010	-756.6	1.0	11350	35	13225	80
33145	260	262	<120µm	0.1392	0.0053	-860.8	5.3	15840	310	19085	500
33146	292	294	<120µm	0.2024	0.0158	-797.6	15.8	12830	630	15085	1660

* Material types

TPF Terrestrial plant fragments
 APF Aquatic plant fragments
 PF Unidentified plant fragments
 Ch Chitin
 WS Woody stems
 <120µm less than 120 µm size fraction (composed of chitin and detrital terrestrial and aquatic plant fragments)

[†] Analyses performed at the Keck Carbon Cycle AMS Facility at UC Irvine

[§] Calibrated using CALIB 5.0.2 (Stuiver and Reimer, 1993)

Table 3. Summary of lichen sizes on moraines in Hallet and Greyling Valleys

Lichen station (figure 3)	Latitude (°N)	Longitude (°W)	Maximum thallus diameter	# of lichens measured	Age (yr BP)*
<u>Hallet Valley</u>					
1	61.48031	146.23224	42	26	280
2	61.48063	146.23138	38	23	220
3	61.47974	146.28105	24	16	80
4	61.48000	146.24053	31	14	140
5	61.47714	146.22375	47	14	380
6	61.47687	146.22279	43	18	300
7	61.48023	146.21613	32	29	150
8	61.48097	146.21360	51	15	460
9	61.48182	146.21289	43	15	300
10	61.48207	146.21211	20	14	50
11	61.48505	146.20679	68	17	970
12	61.48679	146.24397	15	11	30
13	61.48947	146.24955	24	13	80
<u>Greyling Valley</u>					
1	61.37254	145.74860	25	20	80
2	61.37335	145.74854	46	21	360
3	61.37055	145.74991	8	9	0
4	61.36983	145.74675	33	20	160
5	61.37018	145.74470	18	13	40
6	61.36873	145.74618	40	18	250
7	61.36848	145.74363	32	20	150
8	61.37058	145.74206	32	19	150
9	61.37052	145.74143	17	18	40
10	61.37049	145.74030	44	27	320
11	61.36838	145.73821	17	19	40
12	61.36902	145.74020	34	21	170
13	61.37104	145.73427	38	22	220

*Based on the composite growth curve for the Wrangell–St. Elias Mountains presented by Solomina and Calkin (2003)

Table 4. Central Chugach Mountains cirque glacier equilibrium-line altitudes

Glacier (figure 5)	Location		1978 (AD)				Little Ice Age				Maximum	
	Lat (°N)	Long (°W)	Area (km ²)	Head altitude (m asl)	Toe altitude (m asl)	Maximum ELA (m asl)	Area (km ²)	Head altitude (m asl)	Toe altitude (m asl)	Minimum ELA (m asl)	ΔELA (m)	Area lost (%)
1	61.41	145.84	0.12	1710	1460	1590	0.24	1730	1310	1490	100	50
2	61.40	145.83	0.58	1750	1450	1550	1.09	1750	1360	1450	100	47
3	61.40	145.81	0.57	1670	1370	1450	0.63	1660	1330	1430	20	10
4	61.39	145.80	0.40	1700	1400	1470	0.61	1690	1300	1410	60	34
5	61.39	145.79	0.10	1610	1460	1530	0.18	1630	1390	1460	70	44
6	61.39	145.87	1.06	1780	1330	1540	1.48	1790	1190	1420	120	28
7	61.39	145.84	1.38	1820	1420	1560	2.16	1850	1250	1430	130	36
8	61.38	145.84	0.73	1790	1460	1560	1.09	1800	1350	1490	70	33
9	61.38	145.81	2.22	1750	1270	1420	3.88	1770	1110	1280	140	43
10	61.37	145.76	1.05	1730	1160	1470	1.21	1720	1090	1400	70	13
11	61.36	145.73	1.00	1570	1240	1410	1.40	1570	1090	1310	100	29
12	61.37	145.71	0.11	1610	1430	1490	0.31	1630	1330	1410	80	65
13	61.37	145.69	1.15	1760	1370	1490	1.63	1720	1360	1460	30	29
14	61.47	146.26	0.44	1700	1450	1550	1.39	1720	1150	1350	200	68
15	61.48	146.27	0.26	1900	1510	1650	0.33	1910	1460	1580	70	21
16	61.47	146.23	0.25	1640	1460	1520	0.32	1640	1370	1480	40	22
17	61.48	146.21	0.20	1690	1360	1480	0.37	1690	1270	1380	100	46
18	61.48	146.20	0.70	1880	1490	1630	1.14	1890	1200	1510	120	39
19	61.49	146.19	0.79	1730	1430	1530	0.97	1720	1330	1490	40	19
20	61.48	146.18	0.46	1860	1530	1640	0.53	1840	1480	1600	40	13
21	61.38	145.70	0.07	1600	1420	1470	0.13	1590	1380	1430	40	46
Average			0.65	1726	1403	1524	1.00	1729	1290	1441	83	35
Standard deviation			0.53	92	91	68	0.86	94	114	77	44	16

Note: The ELA estimates were maximized for the 1978 glaciers and minimized for the LIA glaciers to develop a maximum estimate of ΔELA

Table 5. Tephra geochemistry.

Tephra	Point	Weight-percent oxide (%) [§]									
		Na ₂ O	MgO	Al ₂ O ₃	SiO ₂	P ₂ O ₅ *	K ₂ O [†]	CaO	TiO ₂	MnO	FeO
GY03 39 cm	1	2.61	3.17	16.30	58.83	0.19	1.63	7.06	1.25	0.22	8.73
	2	1.93	2.45	16.26	63.24	0.26	1.95	5.55	1.11	0.19	7.05
	3	2.93	2.77	16.02	60.88	0.27	1.79	6.20	1.13	0.19	7.82
	4	2.92	1.83	15.61	63.14	0.34	2.16	4.87	1.30	0.19	7.64
	5	2.16	2.57	16.25	62.14	0.24	1.86	5.99	1.06	0.20	7.52
	6	2.33	3.04	16.76	59.93	0.25	1.62	6.51	1.19	0.21	8.16
	7	2.83	2.73	16.90	60.41	0.31	1.80	6.24	1.20	0.14	7.44
	8	2.10	2.72	16.44	60.72	0.23	1.87	6.23	1.23	0.23	8.24
	9	1.37	1.59	16.67	67.24	0.21	2.25	4.25	0.96	0.21	5.25
	10	2.04	2.79	16.59	61.45	0.19	1.78	6.14	1.15	0.17	7.69
	11	3.47	2.20	17.19	61.29	0.25	1.45	6.27	1.04	0.22	6.62
	12	2.21	2.61	17.05	61.80	0.27	1.74	5.75	1.14	0.14	7.29
	13	2.15	2.74	16.53	61.67	0.20	1.77	6.07	1.13	0.17	7.57
	Average	2.39	2.55	16.51	61.75	0.25	1.82	5.93	1.15	0.19	7.46
GY03 43 cm	1	0.89	1.55	14.84	72.64	0.30	3.40	2.33	0.95	0.03	3.07
	2	1.36	1.53	15.96	68.72	0.26	2.89	3.75	1.14	0.07	4.33
	3	3.66	0.18	19.19	67.07	0.19	1.83	4.84	0.83	0.00	2.21
	4	2.05	1.79	15.72	66.59	0.20	2.46	4.60	1.13	0.08	5.39
	5	1.65	2.00	16.00	66.51	0.18	2.36	4.44	1.19	0.07	5.59
	6	1.32	1.15	14.46	70.26	0.41	3.00	3.29	1.15	0.11	4.83
	7	2.67	2.44	16.49	64.46	0.14	1.91	5.41	1.03	0.08	5.37
	8	1.31	0.96	14.45	70.76	0.24	2.86	3.02	1.39	0.05	4.97
	9	2.48	1.53	18.86	64.18	0.17	1.62	5.88	0.86	0.07	4.36
	10	3.73	1.76	21.57	60.15	0.04	1.14	7.76	0.61	0.08	3.17
	Average	2.11	1.49	16.75	67.13	0.21	2.35	4.53	1.03	0.06	4.33
GY05 18 cm	1	1.92	3.29	16.51	59.47	0.20	1.48	6.94	1.19	0.20	8.80
	2	2.03	2.59	16.48	62.10	0.23	1.94	6.11	1.05	0.14	7.33
	3	1.21	3.53	15.18	61.42	0.27	1.83	6.63	1.09	0.27	8.57
	4	2.17	2.65	16.01	61.00	0.30	2.00	6.65	1.29	0.20	7.75
	5	2.01	2.31	16.22	63.62	0.29	1.97	5.47	1.15	0.19	6.77
	6	2.20	2.72	16.08	61.36	0.24	1.83	6.40	1.15	0.20	7.83
	7	2.44	2.91	16.28	60.65	0.27	1.82	6.46	1.14	0.20	7.84
	8	1.18	2.86	16.10	61.63	0.26	1.86	6.81	1.08	0.21	8.02
	9	1.73	2.60	16.12	62.28	0.22	1.89	6.22	1.12	0.19	7.62
	10	1.72	2.91	16.72	60.47	0.25	1.77	6.89	1.23	0.18	7.85
	Average	1.86	2.84	16.17	61.40	0.25	1.84	6.46	1.15	0.20	7.84

Table 5 (continued). Tephra geochemistry.

Tephra	Point	Weight-percent oxide (%) [§]									
		Na ₂ O	MgO	Al ₂ O ₃	SiO ₂	P ₂ O ₅ *	K ₂ O [†]	CaO	TiO ₂	MnO	FeO
GY05 67 cm	1	1.02	0.52	15.58	75.56	nd	2.35	2.60	0.36	0.06	1.94
	2	0.92	0.41	14.30	78.01	0.08	2.43	1.82	0.32	0.09	1.63
	3	1.05	0.41	14.32	77.61	nd	2.58	1.93	0.35	0.05	1.71
	4	2.41	14.59	12.31	43.60	nd	0.47	12.40	1.90	0.18	12.12
	5	1.14	0.32	14.07	78.35	nd	2.59	1.73	0.28	0.04	1.49
	6	2.06	0.35	23.96	65.65	nd	2.72	2.47	0.37	0.01	2.38
	7	0.80	0.32	14.07	78.82	nd	2.52	1.70	0.27	0.03	1.45
	8	0.42	0.23	13.30	81.38	0.03	1.46	1.08	0.41	0.04	1.64
	9	0.28	15.45	0.70	52.91	0.17	0.02	21.21	0.25	0.69	8.32
	10	0.87	15.51	3.34	50.94	0.03	0.15	18.89	0.81	0.53	8.92
	11	2.22	14.48	11.40	44.68	0.03	0.40	11.73	1.57	0.47	13.03
	12	0.94	0.40	14.55	77.82	nd	2.39	1.90	0.32	0.07	1.60
	13	1.08	0.41	14.59	77.37	nd	2.23	1.96	0.34	0.08	1.93
	14	0.79	0.41	14.33	78.43	nd	2.26	1.78	0.34	0.05	1.59
	15	0.55	0.34	14.14	79.70	nd	1.96	1.60	0.25	0.05	1.43
	Average Pop. 1	0.98	0.37	15.20	77.15	0.06	2.32	1.87	0.33	0.05	1.71
	Average Pop. 2	1.45	15.01	6.94	48.03	0.08	0.26	16.06	1.13	0.47	10.60
	Total Average	1.10	4.28	13.00	69.39	0.07	1.77	5.65	0.54	0.16	4.08
HT01 180 cm	1	0.83	0.36	14.44	79.33	0.02	1.63	1.56	0.32	0.07	1.43
	2	1.10	0.38	14.21	78.30	0.03	2.06	1.74	0.36	0.05	1.76
	3	0.80	0.43	14.63	78.26	nd	1.91	1.92	0.35	0.05	1.66
	4	0.58	0.31	13.93	79.74	0.03	1.97	1.57	0.26	0.11	1.49
	5	1.21	7.69	12.09	62.30	nd	0.99	7.22	1.47	0.22	6.82
	6	0.68	0.37	14.09	79.44	0.03	1.68	1.76	0.31	0.05	1.59
	7	0.91	0.37	13.96	79.08	nd	2.05	1.68	0.31	0.07	1.57
	8	0.89	0.41	14.47	78.14	nd	2.08	1.96	0.34	0.08	1.62
	9	0.90	0.32	14.01	79.19	nd	2.21	1.62	0.27	0.07	1.40
	10	0.34	0.33	14.01	80.27	0.02	1.60	1.59	0.26	0.04	1.54
	Average	0.82	1.10	13.99	77.40	0.03	1.82	2.26	0.43	0.08	2.09

*The 2 σ detection limit is 0.01 wt. %oxide

†The 2 σ detection limit is 0.005 wt. %oxide

§Normalized to 100%

nd = not-detectable

Table 6. $^{239+240}\text{Pu}$, ^{137}Cs , and ^{210}Pb activities for core HT01-B from Hallet Lake and core GY02-A from Greyling Lake

Depth (cm)	$^{239+240}\text{Pu}$ activity		^{137}Cs activity		Unsupported ^{210}Pb activity	
	(Bq/g)	±	(Bq/g)	±	(Bq/g)	±
Core HT01-B						
0.25	320	30	0.017	0.003	0.233	0.017
0.75	420	30	0.031	0.002	0.125	0.013
1.25	580	20	0.095	0.003	0.087	0.012
1.75	520	20	0.117	0.003	0.035	0.014
2.25	1230	50	0.095	0.003	0.018	0.013
2.75	2170	20	0.052	0.003	0.012	0.014
3.25	2350	70	0.011	0.002	0.023	0.013
3.75	1850	20				
4.25	850	20	0.002	0.002	0.037	0.012
4.75	200	20				
5.25	<100		0.003	0.002	0.027	0.012
5.75	<100					
6.25	<100		0.000	0.002	0.027	0.010
6.75	<100					
7.25	<100					
7.75	<100					
8.25	<100		0.003	0.002	0.000	0.011
8.75	<100					
9.25	<100					
9.75	<100					
Core GY02-A						
0.25	410	20	0.027	0.002	0.574	0.016
0.75	340	40	0.034	0.002	0.449	0.015
1.25	860	20	0.051	0.002	0.370	0.014
1.75	1880	20	0.095	0.002	0.289	0.014
2.25	1790	40	0.111	0.002	0.099	0.010
2.75	1130	60	0.066	0.002	0.040	0.012
3.25	2050	50	0.093	0.002	0.066	0.013
4.25	4020	50	0.175	0.003	0.104	0.013
5.25	2380	30	0.097	0.002	0.091	0.012
6.25	4260	20				
7.25	<100		0.006	0.001	0.047	0.014
8.25	<100					
10.25	<100		0.000	0.001	0.033	0.011
13.25	<100		0.001	0.001	0.029	0.012
17.25			-0.001	0.001	0.014	0.010
19.75			0.000	0.001	0.034	0.012

Table 7. Correlations between biogenic silica flux and organic-matter content and meteorological and North Pacific climate indices

Correlated Parameter	Biogenic silica flux*			Organic-matter**			Source ^{††}
	n	R	p-value	n	R	p-value	
Valdez T _{annual}	22	0.75	6x10 ⁻⁵	11	0.67	0.03	1
Valdez T _{JJA}	26	0.87	5x10 ⁻⁷	12	0.47	0.13	1
Valdez T _{DJFM}	22	0.63	0.002	11	0.75	0.008	1
Valdez P _{annual}	26	0.31	0.12	10	0.46	0.18	1
Valdez P _{JJA}	23	0.07	0.75	10	0.40	0.25	1
Valdez P _{DJFM}	20	0.18	0.45	9	0.71	0.03	1
Gulkana T _{annual}	18	0.52	0.03	8	0.52	0.2	1
Gulkana T _{JJA}	18	0.32	0.2	8	0.14	0.74	1
Gulkana T _{DJFM}	18	0.56	0.02	8	0.63	0.08	1
ALPI [†]	32	0.55	0.001	16	0.66	0.005	2
NPI _{DJFM} [§]	32	0.45	0.009	16	-0.76	0.0007	3

*All parameters correlated with BSi flux are 5-yr averages

**All parameters correlated with OM are 7-yr averages

[†]Aleutian Low Pressure Index

[§]North Pacific Index (Dec-Mar)

^{††}(1)NCDC, 2007; (2) Beamish et al., 1997; NCAR, 2007

Table 8. Biogenic silica flux and organic-matter data from surface core HT01 with selected instrumental datasets.

Biogenic silica flux			Organic Matter				
Year AD*	BSi flux (mg cm ⁻² yr ⁻¹)	Valdez T _{JJA} (°C) (5-yr mean)	Year AD*	OM (%)	ALPI [†] (7-year mean)	Valdez T _{DJFM} (°C) (7-yr mean)	Gulkana T _{DJFM} (°C) (7-yr mean)
2004	2.33	13.2	1999	3.4	1.9	-2.9	-10.3
2001	2.33	12.7	1993	3.9	0.3	-3.2	-10.4
1998	2.02	12.9	1986	3.6	2.0	-2.4	-9.0
1994	1.52	12.7	1980	3.9	2.1	-3.1	-10.2
1991	1.27	12.5	1973	3.2	-1.0	n.d.	-12.5
1988	1.25	12.1	1966	3.4	-0.5	-5.1	-12.3
1985	1.30	11.8	1960	3.1	0.3	-5.2	-11.1
1981	1.30	11.9	1953	3.1	-1.9	-7.0	-12.3
1978	1.29	12.0	1946	3.3	0.0	-6.3	
1976	1.23	12.1	1940	3.2	1.2	-4.8	
1967	1.16	11.9	1932	3.5	0.0	-4.8	
1965	1.11	11.8	1927	3.3	0.9	n.d.	
1961	1.18	11.6	1920	3.2	-0.8	-6.8	
1958	1.00	11.4	1913	3.1	-1.5		
1955	1.09	11.1	1907	2.7	-1.4		
1951	0.93	10.8	1900	3.0	-0.8		
1948	0.97	10.9					
1945	1.03	10.9					
1942	1.14	11.3					
1938	1.36	11.7					
1936	1.67	12.1					
1932	1.15	10.1					
1928	1.01	10.1					
1924	1.14	10.9					
1922	0.97	10.9					
1918	1.04	10.5					

*Year AD (middle of the 5- or 7-year mean) determined for Bsi flux and OM using the sedimentation rate indicated by the ²³⁹⁺²⁴⁰Pu peak in core HT01-B

[†]Beamish et al. (1997)

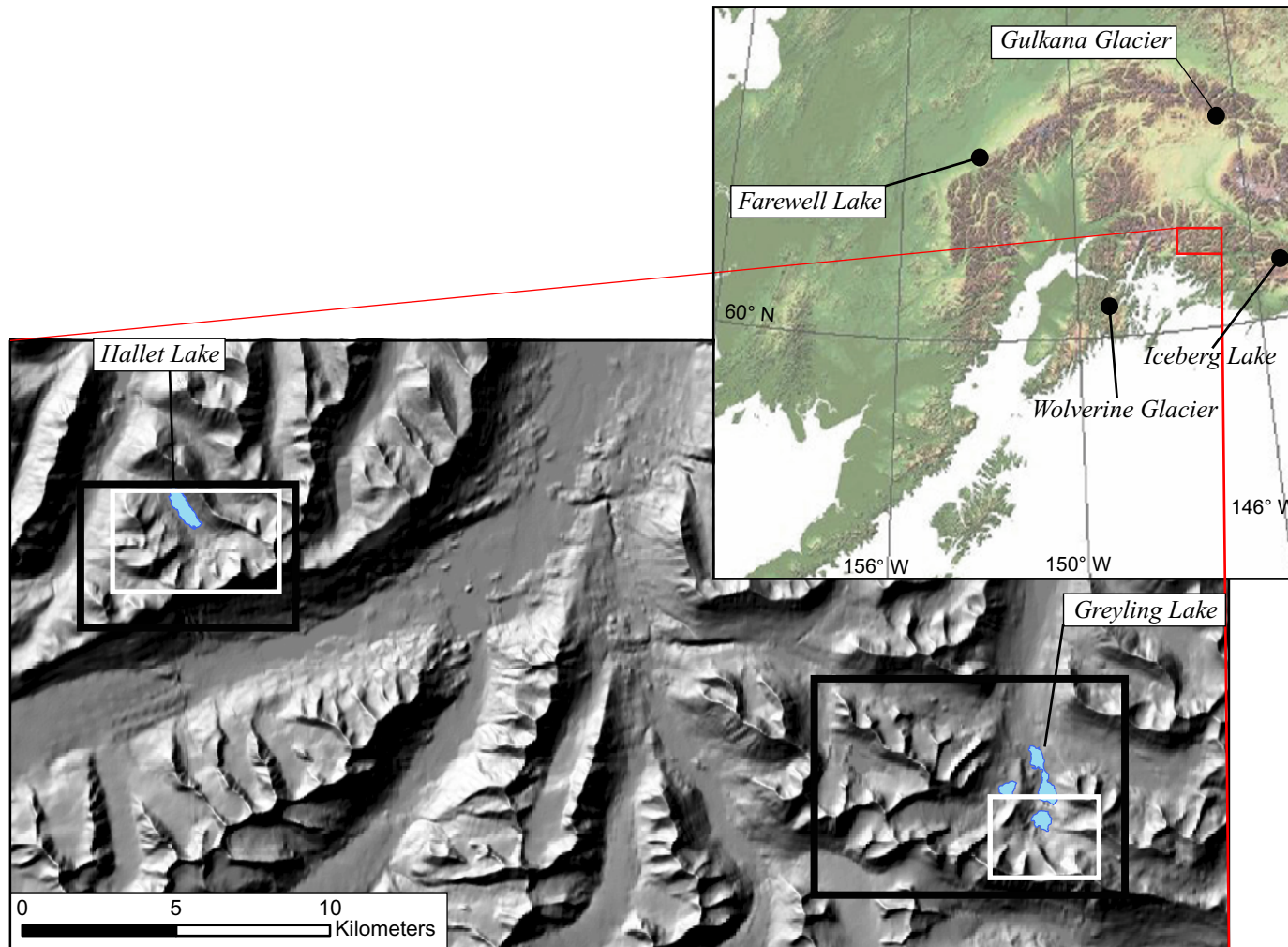


Figure 1. Study area on the north side of the Chugach Range, south-central Alaska. Locations of other high-resolution records of climate derived from lake sediment for southern Alaska (Farewell Lake: Hu et al., 2001; Iceberg Lake: Loso et al., 2006), and of long-term glacier mass-balance data (Wolverine and Gulkana Glaciers; Dwyergerov, 2002) are also shown. Map areas shown for figure 3 (white rectangles) and figure 5 (black rectangles).

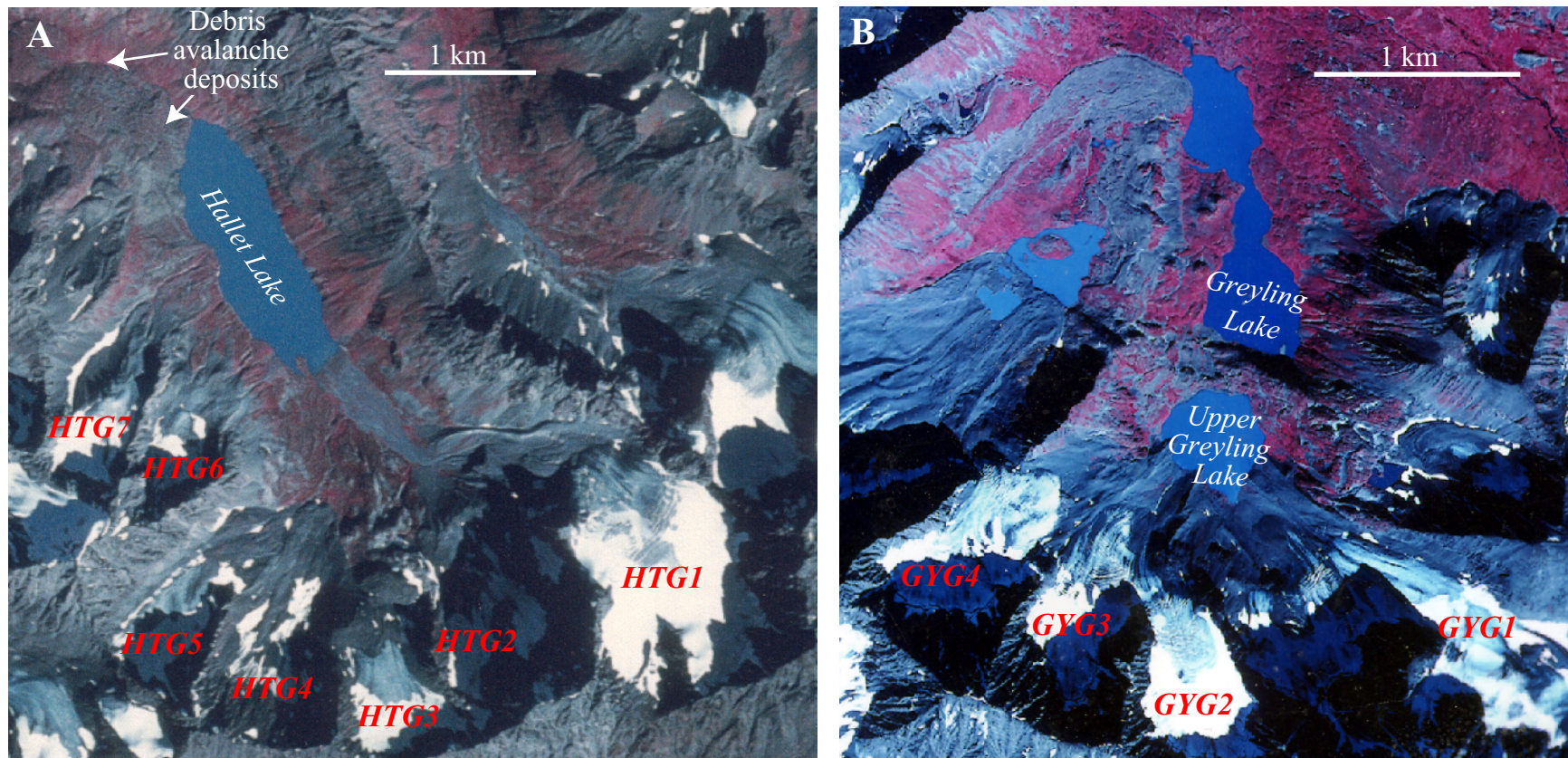


Figure 2. 1978 color-infrared aerial photographs of the study areas near (A) Hallet Lake and (B) Greyling Lake. HTG1-7 and GYG 1-4 denote the glaciers in the watersheds of Hallet and Greyling Lakes respectively. Hallet Lake is dammed by the debris avalanche deposits that originated from the currently unoccupied cirques in the northwest corner of the study area.

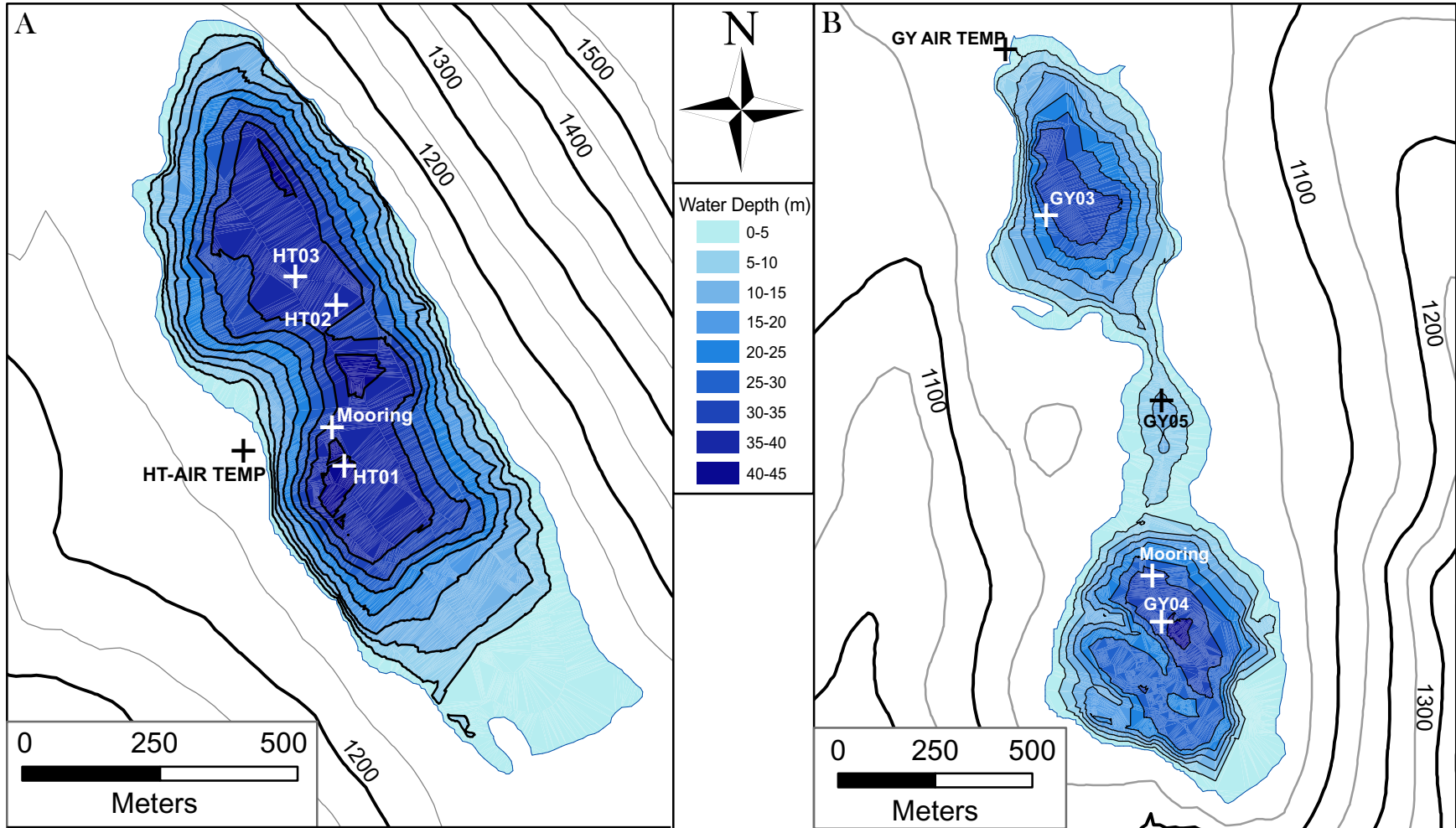


Figure 3. Bathymetric maps of (A) Hallet Lake and (B) Greyling Lake. Core sites, instrument moorings, and location of temperature sensors are indicated by black crosses. Topographic contours in m asl.

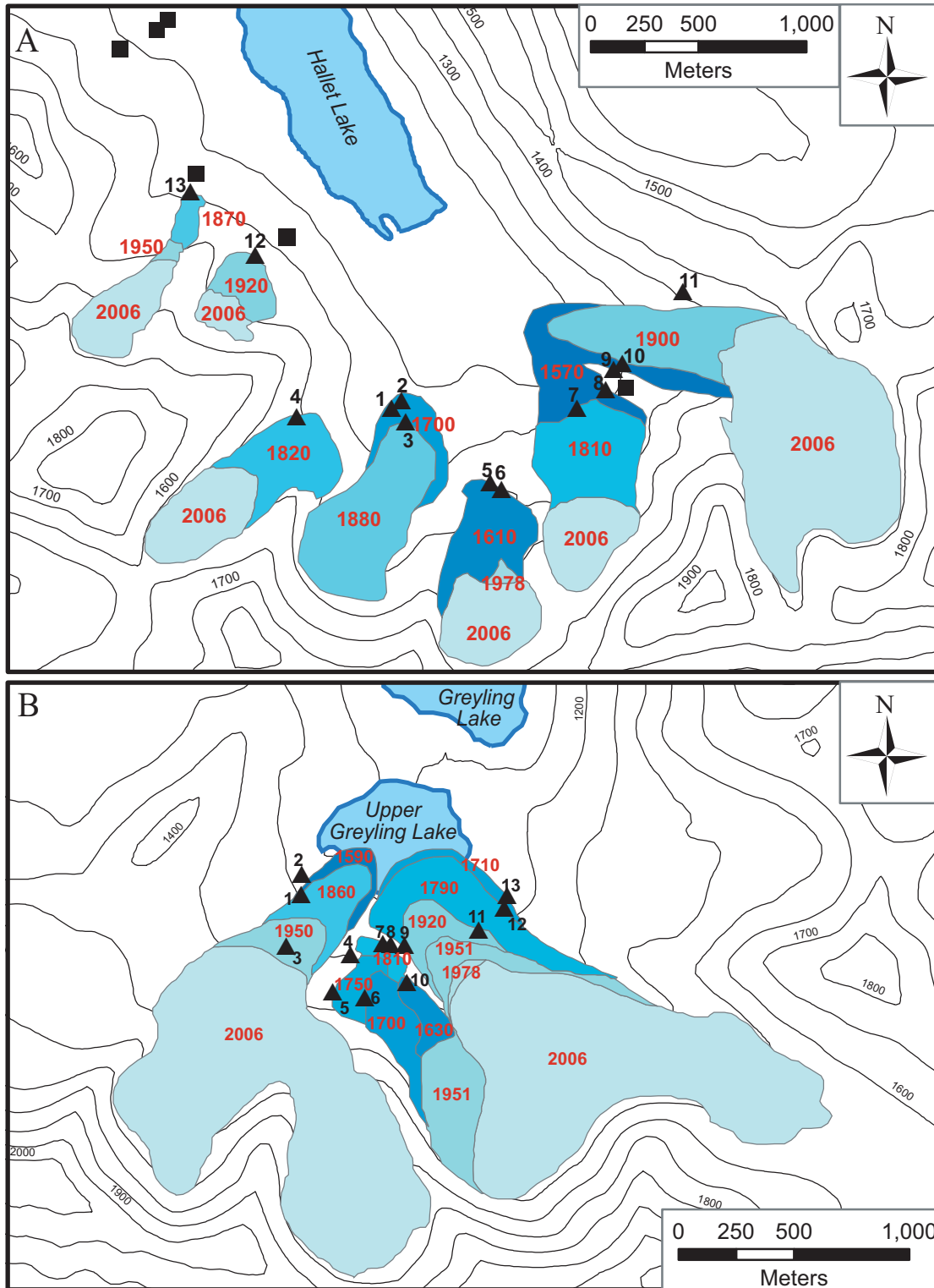
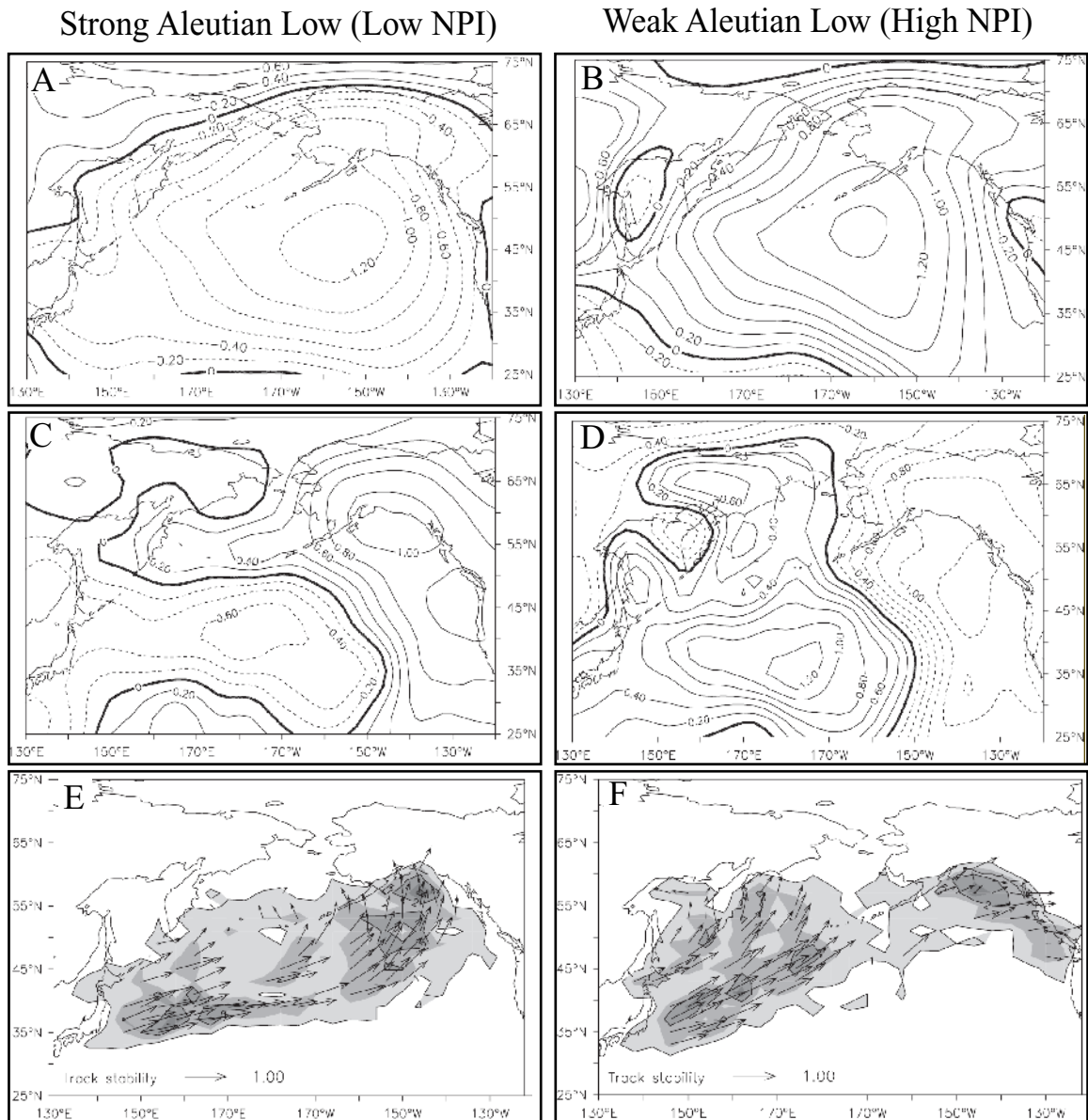


Figure 4. Glacier extents over the past 500 years in (A) Hallett and (B) Greyling valleys, red numbers = yr AD. Evidence for ice extents based on: 2006 = field mapping; 1978 = 1:63,360-scale aerial photographs; 1950 = USGS topographic maps; all others = glacial evidence and lichenometric ages. Lichen stations indicated by black triangles (Table 3). Black squares indicate landforms with lichens older than the LIA. Contour intervals in m asl. Map area shown in figure 1.



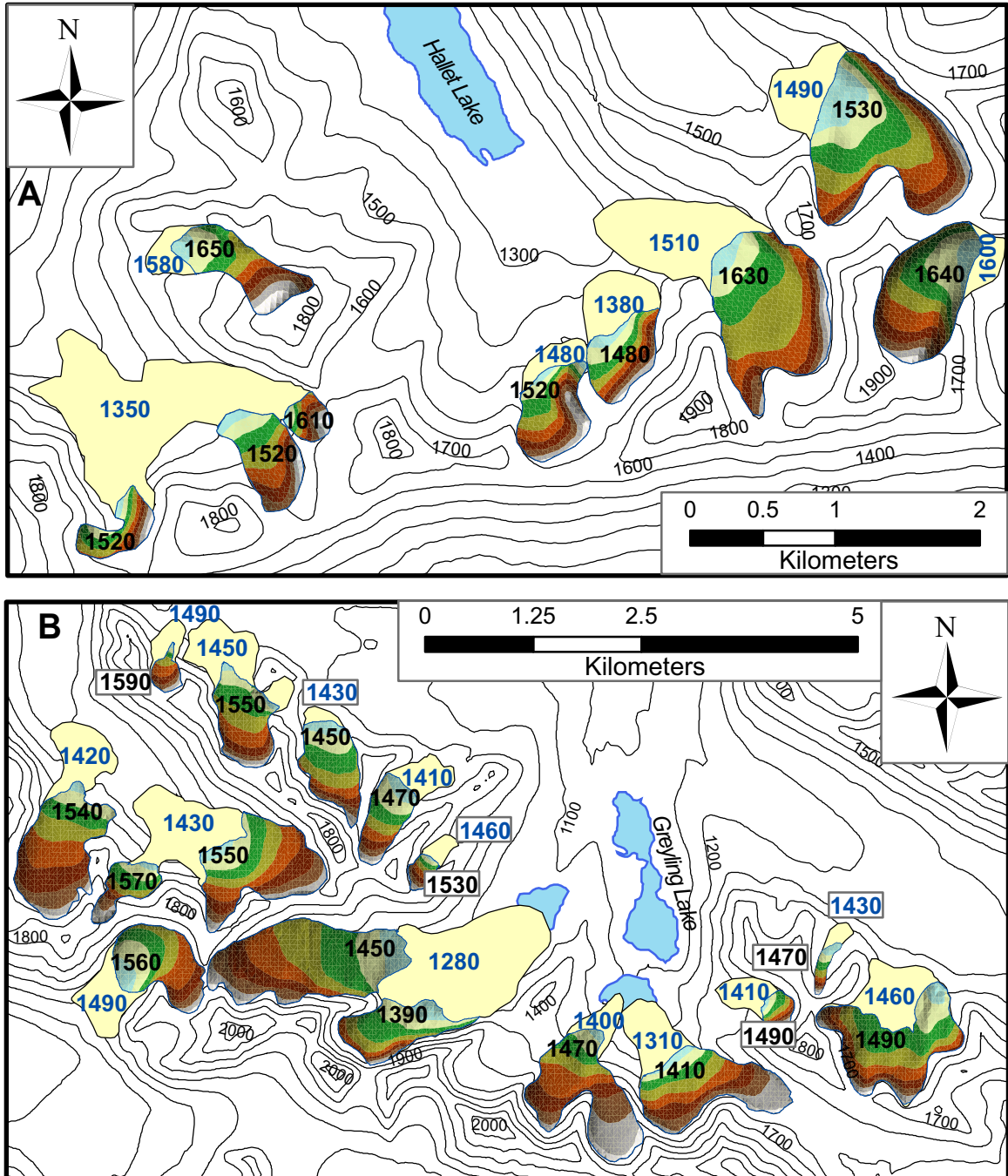


Figure 6. Map of modern (1978) and LIA glacier extents near (A) Hallet Lake and (B) Greyling Lake. Modern glacier extents shown with colored elevation bands, LIA extent in yellow. Blue numbers are calculated LIA ELA, black numbers are calculated modern ELA (m asl). Countour interval = 100 m. Map areas shown in figure 1.

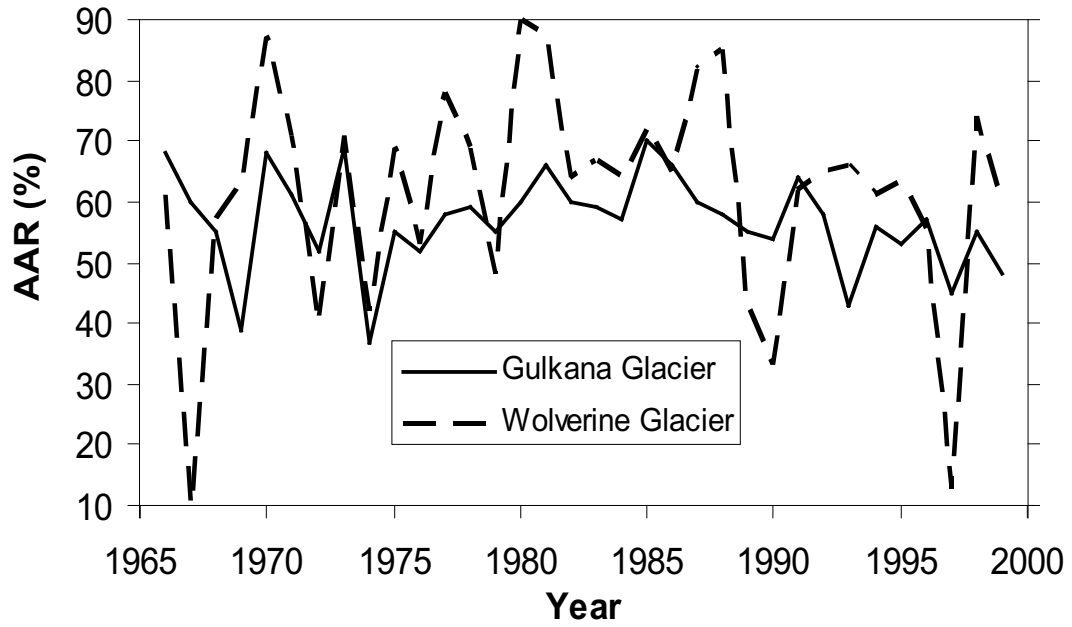


Figure 7. Accumulation area ratios (AAR) derived from mass-balance measurements at Gulkana and Wolverine Glaciers. Data from Dyurgerov (2002).

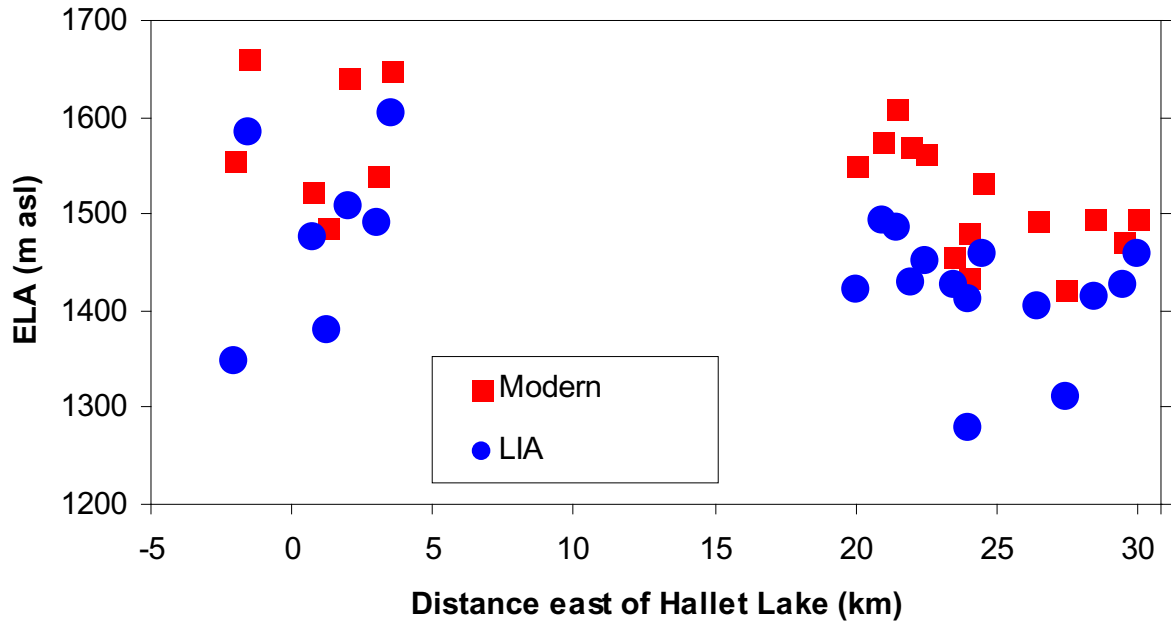


Figure 8. Equilibrium-line altitudes (ELA) estimated for 21 glaciers near Hallet and Greyling Lakes, calculated for both LIA and modern (1978) glaciers. ELAs rise to the west.

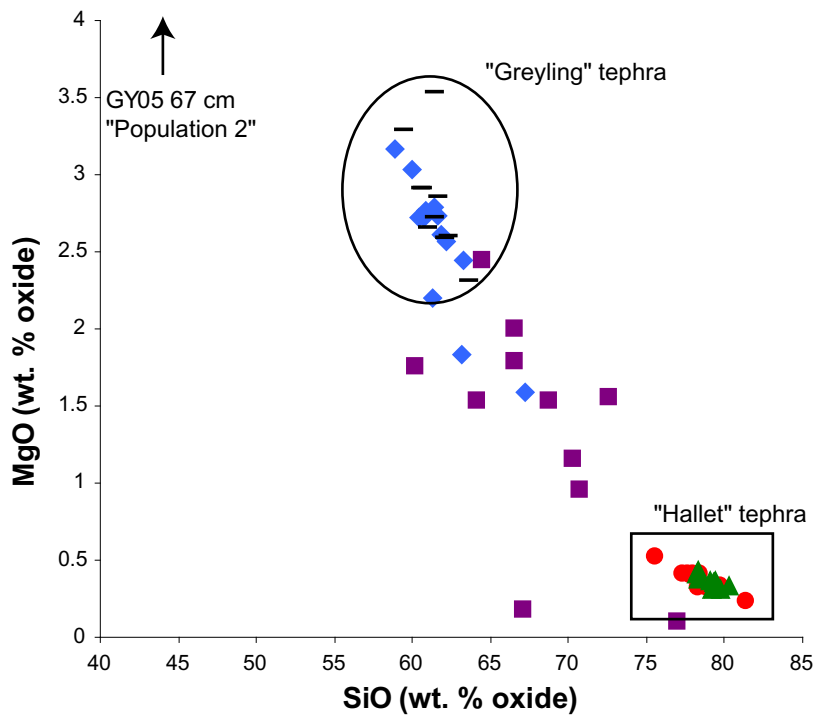
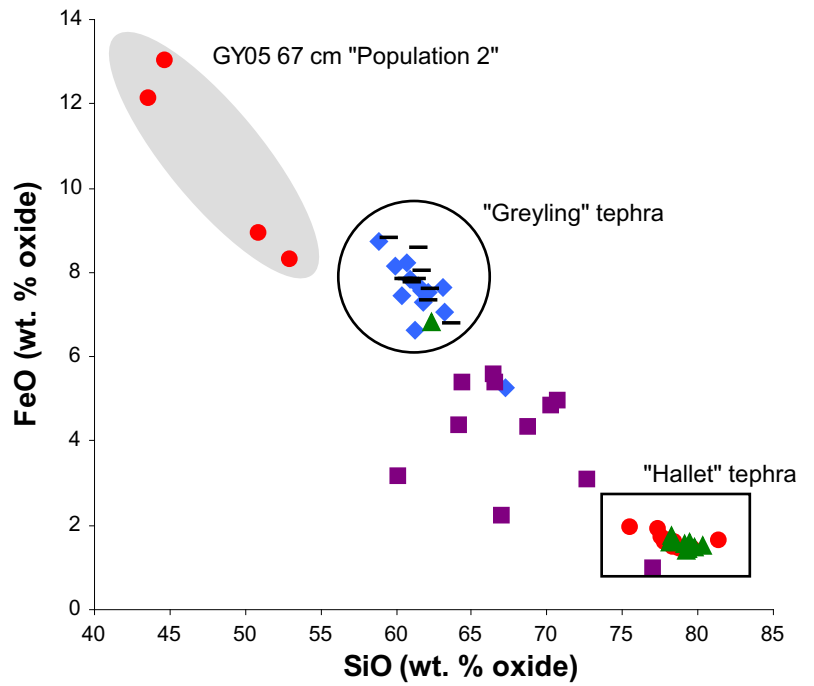


Figure 9. FeO and MgO plotted against SiO for the five analyzed tephtras. The populations of the "Greyling" and "Hallet" tephtras are shown by open ellipses and rectangles, respectively. The second population from tephtra GY05 67 cm is indicated by the gray ellipse.

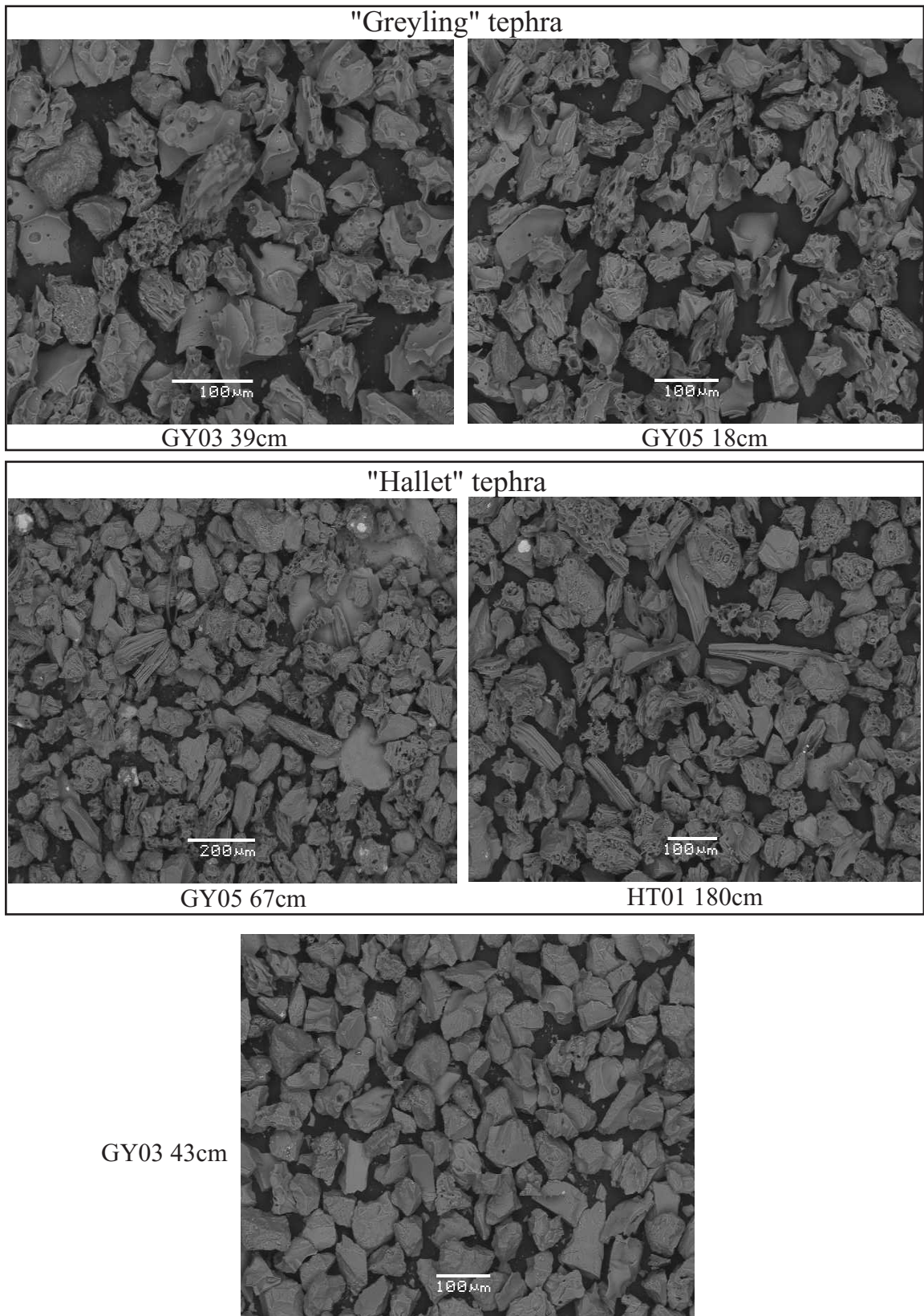


Figure 10. Examples of shard morphology from the five tephra deposits.

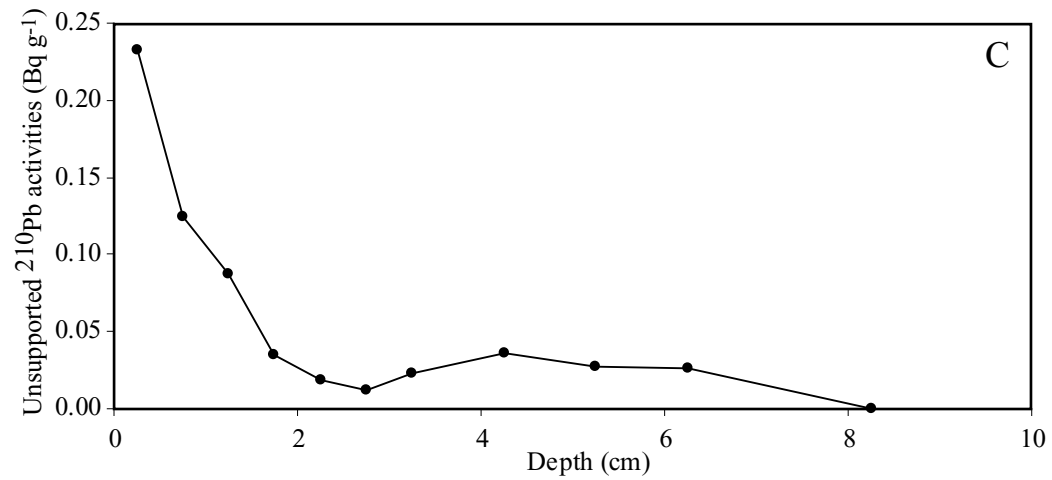
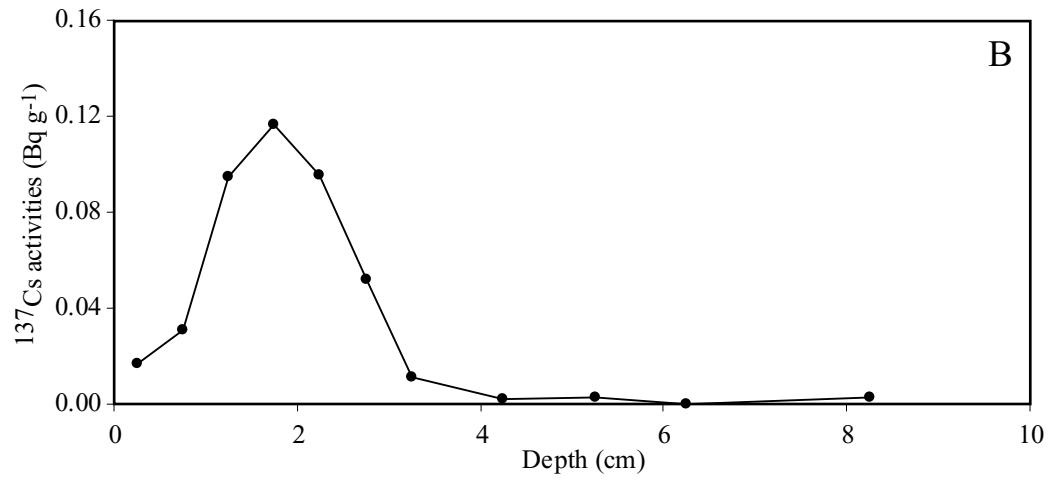
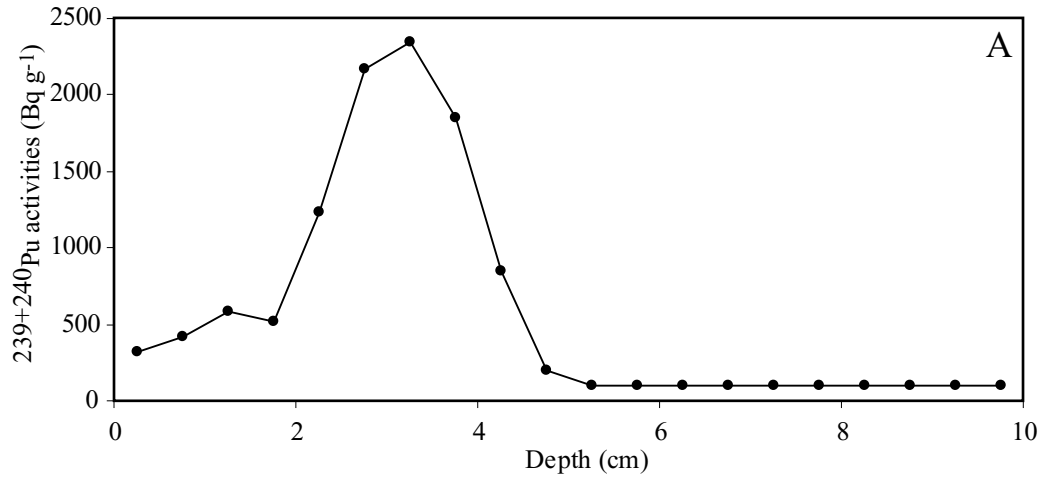


Figure 11. The (A) $^{239+240}\text{Pu}$ profile, (B) ^{137}Cs profile, and (C) $^{210}\text{Pb}_{\text{ex}}$ profile from short core HT01-B.

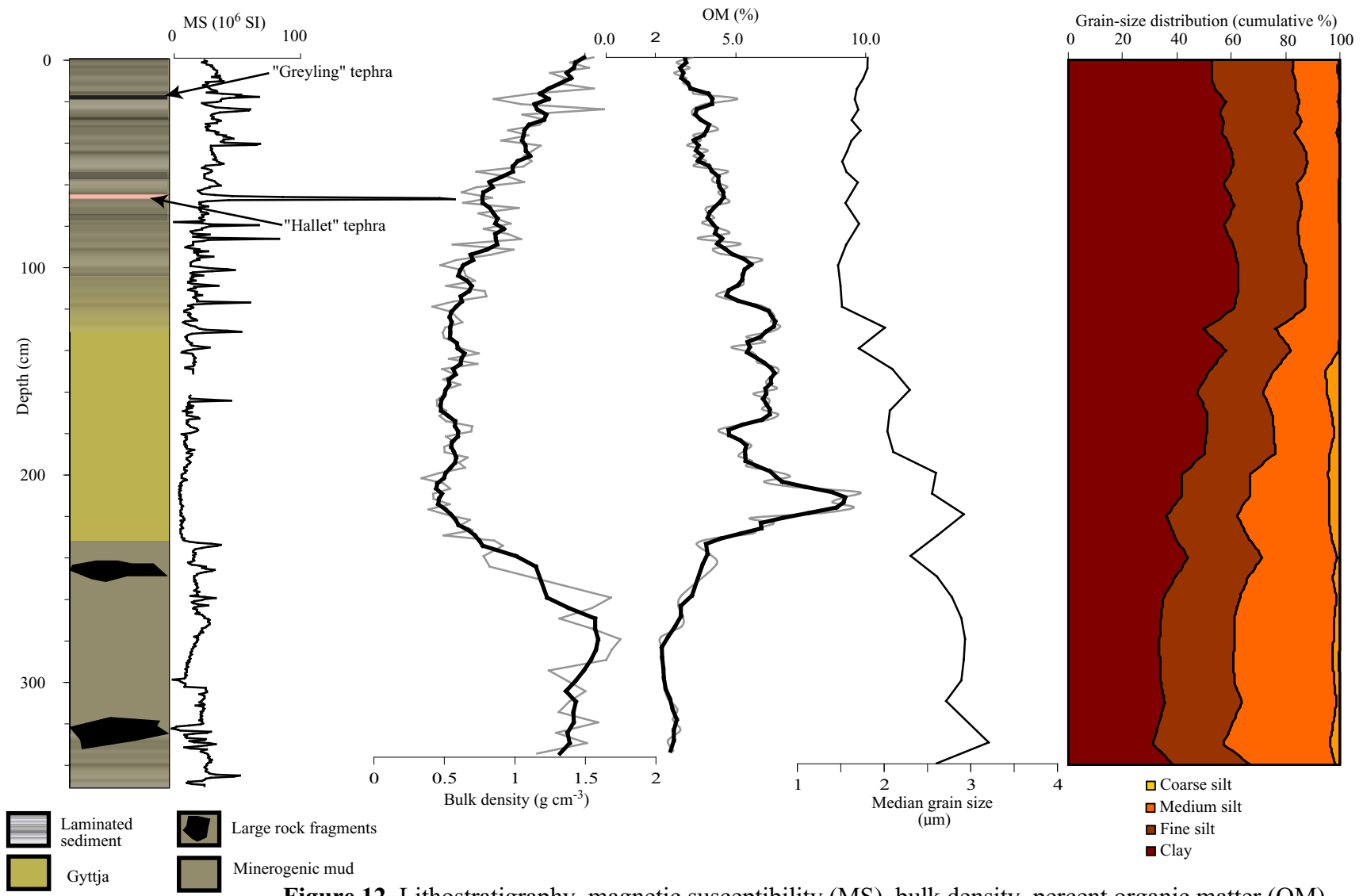


Figure 12. Lithostratigraphy, magnetic susceptibility (MS), bulk density, percent organic matter (OM) median grain size, and grain-size distribution for core GY05 from Greyling Lake.

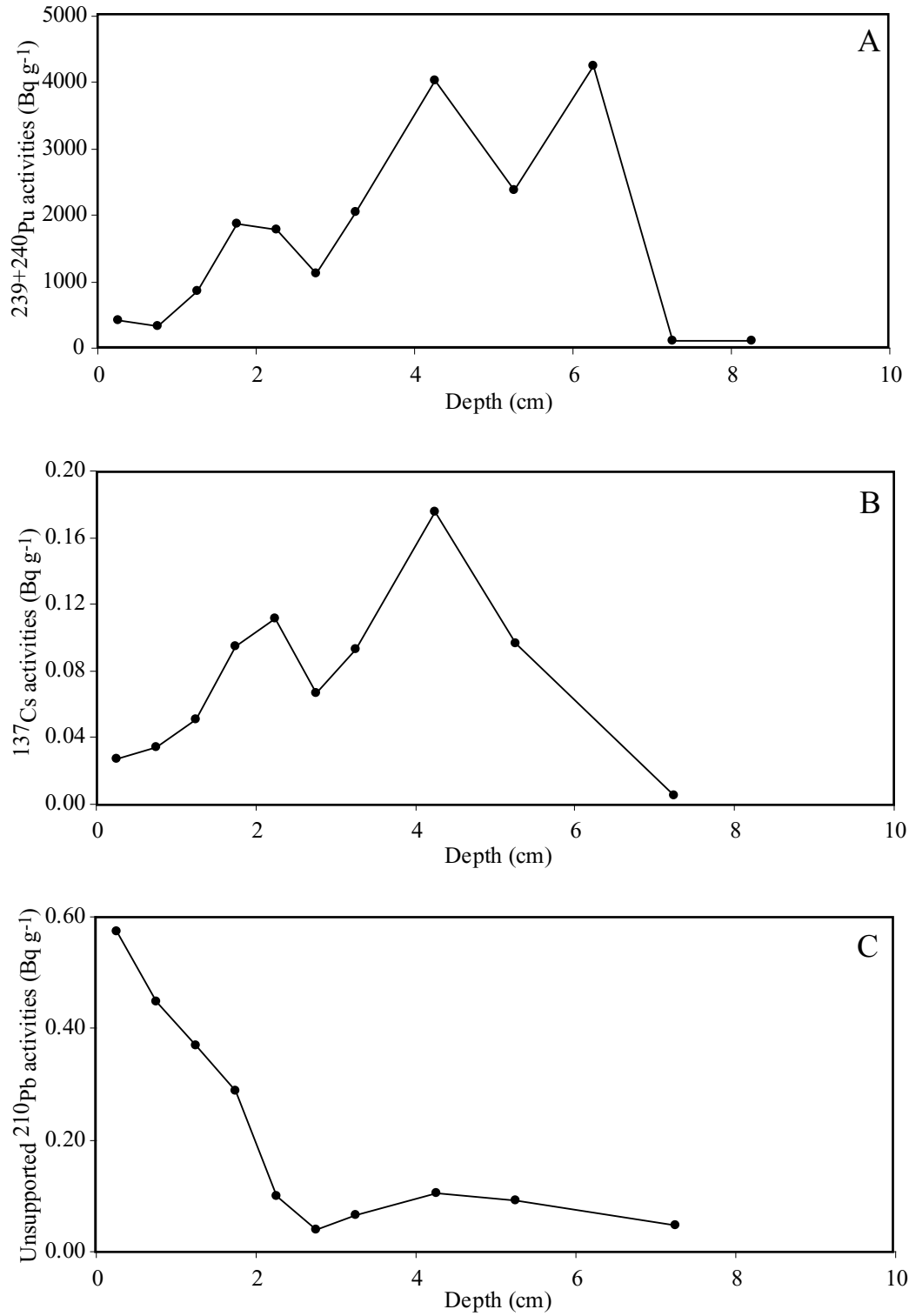


Figure 13. The (A) $^{239+240}\text{Pu}$ profile, (B) ^{137}Cs profile, and (C) $^{210}\text{Pb}_{\text{ex}}$ profile from short core GY02-A.

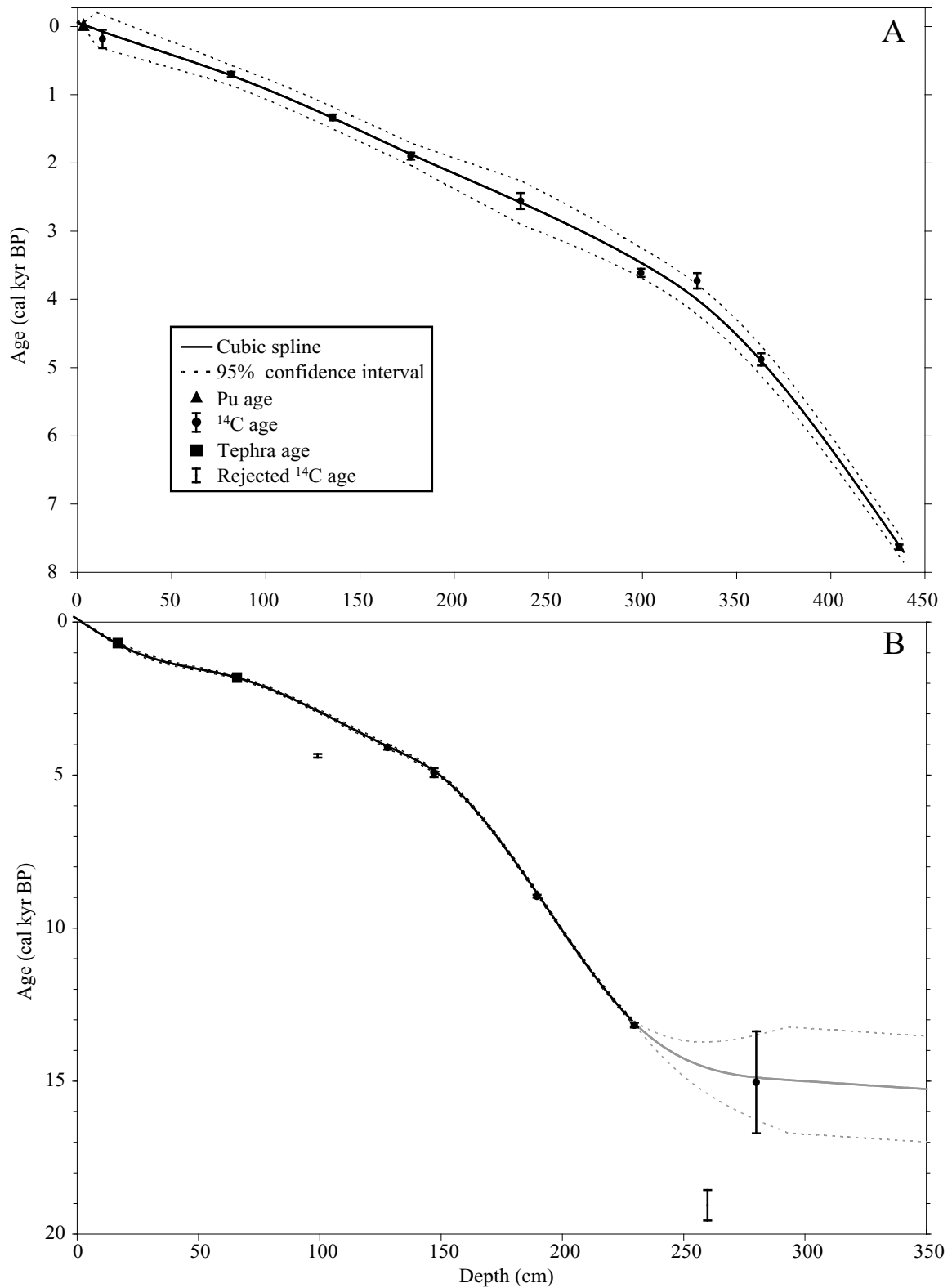


Figure 14. Age-depth models for cores (A) HT01, and (B) GY05. The cubic spline and confidence intervals were developed following Heegaard et al. (2005). Gray lines indicate poorly constrained age model and associated 95% confidence intervals. Error bars show the 2-sigma ranges for the calibrated ¹⁴C ages.

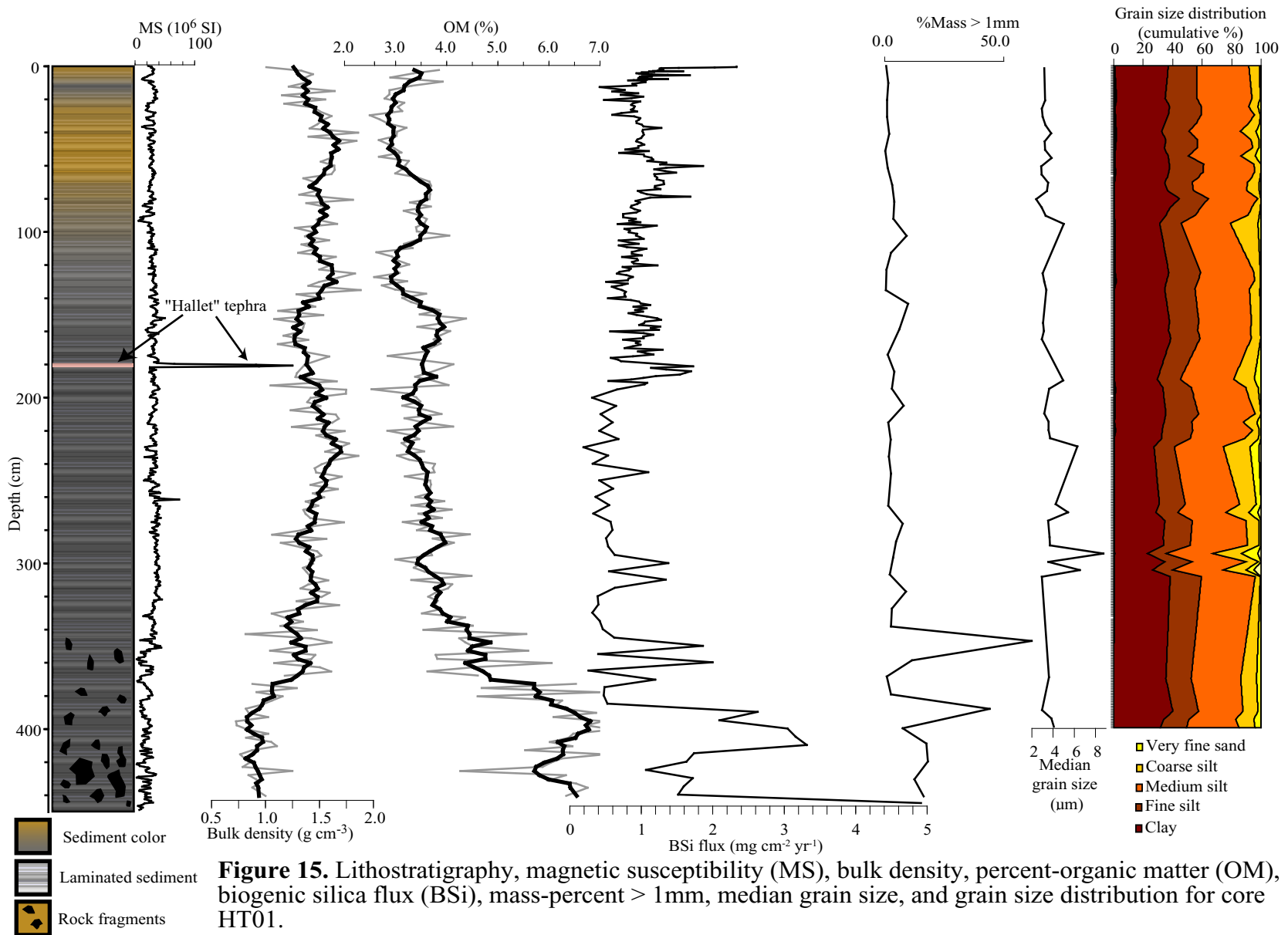


Figure 15. Lithostratigraphy, magnetic susceptibility (MS), bulk density, percent-organic matter (OM), biogenic silica flux (BSi), mass-percent > 1mm, median grain size, and grain size distribution for core HT01.

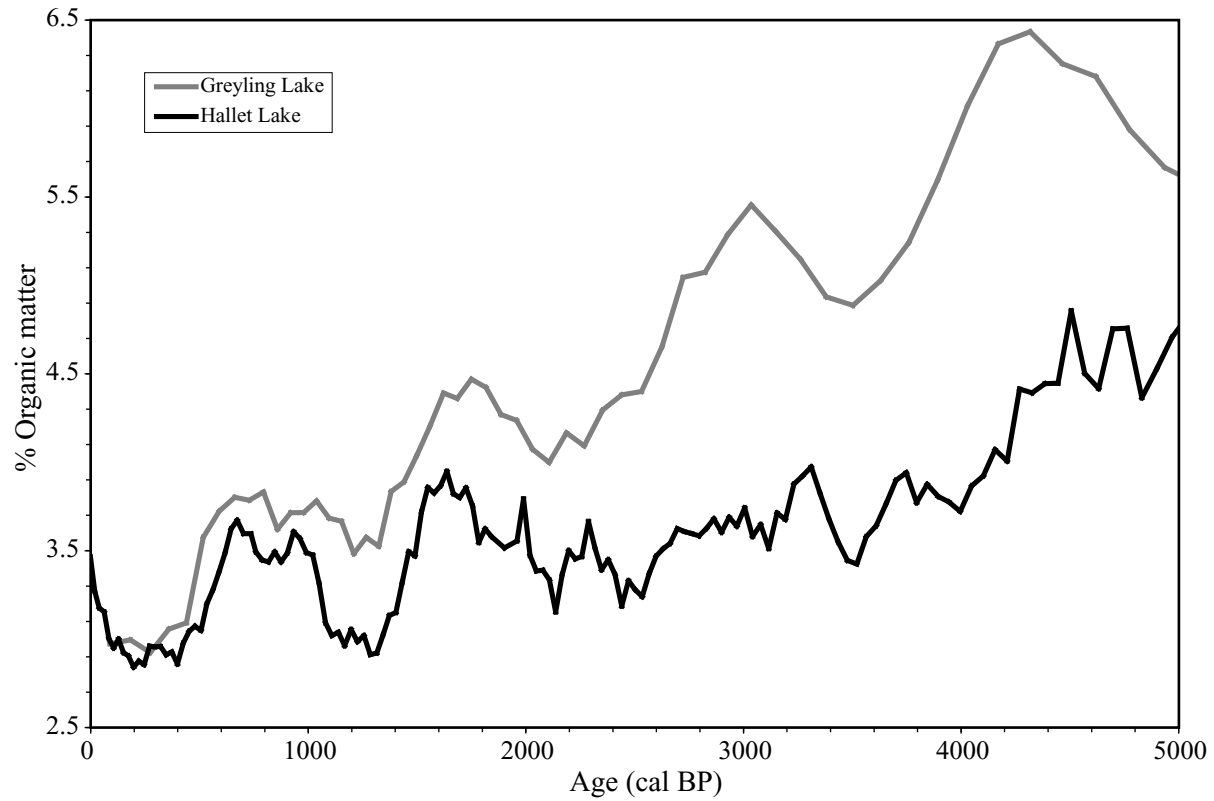


Figure 16. Percent organic matter from cores HT01 (black) and GY05 (grey) over the past 5000 yr. The strong similarities between the two independently dated records from the two lakes (30 km apart) suggest that the sediment sequences respond to regional climate variability over this timescale.

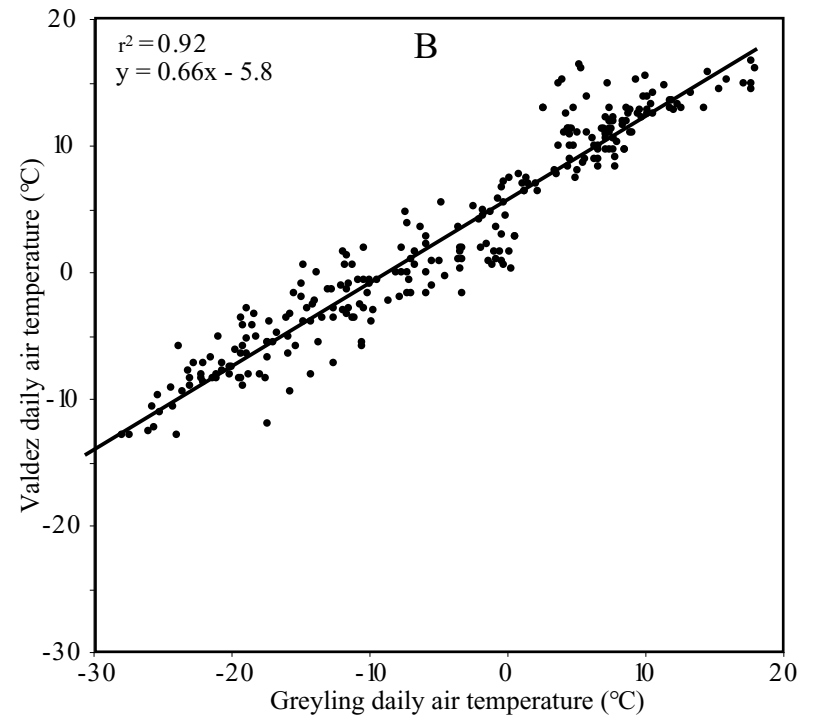
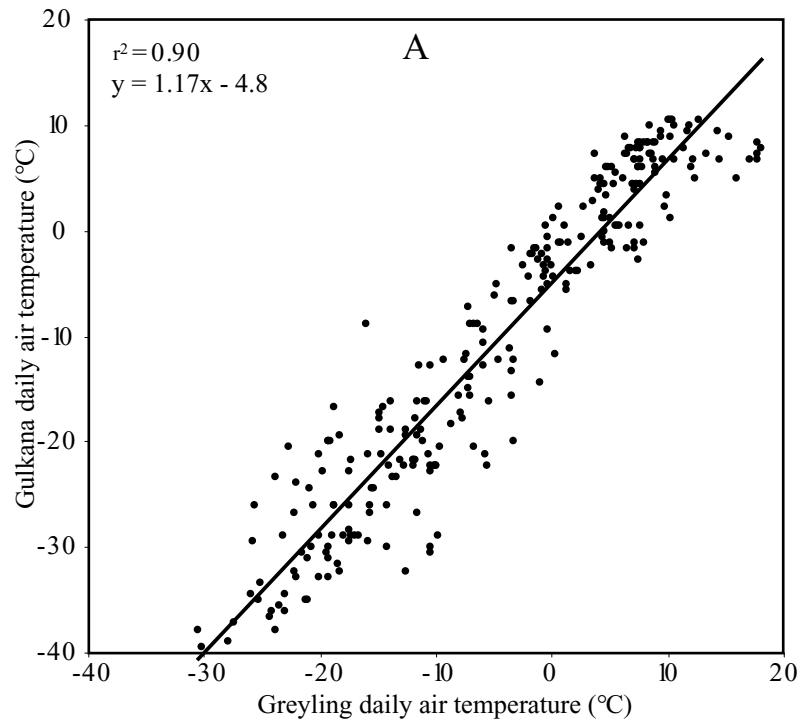


Figure 17. Daily air temperature at Greyling Lake from August 2005 - July 2006, compared against (A) Gulkana and (B) Valdez. Black lines are least-squares linear regressions.

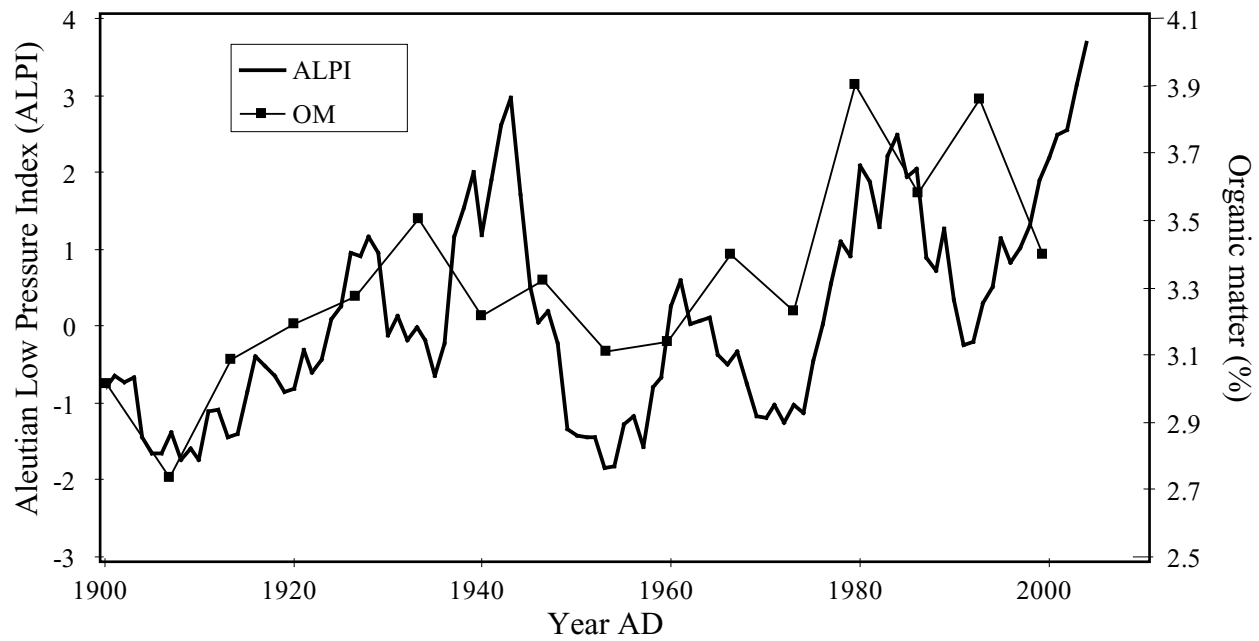


Figure 18. Organic-matter content (OM) in core HT01-B from Hallet Lake over the past 100 yr compared to a 7-year running average of ALPI.

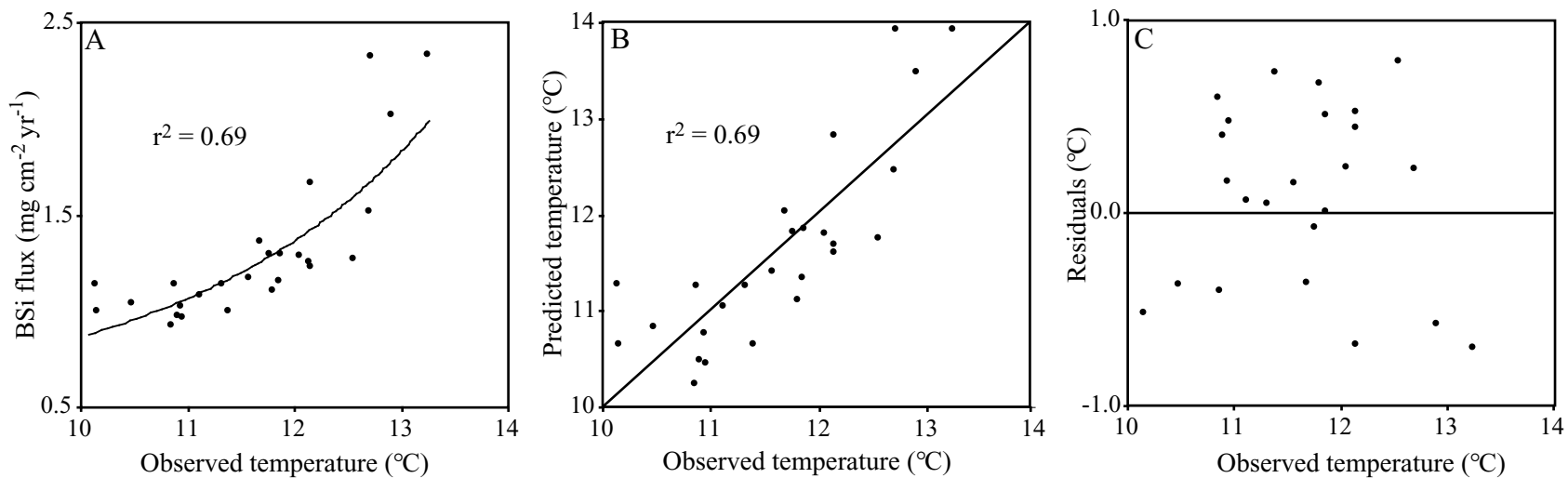


Figure 19. (A) Relation between observed temperature and BSi flux at Hallet Lake; black line shows the least-squares log regression. (B) Relation between observed summer temperature and temperature predicted by the BSi transfer function; black line shows ideal 1:1 relation. (C) Relation between observed summer temperature and residuals (observed - predicted); black line shows ideal residuals (0).

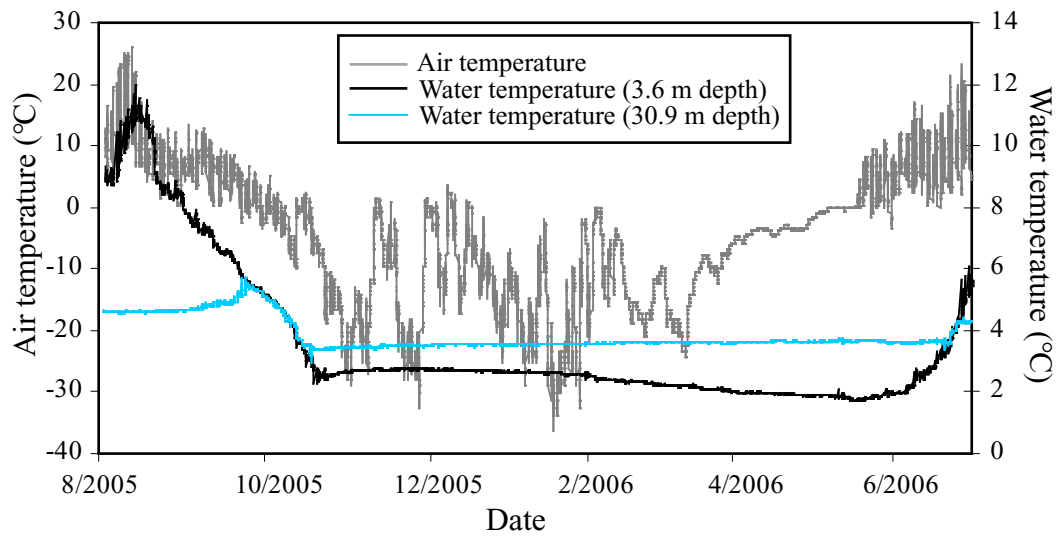


Figure 20. Air temperature and water temperature (at 3.6 and 30.9 m depth) from Greyling Lake from August 2005 to July 2006. Water temperature, during the open-water season, follows major air temperature trends with a 4-day lag.

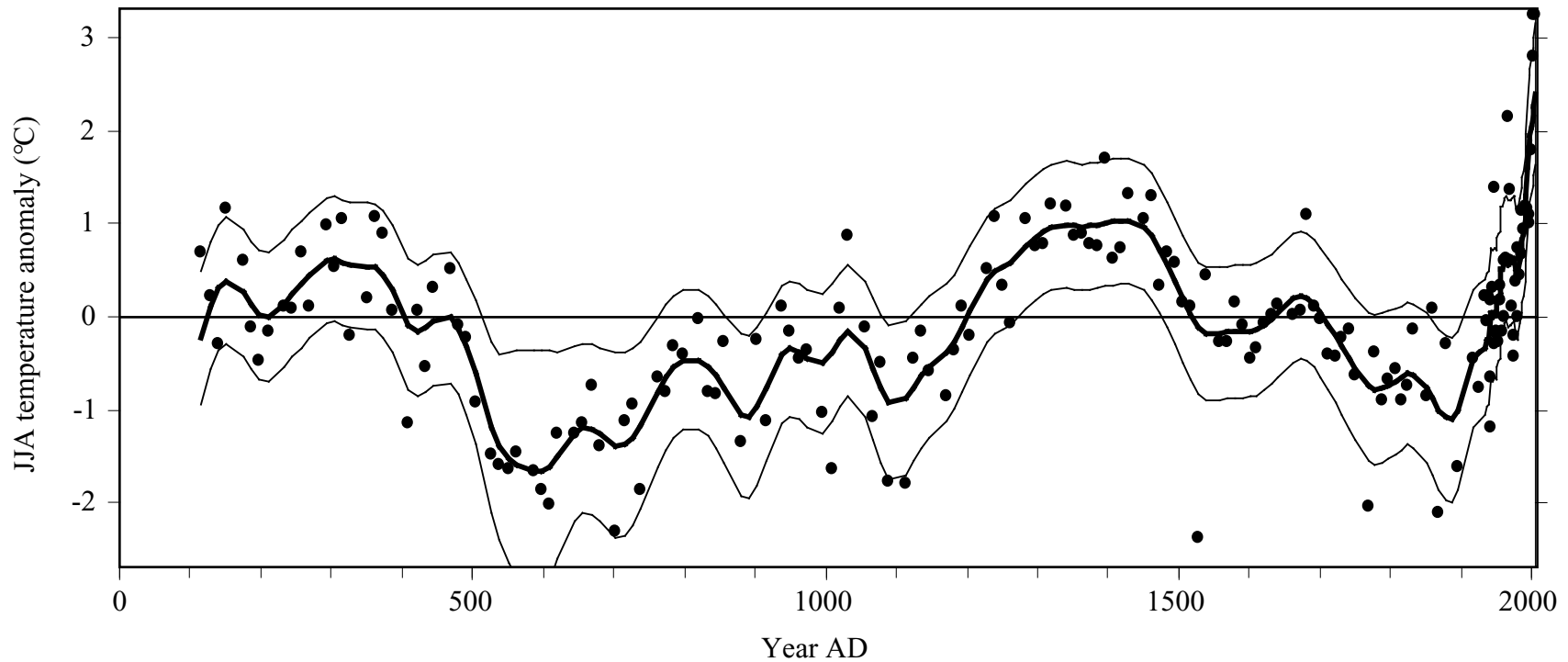


Figure 21. Reconstructed summer temperatures anomalies from the 2 kyr average, inferred from BSi flux from Hallet Lake. Black line indicates the average for the past 2 kyr (10.6 °C). Thick curve is the 50-year Gaussian-weighted low-pass filtered curve. Thin curves are confidence intervals determined as the $RMSEP_{(boot)}$ values calculated for each point in the reconstruction. Data listed in Appendix A-6.

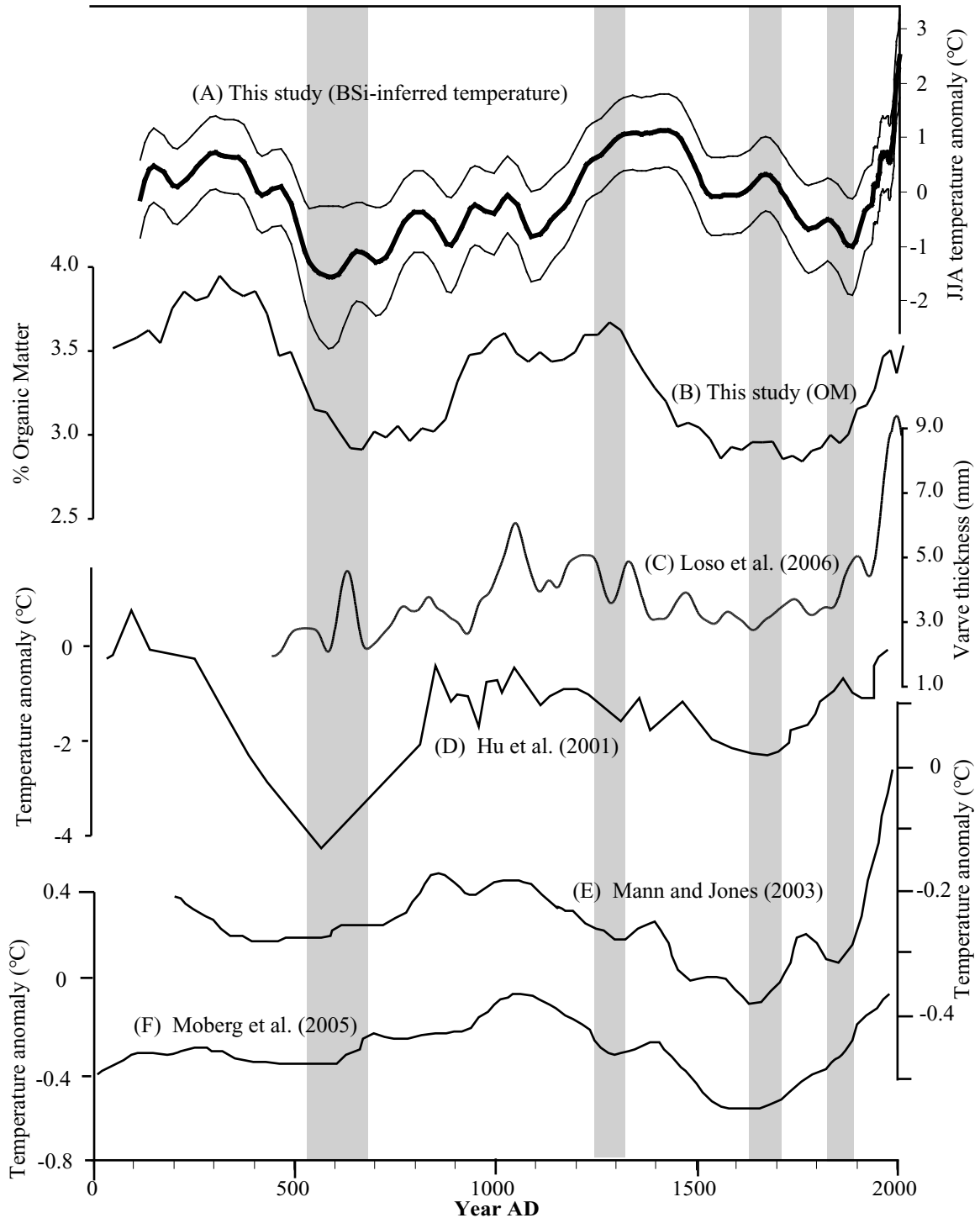


Figure 20. Compilation of climate records from the Northern Hemisphere. (A) BSi-inferred summer temperature anomalies from Hallet Lake (this study). (B) OM from Hallet Lake (this study). (C) Varve thickness from Iceberg Lake, eastern Chugach Range (Loso et al., 2006). (D) Isotope-inferred temperature from Farewell Lake, northwestern Alaska Range. (E) Multi-proxy temperature reconstruction for the Northern Hemisphere (Mann and Jones, 2003). (F) Multi-proxy temperature reconstruction for the Northern Hemisphere (Moberg et al., 2005). Shaded intervals are periods of glacial advance in southern Alaska (Wiles et al., 2007). Study locations shown on figure 1.

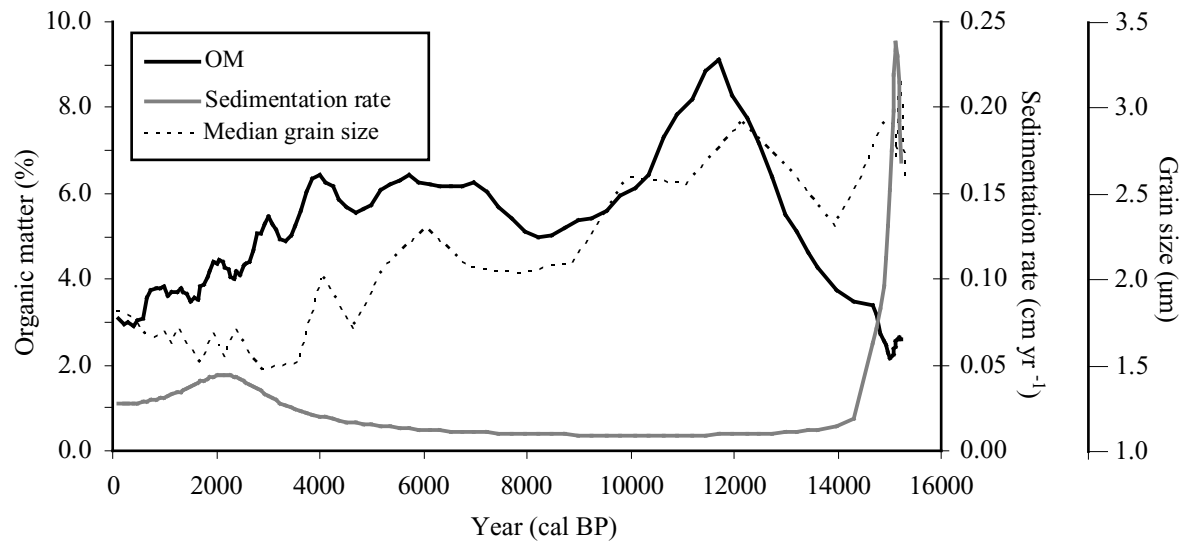


Figure 23. Organic matter (OM), sedimentation rate, and median grain size at Greyling Lake for the past 16 ka.

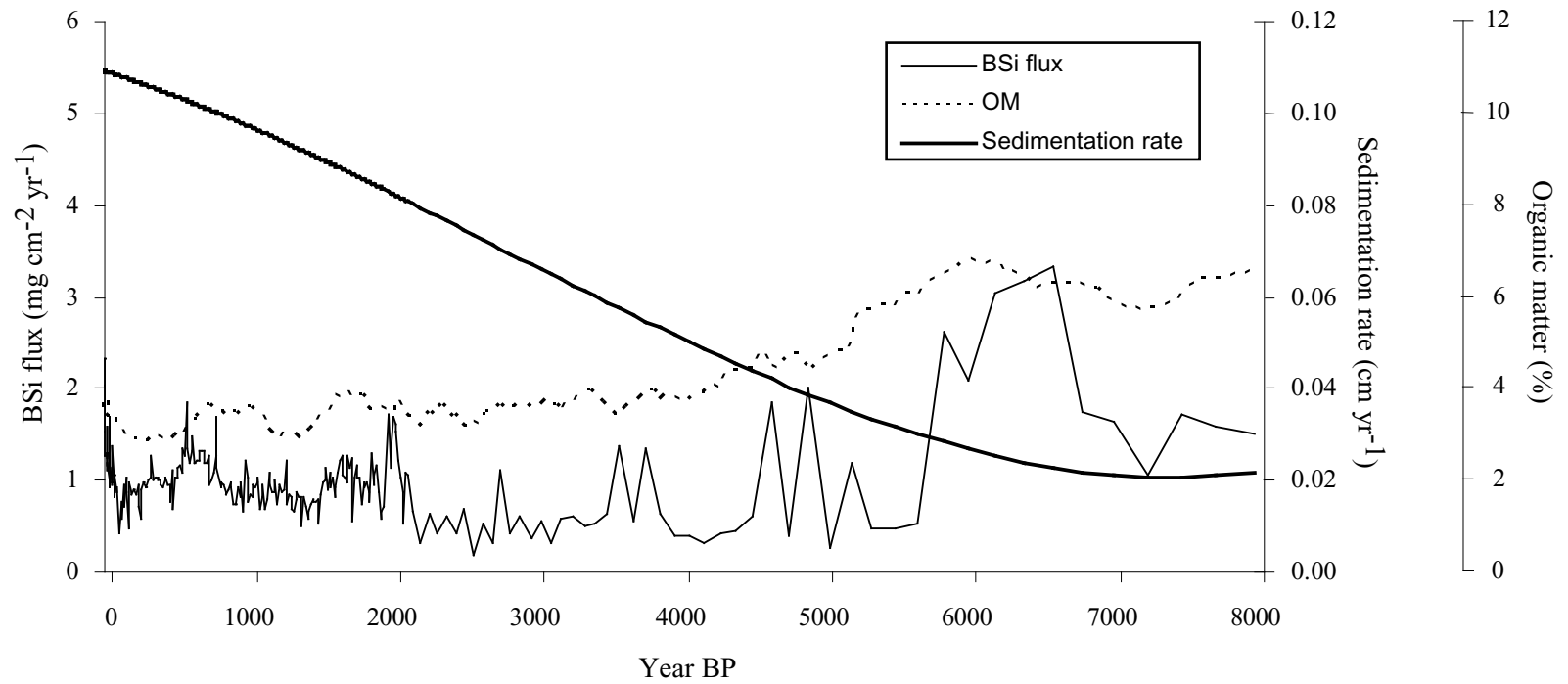


Figure 24. Biogenic silica (BSi), sedimentation rate, and organic matter (OM) from Hallet Lake.

Appendix A-1. Magnetic susceptibility data for core HT01

Depth	0	20	40	60	80	100	120	140	160	180	200	220
0.0		34	33	24	34	21	28	33	21	264	36	35
0.5		33	24	24	31	28	34	38	36	208	37	36
1.0		30	26	25	25	32	28	33	39	25	37	34
1.5		31	30	28	23	29	23	32	26	32	36	30
2.0	22	31	26	29	28	30	32	36	23	25	36	28
2.5	28	21	26	31	29	27	33	39	27	35	37	26
3.0	27	23	21	29	16	28	33	37	26	30	36	26
3.5	30	22	21	33	17	28	32	36	29	25	34	26
4.0	32	19	24	32	13	28	31	29	33	24	32	30
4.5	31	23	25	34	20	26	32	26	34	28	30	31
5.0	29	22	31	29	28	24	23	29	34	29	30	30
5.5	30	21	33	32	28	28	34	32	36	32	31	33
6.0	30	20	32	30	26	23	34	34	36	32	32	35
6.5	31	18	31	29	24	25	31	35	34	31	36	34
7.0	29	21	26	31	21	30	31	37	32	34	33	32
7.5	25	26	23	30	19	30	31	36	33	33	32	36
8.0	22	34	23	29	26	27	30	37	31	28	30	35
8.5	20	32	26	27	32	32	30	35	28	32	28	24
9.0	16	31	28	26	32	28	29	35	30	31	28	17
9.5	13	31	26	25	29	21	30	31	31	27	24	20
10.0	12	31	23	26	25	31	31	30	29	31	27	21
10.5	16	26	31	25	14	37	32	35	32	33	29	19
11.0	27	19	30	26	9	34	35	37	31	31	28	25
11.5	31	22	26	28	14	34	35	50	31	31	26	36
12.0	23	20	28	24	13	35	36	42	31	37	26	34
12.5	33	24	29	23	8	33	33	44	33	38	25	35
13.0	31	31	30	25	6	35	35	33	31	39	25	35
13.5	30	31	31	24	15	32	31	30	26	39	23	36
14.0	31	32	28	24	23	28	31	29	22	41	23	33
14.5	36	33	27	23	27	26	26	27	26	39	21	28
15.0	35	32	28	22	24	25	31	27	33	33	22	16
15.5	37	30	25	28	23	29	34	35	36	30	33	37
16.0	35	16	28	30	22	29	33	32	37	29	35	31
16.5	32	12	30	30	25	28	36	32	39	30	32	30
17.0	33	17	31	30	26	28	37	29	39	34	31	34
17.5	34	19	30	28	29	25	34	22	39	31	31	35
18.0	34	31	28	28	26	28	28	21	32	27	36	34
18.5	34	32	27	25	30	30	24	18	37	26	37	31
19.0	32	34	28	27	28	29	24	20	66	25	34	33
19.5	37	34	25	30	25	29	29	22	203	35	34	35

Appendix A-1. (continued)

Depth	240	260	280	300	320	340	360	380	400	420	440
0.0	34	48	25	37	40	32	10	24	16	7	18
0.5	37	74	27	40	45	36	26	20	26	8	16
1.0	37	40	35	41	32	36	30	13	23	15	21
1.5	35	33	39	40	35	26	26	9	17	22	27
2.0	26	32	39	41	32	27	26	10	14	24	24
2.5	28	31	34	39	30	29	30	10	12	21	30
3.0	26	37	31	37	30	32	19	9	22	18	16
3.5	31	36	32	37	30	33	19	10	23	18	14
4.0	34	35	34	37	31	33	28	12	23	19	11
4.5	25	42	35	33	30	16	29	11	18	23	5
5.0	27	41	38	35	33	9	28	9	15	31	8
5.5	31	39	37	38	32	28	26	14	14	35	13
6.0	26	41	36	37	33	27	17	14	16	34	10
6.5	23	38	34	39	31	25	11	16	16	29	10
7.0	23	38	35	35	31	28	9	14	12	6	7
7.5	23	38	37	39	28	33	9	9	10	3	
8.0	26	37	36	38	29	34	10	10	13	11	
8.5	17	36	35	37	29	42	10	12	11	21	
9.0	15	38	33	36	27	33	7	12	12	27	
9.5	31	40	33	41	24	44	4	12	13	23	
10.0	27	37	33	42	17	34	5	14	21	14	
10.5	34	34	35	40	14	23	14	19	27	21	
11.0	34	38	37	40	29	20	16	12	16	26	
11.5	40	43	36	39	24	25	15	16	9	25	
12.0	40	37	33	42	25	10	17	17	22	23	
12.5	37	34	35	40	30	10	18	25	28	15	
13.0	33	37	37	35	32	18	19	25	20	12	
13.5	30	36	38	36	32	15	21	23	11	25	
14.0	29	28	38	37	33	17	20	23	17	26	
14.5	28	34	40	36	32	17	23	22	20	16	
15.0	25	40	36	35	34	15	25	22	28	8	
15.5	24	41	38	35	33	6	25	23	30	7	
16.0	40	36	39	35	30	8	27	26	20	14	
16.5	42	38	37	33	29	3	27	28	17	19	
17.0	25	33	36	34	31	6	28	25	15	25	
17.5	25	29	35	36	30	13	28	24	15	17	
18.0	25	31	34	36	29	19	29	22	14	19	
18.5	33	33	36	38	28	7	22	14	17	18	
19.0	40	36	36	40	28	7	23	14	4	17	
19.5	33	33	34	41	32	10	23	20	3	26	

Note: The sums of the column and row headings indicate the depth for the magnetic susceptibility readings. Magnetic susceptibility reported in 10^{-6} SI units.

Appendix A-2. Magnetic susceptibility data for core GY05

Depth	0	20	40	60	80	100	120	140	160	180	200	220
0.0		37	37	34	67	20	13	10	-10	6	6	7
0.5		37	40	35	28	27	10	7	-11	8	6	8
1.0	24	34	68	37	25	42	8	6	-10	10	6	8
1.5	26	22	65	28	22	48	8	14	13	9	9	5
2.0	22	24	29	28	22	30	12	15	12	10	10	7
2.5	25	26	29	24	17	15	13	15	12	10	7	6
3.0	26	30	29	22	13	13	11	16	13	9	6	6
3.5	30	33	30	19	14	15	12	17	30	8	5	5
4.0	29	43	29	20	15	23	13	16	45	8	5	6
4.5	31	60	30	21	28	14	14	16	12	9	6	6
5.0	31	59	30	22	20	15	17	16	11	8	4	7
5.5	32	49	31	32	15	13	18	17	12	10	5	5
6.0	34	36	30	46	24	13	9	15	11	9	5	5
6.5	34	32	32	86	83	17	7	16	15	10	4	5
7.0	34	30	32	210	27	11	9	16	10	10	5	5
7.5	33	29	33	222	23	11	11	15	14	16	4	5
8.0	33	31	33	43	15	14	13	9	10	13	4	6
8.5	36	31	31	26	15	26	17	9	10	11	4	6
9.0	30	30	34	20	15	35	18	15	7	10	5	6
9.5	36	35	34	21	15	16	20	15	14	14	4	6
10.0	37	37	36	20	11	17	25	15	10	14	5	8
10.5	36	34	39	22	9	13	42	15	10	13	5	7
11.0	39	34	36	27	13	11	53	15	10	12	4	8
11.5	25	25	25	20	20	16	23	9	14	10	6	12
12.0	27	27	24	21	16	18	14	7	19	10	5	19
12.5	26	28	22	20	27	17	11	3	20	11	5	29
13.0	23	25	26	21	16	17	10	2	12	12	5	37
13.5	26	26	29	21	19	22	9	2	10	13	5	34
14.0	27	27	30	26	18	17	10	3	11	12	6	27
14.5	28	26	29	27	19	15	10	6	10	11	7	22
15.0	29	32	27	22	31	17	10	8	10	10	6	17
15.5	33	35	24	23	21	18	11	1	11	10	6	16
16.0	34	33	24	23	18	19	12	-2	12	8	6	15
16.5	26	34	24	20	20	18	14	-4	13	8	5	15
17.0	38	41	24	21	16	60	13	-7	16	8	5	17
17.5	53	39	24	24	14	29	14	-7	18	10	5	17
18.0	49	44	27	22	13	15	19	-6	19	9	6	15
18.5	67	47	30	0	13	11	28	-8	18	9	5	16
19.0	44	39	32	22	13	14	22	-10	16	7	5	16
19.5	38	39	33	28	13	15	15	-11	13	6	7	15

Appendix A-2. (continued)

Depth	240	260	280	300	320	340
0.0	15	16	17	9	2	25
0.5	16	14	16	9	1	26
1.0	14	15	16	8	-2	25
1.5	11	19	17	25	3	25
2.0	12	27	15	25	5	27
2.5	14	19	15	25	29	28
3.0	20	16	14	26	26	33
3.5	25	15	14	26	15	52
4.0	22	18	14	24	8	47
4.5	25	18	13	20	10	29
5.0	32	18	13	23	9	25
5.5	30	20	14	24	10	24
6.0	25	17	13	24	25	22
6.5	21	22	12	24	24	11
7.0	18	23	12	23	12	10
7.5	18	24	13	22	16	14
8.0	16	24	12	21	28	24
8.5	16	27	11	20	33	24
9.0	16	28	12	23	26	
9.5	16	27	10	24	19	
10.0	17	27	11	17	8	
10.5	16	28	10	23	13	
11.0	17	28	10	23	26	
11.5	18	27	11	24	22	
12.0	17	26	10	23	21	
12.5	18	25	9	23	24	
13.0	18	22	10	21	26	
13.5	19	22	10	22	27	
14.0	18	22	10	21	27	
14.5	17	21	9	21	28	
15.0	16	23	9	22	27	
15.5	20	20	10	21	28	
16.0	18	20	9	21	30	
16.5	18	19	9	22	28	
17.0	19	16	8	20	29	
17.5	13	19	-1	22	27	
18.0	24	18	4	22	26	
18.5	33	19	5	23	26	
19.0	24	18	7	21	25	
19.5	22	18	9	12	24	

Note: The sums of the column and row headings indicate the depth for the magnetic susceptibility readings. Magnetic susceptibility reported in 10^{-6} SI units.

Appendix A-3. Percent organic-matter for cores HT01 and GY05

Depth	Core HT01					Core GY05			
	0	100	200	300	400	1	101	201	301
0.0	3.4	3.4	3.4	3.5	7.3	3.3	5.5	6.4	2.3
2.5	3.8	4.0	3.5	3.4	6.5	2.7	5.3	7.1	
5.0	3.4	3.4	3.1	3.6	6.4	3.2	5.2	6.1	2.3
7.5	2.9	3.2	3.6	4.5	6.0	2.6	5.3	7.2	
10.0	3.9	3.3	3.9	3.3	6.5	3.1	5.2	9.7	2.4
12.5	3.3	2.6	3.2	4.1	5.5	3.0	4.7	9.2	
15.0	2.9	2.9	3.5	4.0	7.1	3.4	4.2	8.7	2.7
17.5	2.9	3.1	4.1	3.8	6.2	3.4	5.0	9.5	
20.0	2.8	3.3	2.8	3.6	6.0	5.0	6.0	8.4	2.6
22.5	3.2	3.0	3.3	3.8	5.9	3.8	6.3	5.6	
25.0	3.0	3.1	3.5	3.8	4.3	3.4	6.5	6.5	2.9
27.5	3.1	2.6	3.1	3.9	6.3	3.3	6.3	5.8	
30.0	2.5	3.2	3.2	3.5	6.1	3.6	6.7	5.7	2.4
32.5	2.7	2.7	3.6	4.4	6.5	4.0	6.3	4.1	
35.0	2.9	3.0	3.0	4.1	6.8	4.3	5.4	3.5	2.6
37.5	3.2	3.6	3.3	4.5		3.4	6.1		
40.0	3.0	3.1	3.8	3.5	6.3	3.6	4.8	4.0	
42.5	3.0	3.3	3.7	5.6		3.1	5.6		
45.0	2.7	3.6	3.8	4.2		3.9	5.8	4.2	
47.5	2.9	3.9	3.2	4.4		3.4	5.9		
50.0	3.0	3.5	3.7	4.5		3.8	6.6		
52.5	3.1	4.4	3.7	5.6		3.4	6.6		
55.0	2.7	4.0	3.7	3.8		4.7	6.3		
57.5	3.3	3.4	3.7	3.8		4.2	6.2		
60.0	3.2	4.1	3.4	6.1		4.1	6.6	2.9	
62.5	3.1	3.9	4.0	4.5		4.7	5.7		
65.0	3.0	3.7	3.3	3.6		4.3	6.3	2.8	
67.5	3.4	3.9	4.1	4.6		4.5	6.2		
70.0	3.7	3.7	3.4	10.8		4.7	6.0	3.0	
72.5	3.7	3.6	3.9	6.5		3.9	6.6		
75.0	3.7	2.8	3.1	4.7		3.9	6.2	2.9	
77.5	3.7		3.6	7.0		4.2	5.1		
80.0	3.7	4.1	3.4	4.6		3.7	4.3	2.1	
82.5	3.3	3.7	4.5	6.3		4.4	4.7		
85.0	3.7		3.7	6.2		4.7	5.2	2.1	
87.5	3.2	3.4	4.1	6.3		3.5	5.6		
90.0	3.4	3.8	3.9	6.9		5.2	5.4	2.2	
92.5	3.6	4.0	3.7	6.1		4.1	5.1		
95.0	3.6	2.5	3.7	7.1		4.5	5.6	2.2	
97.5	3.4	3.2	3.0	6.7		6.0	5.4		

Note: The sums of the column and row headings indicate the depth for the organic-matter measurements. Organic-matter reported in percent.

Appendix A-4. Grain size data for core HT01.

Depth (cm)	Median grain size (μm)	Grain size distribution (%)					
		Fine clay	Clay	Fine silt	Medium silt	Coarse silt	Very fine sand
2.5	3.2	0.6	36.5	19.3	35.2	7.5	0.8
20	3.3	1.9	33.1	21.6	37.3	5.6	0.6
25	2.9	1.0	37.1	21.4	32.1	6.3	2.2
30	3.0	1.1	36.0	22.3	36.0	4.1	0.5
35	3.3	1.3	33.4	21.5	35.5	7.5	0.8
40	3.8	1.7	30.7	18.8	34.8	10.6	3.3
45	3.2	1.6	33.7	21.4	36.4	5.4	1.4
50	3.3	1.2	33.3	22.3	37.5	4.1	1.5
55	3.9	0.9	35.9	13.9	35.8	9.5	4.0
60	2.9	1.0	36.9	23.3	34.2	4.5	0.2
65	2.9	1.3	36.3	23.0	35.0	4.5	0.0
70	3.5	0.5	34.2	18.7	37.6	7.8	1.2
75	3.4	0.5	35.9	17.6	36.1	8.7	1.2
80	2.4	0.3	44.3	19.7	33.6	2.1	0.0
85	2.9	0.6	38.1	20.6	34.4	6.0	0.3
90	3.3	0.6	34.9	20.1	35.8	7.5	1.1
95	5.0	0.8	30.5	14.5	33.4	18.8	2.1
125	3.0	1.0	36.4	21.6	36.3	4.3	0.4
130	3.2	1.8	34.1	21.4	38.1	4.2	0.3
135	3.4	0.6	34.0	20.6	36.9	7.2	0.7
155	3.1	0.3	37.6	19.8	35.7	6.0	0.5
160	3.1	0.3	36.9	19.8	35.9	6.8	0.3
165	2.9	0.3	38.6	19.8	34.7	6.5	0.2
190	4.9	0.5	29.1	15.6	36.3	14.0	4.4
195	3.6	1.1	32.3	19.4	36.9	8.4	1.9
210	3.2	1.0	34.5	22.1	38.3	4.1	0.0
215	3.6	0.6	33.6	18.8	34.9	9.4	2.7
220	3.6	1.3	31.5	20.7	40.8	4.5	1.2
225	3.7	0.5	32.2	19.3	36.8	9.6	1.7
230	6.3	0.5	26.9	13.8	33.2	18.0	6.0
265	4.2	0.6	30.5	17.4	37.0	11.3	3.2
270	5.4	0.4	28.4	14.8	32.6	15.6	5.8
275	3.5	0.5	34.3	18.5	36.5	8.7	1.5
285	3.7	0.5	33.2	18.7	38.1	8.2	1.3
290	3.7	0.3	33.6	18.1	38.7	7.8	1.5
295	8.7	0.7	22.3	12.6	31.7	19.4	11.2
300	3.6	0.4	34.2	18.6	36.8	8.2	1.8
305	6.5	0.4	26.0	13.8	34.4	15.2	5.4
309	2.9	0.3	38.1	21.2	36.4	3.6	0.4
370	3.6	0.2	35.3	17.1	33.7	10.7	3.0
390	2.9	0.1	40.0	17.4	30.1	10.1	2.2
395	3.8	0.1	34.0	16.8	31.9	12.3	4.9
400	4.1	0.2	31.6	17.7	35.5	10.9	4.0

Note: Fine clay = 0.002-0.2 μm ; Clay = 0.2-2 μm ; Fine silt = 2-4 μm ; Medium silt = 4-20 μm ;
Coarse silt = 20-50 μm ; Very fine sand = 50-100 μm .

Appendix A-5. Grain size data for core GY05.

Depth (cm)	Median grain size (μm)	Grain size distribution (%)			
		Clay	Fine silt	Medium silt	Coarse silt
1	1.9	52.7	30.1	16.8	0.4
6	1.9	52.7	29.9	16.6	0.8
11	1.9	52.9	30.6	16.4	0.1
16	1.8	54.5	29.3	16.1	0.0
21	1.6	58.1	26.9	14.2	0.7
26	1.7	55.8	28.5	15.7	0.0
31	1.7	57.4	28.7	14.0	0.0
36	1.7	56.5	26.7	15.6	1.3
41	1.6	59.0	26.9	14.1	0.1
46	1.6	60.2	27.5	12.3	0.0
51	1.5	60.8	27.1	12.0	0.0
56	1.6	59.6	27.4	13.0	0.0
61	1.7	57.3	26.8	15.3	0.5
71	1.5	61.3	24.8	13.4	0.5
81	1.7	57.3	27.1	15.4	0.2
91	1.5	60.9	24.3	14.6	0.1
101	1.5	62.7	25.0	12.3	0.0
111	1.5	62.6	24.5	12.8	0.0
121	1.5	60.8	26.0	13.0	0.0
131	2.0	49.8	26.5	23.6	0.0
141	1.6	58.0	24.0	17.5	0.4
151	1.9	52.1	23.7	19.0	5.2
161	2.1	47.3	24.3	23.5	4.8
171	1.9	51.1	23.8	21.9	3.2
181	2.0	50.8	25.0	22.0	2.0
191	2.0	50.0	26.0	20.2	3.8
201	2.5	42.0	24.8	28.9	4.3
211	2.5	41.8	24.9	29.4	3.8
221	2.9	36.1	26.0	33.7	4.2
231	2.7	39.2	27.0	30.7	3.1
241	2.3	44.0	27.5	27.4	1.1
251	2.7	39.3	26.7	31.4	2.6
261	2.9	34.8	28.2	35.8	1.2
271	3.0	34.0	26.9	36.8	2.2
281	3.1	33.5	27.6	36.3	2.4
291	3.1	33.5	27.1	36.5	2.3
301	3.0	33.8	27.2	36.7	2.2
311	2.9	35.4	28.4	34.9	1.2
331	3.3	31.0	25.9	39.2	3.7
341	2.6	38.7	28.5	31.0	1.7

Note: Fine clay = Clay = 0.2-2 μm ; Fine silt = 2-4 μm ;
Medium silt = 4-20 μm ; Coarse silt = 20-50 μm .

Appendix A-6. Biogenic silica data for core HT01

Depth	BSi	BSi flux	BSi-inferred	Depth	BSi	BSi flux	BSi-inferred
(cm)	(%)	(mg cm⁻² yr⁻¹)	(°C)	(cm)	(%)	(mg cm⁻² yr⁻¹)	(°C)
0.13	1.56	2.33	13.9	21.25	0.66	0.99	10.6
0.38	1.55	2.33	13.9	22.25	0.59	0.88	10.0
0.63	1.35	2.03	13.5	23.25	0.58	0.86	9.8
0.88	1.01	1.52	12.5	24.25	0.61	0.91	10.1
1.13	0.85	1.28	11.8	25.25	0.60	0.89	10.0
1.38	0.84	1.26	11.7	26.25	0.58	0.86	9.8
1.63	0.87	1.30	11.8	27.25	0.63	0.94	10.3
1.88	0.87	1.31	11.9	28.25	0.49	0.72	8.6
2.13	0.86	1.29	11.8	30.25	0.61	0.90	10.1
2.38	0.82	1.24	11.6	31.25	0.66	0.98	10.6
2.63	0.86	1.30	11.8	32.25	0.65	0.97	10.5
2.88	0.78	1.16	11.4	33.25	0.63	0.93	10.3
3.13	0.74	1.11	11.1	34.25	0.63	0.94	10.3
3.38	0.79	1.18	11.4	35.25	0.68	1.01	10.7
3.63	0.67	1.01	10.7	36.25	0.70	1.03	10.8
3.88	0.73	1.09	11.1	37.25	0.87	1.28	11.8
4.13	0.62	0.93	10.3	38.25	0.69	1.02	10.7
4.38	0.65	0.97	10.5	39.25	0.69	1.02	10.7
4.63	0.69	1.03	10.8	41.25	0.70	1.04	10.8
4.88	0.76	1.14	11.3	42.25	0.69	1.02	10.7
5.13	0.91	1.37	12.1	43.25	0.68	1.00	10.6
5.38	1.12	1.68	12.8	44.25	0.64	0.95	10.3
5.63	0.77	1.15	11.3	45.25	0.63	0.93	10.2
5.88	0.67	1.01	10.7	46.25	0.68	0.99	10.6
6.13	0.76	1.15	11.3	47.25	0.71	1.04	10.8
6.38	0.65	0.98	10.5	48.25	0.65	0.96	10.4
6.63	0.70	1.05	10.9	49.25	0.66	0.96	10.4
6.88	0.72	1.08	11.0	51.25	0.76	1.11	11.1
7.13	0.64	0.96	10.4	52.25	0.47	0.69	8.3
7.38	0.65	0.97	10.5	53.25	0.71	1.03	10.8
7.50	0.65	0.98	10.5	54.25	0.72	1.04	10.9
7.63	0.92	1.37	12.1	55.25	0.78	1.14	11.3
7.88	0.64	0.96	10.4	56.25	0.80	1.17	11.4
8.13	0.72	1.08	11.0	57.25	0.75	1.08	11.0
8.38	0.60	0.89	10.0	58.25	0.93	1.35	12.0
8.50	0.55	0.82	9.5	59.25	0.87	1.27	11.7
8.63	0.70	1.05	10.9	61.25	0.93	1.35	12.0
8.88	0.70	1.06	10.9	62.25	0.82	1.18	11.4
9.13	0.67	1.00	10.6	63.25	0.80	1.15	11.3
9.50	0.71	1.06	10.9	64.25	1.03	1.48	12.4
10.50	0.59	0.88	9.9	65.25	0.82	1.18	11.4
11.50	0.62	0.93	10.2	66.25	0.83	1.19	11.5
14.25	0.51	0.77	9.1	67.25	0.85	1.22	11.6
15.25	0.40	0.59	6.9	68.25	0.85	1.22	11.6
16.25	0.64	0.96	10.4	69.25	0.91	1.31	11.9
17.25	0.48	0.71	8.6	71.25	0.92	1.32	11.9
18.25	0.69	1.03	10.8	72.25	0.83	1.19	11.5
19.25	0.58	0.86	9.8	73.25	0.83	1.19	11.4

Appendix A-6. (continued)

Depth	BSi	BSi flux	BSi-inferred temperature	Depth	BSi	BSi flux	BSi-inferred temperature
(cm)	(%)	(mg cm ⁻² yr ⁻¹)	(°C)	(cm)	(%)	(mg cm ⁻² yr ⁻¹)	(°C)
74.25	0.89	1.27	11.7	134.25	1.85	2.43	14.1
76.25	0.70	1.00	10.6	136.25	0.60	0.78	9.2
77.25	0.76	1.08	11.0	137.25	0.58	0.76	9.1
78.25	0.90	1.28	11.8	138.25	0.59	0.77	9.1
79.25	0.79	1.12	11.2	139.25	0.60	0.78	9.2
81.25	0.69	0.97	10.5	141.25	0.66	0.85	9.8
82.25	0.73	1.03	10.8	142.25	0.75	0.97	10.5
83.25	0.67	0.94	10.3	143.25	0.77	0.99	10.6
84.25	0.61	0.86	9.8	144.25	0.87	1.12	11.2
86.25	0.64	0.90	10.1	146.25	0.83	1.08	11.0
87.25	0.70	0.98	10.5	147.25	0.71	0.91	10.2
88.25	0.66	0.93	10.2	148.25	0.80	1.02	10.7
89.25	0.53	0.75	8.9	149.25	0.64	0.82	9.5
91.25	0.53	0.75	8.9	151.25	1.63	2.09	13.6
92.25	0.66	0.92	10.2	152.25	0.96	1.22	11.6
93.25	0.60	0.83	9.6	153.25	1.00	1.28	11.8
94.25	0.71	0.99	10.6	154.25	0.83	1.05	10.9
96.25	0.87	1.22	11.6	156.25	0.76	0.97	10.5
97.25	0.74	1.03	10.8	157.25	1.00	1.26	11.7
98.25	0.55	0.76	9.1	158.25	0.90	1.13	11.2
99.25	0.61	0.84	9.7	159.25	0.99	1.25	11.7
101.25	0.68	0.94	10.3	161.25	0.82	1.03	10.8
102.25	0.67	0.93	10.2	162.25	0.93	1.17	11.4
103.25	0.71	0.98	10.5	163.25	0.82	1.03	10.8
104.25	0.75	1.03	10.8	164.25	0.83	1.03	10.8
106.25	0.60	0.83	9.6	166.25	0.79	0.98	10.5
107.25	0.70	0.96	10.4	167.25	0.74	0.92	10.2
108.25	0.47	0.65	7.8	168.25	0.80	0.99	10.6
109.25	0.58	0.80	9.4	169.25	3.00	3.71	15.3
111.25	0.70	0.96	10.4	171.25	1.05	1.30	11.8
112.25	0.64	0.87	9.9	172.25	0.78	0.95	10.4
113.25	0.64	0.87	9.9	173.25	0.86	1.06	10.9
114.25	0.74	1.00	10.7	174.25	0.95	1.17	11.4
116.25	0.69	0.94	10.3	176.25	0.47	0.57	6.5
117.25	0.70	0.95	10.4	177.25	0.55	0.67	8.1
118.25	0.65	0.87	9.9	178.25	0.59	0.72	8.6
119.25	0.67	0.90	10.0	182.25	0.94	1.14	11.3
121.25	0.55	0.74	8.8	183.25	1.11	1.34	12.0
122.25	0.64	0.85	9.8	184.25	1.41	1.70	12.9
123.25	0.62	0.83	9.6	186.25	1.29	1.54	12.5
124.25	0.52	0.70	8.4	187.25	1.01	1.20	11.5
126.25	0.60	0.79	9.3	188.25	0.86	1.03	10.8
127.25	0.66	0.88	9.9	189.25	0.72	0.86	9.8
128.25	0.62	0.82	9.5	191.25	0.91	1.08	11.0
129.25	0.61	0.81	9.4	192.25	0.88	1.05	10.9
131.25	0.61	0.81	9.4	195.25	0.56	0.66	*
132.25	0.55	0.72	8.7	200.25	0.27	0.31	*
133.25	0.45	0.59	6.8	205.25	0.56	0.65	*

Appendix A-6. (continued)

Depth	BSi	BSi flux	BSi-inferred temperature	Depth	BSi	BSi flux	BSi-inferred temperature
(cm)	(%)	(mg cm ⁻² yr ⁻¹)	(°C)	(cm)	(%)	(mg cm ⁻² yr ⁻¹)	(°C)
210.25	0.38	0.43	*	330.25	0.43	0.31	*
215.25	0.53	0.60	*	335.25	0.59	0.42	*
220.25	0.37	0.41	*	340.25	0.68	0.46	*
225.25	0.62	0.68	*	345.25	0.94	0.62	*
230.25	0.18	0.19	*	350.25	2.94	1.86	*
235.25	0.50	0.53	*	355.25	0.66	0.40	*
240.25	0.30	0.32	*	360.25	3.43	2.00	*
245.25	1.05	1.10	*	365.25	0.47	0.26	*
250.25	0.40	0.41	*	370.75	2.27	1.20	*
255.25	0.60	0.61	*	375.25	0.96	0.48	*
260.25	0.36	0.36	*	380.25	0.99	0.47	*
265.25	0.56	0.55	*	385.25	1.16	0.52	*
270.25	0.34	0.33	*	390.25	6.13	2.63	*
275.25	0.60	0.57	*	395.25	5.17	2.09	*
280.25	0.64	0.60	*	400.25	7.94	3.05	*
285.25	0.55	0.51	*	405.25	8.70	3.16	*
290.25	0.60	0.54	*	410.25	9.59	3.32	*
295.25	0.72	0.63	*	415.25	5.25	1.74	*
300.25	1.61	1.38	*	420.25	5.09	1.63	*
305.25	0.66	0.55	*	425.25	3.40	1.07	*
310.25	1.64	1.34	*	430.25	5.52	1.72	*
315.25	0.79	0.63	*	435.25	5.03	1.59	*
320.25	0.50	0.39	*	440.25	4.61	1.52	*
325.25	0.53	0.40	*	445.25	14.06	4.91	*

*BSi-inferred temperatures were only determined for the past 2 kyr